Anatomy of the Indian Summer Monsoon and ENSO relationship in a state-of-the-art CGCM: Role of the tropical Atlantic Ocean

Pascal Terray[1], Ligin Joseph[2], KP Sooraj[3]

[1] LOCEAN/IPSL, Sorbonne Universités (UPMC, Univ Paris 06)-CNRS-IRD-MNHN, Paris, France
[2]Institut Universitaire Européen de la Mer, Université de Bretagne Occidentale, Brest, France
[3]CCCR, Indian Institute of Tropical Meteorology, Ministry of Earth Sciences, Pune, India

Revised for **Climate Dynamics**

15 June 2022

1

Corresponding author address: Pascal Terray, LOCEAN-IPSL, Sorbonne Universités (Campus Université Pierre et Marie Curie), BP100 – 4 Place Jussieu, 75252 Paris cedex 05, France. Tel : +33 1 44 27 70 72. E-mail : pascal.terray@locean.ipsl.fr

Abstract

The main paradigm for prediction of Indian Summer Monsoon Rainfall (ISMR) is its inverse relation with El Niño-Southern Oscillation (ENSO). In this study, we focus on the role of the Atlantic Ocean (AO) Sea Surface Temperature (SST) variability on the ISMR. There are basically two ways by which AO SSTs can impact the ISMR: a “direct pathway” in which the AO may directly force the ISMR in the absence of interactions with other dominant forcings like ENSO, and an “indirect pathway” in which AO forces ENSO and modulates the ENSO teleconnection to ISMR. These two pathways are studied with the help of sensitivity experiments performed with a Coupled General Circulation Model (CGCM). Two pairs of decoupling experiments have been done. In the first, the SST variability in the tropical AO or Pacific Ocean (PO) is removed by nudging the SST in these regions from a control run's SST climatology. In the second set, the SST nudging is performed from the observed SST climatology, which allows us to assess the robustness of the results and the specific role of the model’s SST mean-state biases.

The direct pathway linking tropical AO SST variability onto ISMR is insignificant in the PO decoupled experiments or in recent observations. Furthermore, these experiments suggest on the contrary that many AO SST anomalous patterns could be forced by ISMR. On the other hand, for the indirect pathway, the AO decoupled experiments demonstrate that AO SST variability modulates the onset and decaying phases of ENSO events. Despite ENSO is as strong and persists longer than in the control simulation, the AO SST nudging resulted in a significant weakening of the inverse relationship between ENSO and ISMR. The ENSO-monsoon relationship is mainly modulated during the ENSO decaying phase. The upper-level divergent wind flows mainly from the Pacific to the AO resulting in rainfall suppression in the AO, but only in a weak forcing on ISMR during boreal summer of the ENSO decaying year in the AO decoupled experiments. Thus, the AO rainfall variability in these experiments is decoupled from the surface and mainly modulated by the upper-level convergence or divergence induced by the remote ENSO forcing.

Finally, the rectification of the AO SST mean-state biases in the CGCM also induces an El Niño-like mean pattern over the tropical Pacific during boreal spring and promotes a stronger ENSO during its peak phase. This demonstrates that the prominent AO SST mean-state biases in current CGCMs further complicate the dynamical prediction and simulation of ISMR and ENSO.

Keywords: Indian Summer Monsoon; El Niño-Southern Oscillation; tropical Atlantic Ocean; ocean-atmosphere interactions; Walker circulation, coupled climate model.

1. Introduction

In India, the rainy season is from June to September (JJAS) and Indian Summer Monsoon Rainfall (ISMR) provides 80% of India's total annual precipitation. Despite the standard deviation of ISMR is only about 10% of its mean, ISMR variability has a tremendous impact on water resource management, agricultural yield and India's gross domestic product (Gadgil and Gadgil 2006). However, forecasting ISMR variability is still a scientific challenge (Rao et al. 2019) and an active research area as it involves many factors and their complex interactions (see Chowdary et al. 2021 for recent review).

Numerous studies have examined climatic controls on ISMR interannual variability and most of them showed the role played by tropical Pacific, Indian and Atlantic oceans Sea Surface Temperature (SST) anomalies (Chowdary et al. 2021). El Niño-Southern Oscillation (ENSO) is the primary forcing of year-to-year ISMR variability (Webster et al. 1998). However, since ENSO can only explain about 35% the interannual variance of ISMR and the ISM-ENSO relationship has weakened during the latter part of the 20th century, partly in response to coherent multi-decadal variability of the climate system (Kumar et al. 1999; Kucharski et al. 2007; Srivastava et al. 2019; Yang and Huang 2021), it is important to look for other sources of ISMR predictability.

First, many studies have suggested a connection between ISM and Indian Ocean (IO) SSTs, especially the Indian Ocean Dipole (IOD; see reviews in Cherchi et al. 2021). The IOD is an irregular interannual SST oscillation in which the eastern equatorial IO gets alternately colder and then warmer than the western part during boreal fall. Positive IOD events (e.g., warm in the western IO) may enhance ISMR through moisture transport over the western IO or modification of the local Hadley cell with increased ascendance over the Indian region (Cherchi et al. 2021). However, the influence of IOD on both ISMR and ENSO remains a controversial topic (Meehl et al. 2003; Fischer et al. 2005; Izumo et al. 2010; Cretat et al. 2017, 2018; Stuecker et al. 2017; Terray et al. 2021; Cherchi et al. 2021; Zhang et al. 2021a).

The Atlantic Ocean (AO) can also add its impact on ISMR (Kucharski et al. 2007, 2009; Pottapinjara et al. 2014, 2016; Sabeerali et al. 2019; Vittal et al. 2020; Yang and Huang 2021). First, a basin-warming mode exists in the tropical AO and is known as Atlantic Niño or the Atlantic Zonal Mode (AZM; Lübbecke et al. 2018; Cabos et al. 2019; Richter and Tokinaga 2021). These Atlantic Niños peak during boreal summer and are formed due to a Bjerknes feedback as for ENSO, but last only for 3-4 months due to the weaker ocean-atmosphere interactions in this basin (Lübbecke et al. 2018; Cabos et al. 2019; Richter and

Tokinaga 2021). It is still debated whether and how ENSO affects the AZM (Tokinaga et al. 2019). However, Atlantic Niños give rise to important shifts in local rainfall and are associated with a Matsuno-Gill atmospheric response during boreal summer (Gill 1980; Kucharski et al. 2009; Li et al. 2016; Jiang and Li 2021), which may modulate the tropospheric temperature gradient in the Indo-Pacific sector and ISMR (Kucharski et al. 2009, Pottapinjara et al. 2014, 2016; Sabeerali et al. 2019; Jiang and Li 2021). The second leading mode of tropical AO SST variability involves fluctuations of the interhemispheric SST gradient in the AO and is known as the Atlantic Meridional Mode (AMM; Chiang and Vimont 2004; Jiang and Li 2021). The AMM is triggered and sustained by a Wind-Evaporation-SST (WES) feedback (Chiang and Vimont 2004; Cabos et al. 2019). However, the Tropical North Atlantic (TNA) SST anomaly dominates AMM variability (Enfield and Mayer 1997; Jiang and Li 2021) and ENSO plays a dominant role in causing the spring time trade wind variability over the TNA and the generation of local SST anomalies by evaporative cooling/warming through ENSO teleconnections (Enfield and Mayer 1997; Garcia-Serrano et al. 2017; Jiang and Li 2019). A few studies also suggest a link between the AMM or warm SST TNA anomalies and ISMR (Vittal et al. 2020; Yang and Huang 2021).

An important difficulty for assessing the role of AO on ISMR, is that it interacts also directly with the PO and IO in a complex manner and at different time scales (Kucharski et al. 2009, 2011; Rodriguez-Fonseca et al. 2009; Ham et al. 2013ab, McGregor et al. 2014, 2018; Li et al. 2016; Terray et al. 2016; Wang et al. 2017; Cai et al. 2019; Li et al. 2020; Jiang and Li 2021; Zhang and Han 2021). Recent studies suggest that warm TNA and AZM SST anomalies can force a La Niña-like SST pattern in the Pacific (Rodriguez-Fonseca et al. 2009; Ding et al. 2012; Ham et al. 2013ab; Wang et al. 2017; Jiang and Li 2021). But, again the role of AO in ENSO and ISMR is debated in the literature (Ding et al. 2012; Zhang et al. 2021b; Richter et al. 2021). As an illustration, previous studies suggest that Altantic Niños may reduce ISMR (Kucharski et al. 2007, 2009; Pottapinjara et al. 2016), but at the same times it may promote La Niña conditions over the Pacific (Rodriguez-Fonseca et al. 2009; Ding et al. 2012; Jiang and Li 2021), which will be associated with enhanced ISMR. Therefore, it is difficult to isolate the net effect of AO SST anomalies as the players, ISM, ENSO and AO modes interact with each other in multiple different ways (Kucharski et al. 2009; Ding et al. 2012; Ham et al. 2013b; Cai et al. 2019; Jiang and Li 2021; Yang and Huang 2021).

This review highlights that there are two pathways by which the AO SSTs can affect ISMR, one by a "direct" forcing on the ISMR and the other, "indirect", by the AO forcing on ENSO, which, in turn, will modulate the ISMR. However, as noted above, these two pathways are not really independent of each other and the complexity of these interactions implies that it is very difficult to assess the distinct causal relationships between the Atlantic, Indian and Pacific SSTs and ISMR, or even the net effect of AO SSTs on ISMR from observations alone. Considering these difficulties, we will assess the role of the tropical AO on ISMR with the help of dedicated experiments performed with a Coupled General Circulation Model (CGCM).

This paper is organised as follows. The validation datasets, CGCM and sensitivity experiments used in this study are described in Section 2. In Section 3, the observed and simulated relationships between ISMR, ENSO and AO SSTs at the interannual time scale are documented. In Section 4, the AO “direct” and “indirect” effects on ISMR are assessed through sensitivity coupled experiments. The final section summarizes the results of the present work and presents some perspectives.

2. Datasets, coupled model and sentivity experiments

2.a Observed datasets and time series indices.

Multiple data sources are used for model validation. SST and atmospheric variables (e.g., 850- and 200-hPa winds, velocity potentials and stream functions) are taken or computed from ERA-Interim reanalysis (ERAi; Dee et al. 2011) available from 1979 onwards. The depth of the 20°C isotherm (Z20) is used as a proxy of the thermocline depth and is extracted from the Simple Ocean Data Assimilation reanalysis for the 1979-2010 period (Carton and Giese 2008; SODA version 2.2.4). We also used the Global Precipitation Climatology Project rainfall dataset (GPCP; Huffman et al. 2001), which combines measures of precipitation gauges and satellite data. GPCP is analyzed for the 1979-2016 period. All these quantities are interpolated onto the model resolution to foster direct comparison with the simulations.

To monitor ISM, ENSO and AZM variability both in observations and simulations, we define three standard time series indices:

- The ISMR time series is defined as the average of rainfall anomalies for the land grid points in the region 5°-25°N and 70°-95°E.

- The Niño-3.4 SST (monthly average of SST anomalies in the region 5°S-5°N and 170°-120°W; Nino34 hereafter) time series is chosen for the ENSO index since in observations the strongest correlations between ISMR and tropical Pacific SSTs occur over this region.

- The ATL3 SST (monthly average of SST anomalies in the region 3°S-3°N and 20°W-0°E) time series, which is a convenient index for the AZM (Lübbecke et al. 2018).

Note that our analysis of observations is robust if we estimate our Nino34, ATL3 and ISMR time series from the Hadley Centre Sea Ice and SST dataset (Rayner et al. 2003) and the rainfall dataset obtained from the Indian Meteorological Department (Pai et al. 2015).

2.b Coupled model and sensitivity experiments.

Here we employ a CGCM, the SINTEX-F2 (Masson et al. 2012), to assess the influence of AO on ISMR variability and the ISM-ENSO relationship. The different model components are ECHAM5.3 atmospheric model (Roeckner et al. 2003) at T106 spectral resolution (~1.125° x 1.125°) and 31 hybrid sigma-pressure levels, NEMO ocean model (Madec 2008) at 0.5° x 0.5° horizontal resolution, 31 vertical levels and the LIM2 ice model (Timmermann et al. 2005). The three model components are coupled using the Ocean-Atmosphere-Sea-Ice-Soil (OASIS3) coupler (Valcke 2006). The model simulates the tropical Pacific SST mean state, ENSO and ISMR variability reasonably well (Masson et al. 2012, Terray et al. 2016, 2021; Cretat et al. 2017, 2018).

First, a 210-yr fully coupled ocean-atmosphere simulation is used as a control (CTRL hereafter). In order to disentangle the complex interactions between ISMR, ENSO and AO SST variability, two partially coupled configurations of SINTEX-F2 are used and two dedicated experiments have been performed with each of these configurations (see Table 1 for details). In the first partial coupled configuration, full ocean-atmosphere coupling is used everywhere except in the subtropical and tropical AO (25°S-25°N band), where SST is nudged toward a daily SST climatology computed from CTRL or AVHRR-V2 daily Optimum Interpolation SST observations during the 1982-2010 period (Reynolds et al. 2007). These two AO decoupling experiments will be called FTAC and FTAC-obs and have been run for 110-yr and 50-yr, respectively. In the second partial coupled configuration, ocean-atmosphere coupling is active except in the subtropical and tropical Pacific (25°S-25°N band) where, again, SST is nudged toward a daily SST climatology computed from CTRL or observations. These two PO decoupling experiments will be called FTPC and FTPC-obs, and have been run for 110-yr and 50-yr, respectively.

The nudging method used in these partial decoupling experiments modifies the non-solar heat fluxes in the selected domain through a correction term that completely removes the SST variability in the nudging domain (Terray et al. 2021). The damping term used in this nudging technique (-2400 W m^{-2} K^{-1}) corresponds to the 1-day relaxation time for temperature in a 50-

m ocean layer. To avoid sharp SST gradients, a buffer zone is used between the "free" ocean and regions of prescribed SST forcing such that the SSTs in these buffer regions are gradually merged (over 5° latitude) with the prescribed SSTs. This strong SST restoring leads to an almost complete decoupling between the ocean and atmosphere in the nudging domain with SSTs, which differ by no more than 0.1 K from the prescribed space-time climatology.

In FTAC and FTPC, there are no significant changes in SST mean-state in the nudged region, but also in the whole Tropics compared to CTRL (not shown). On the other hand, in FTAC-obs (and also FTPC-obs), the strong SST restoring removes the SST mean-state biases present in CTRL in addition to suppressing SST variability in the selected domain. CTRL exhibits a strong warm bias in the southeast AO (Fig. 1a), which is a common problem for most CGCMs (Richter et al. 2014; Voldoire et al. 2019; Bi et al. 2022). This bias is attributed to errors in simulating zonal trade winds during boreal spring and is related to a deeper thermocline, which weakens the upwelling of cold waters in the eastern AO (Fig. 1b). Consistent with this erroneous east-west SST gradient, the rainfall pattern in the tropical AO is shifted southeastward in CTRL compared to observations (Fig. 1c). Also consistent with these mean-state biases, CTRL simulates a weaker SST variability over the eastern equatorial AO compared to observations (Fig. S1b), especially during boreal summer, which is the season of maximum SST variability in observations (Fig. S1a) as this is also the season when the (observed) thermocline is the shallowest. Focusing on the PO, we note that CTRL is also affected by a double Inter-Tropical Convergence Zone (ITCZ) bias (Fig. 1c) and a reduced ENSO amplitude during boreal winter (Fig. S1b). As we will demonstrate in the following sections, the inability of CTRL to realistically reproduce the seasonal cycle in the AO is a cause of concern not only for the AO region, but also for ENSO and ISMR.

On the other hand, the SST restoring applied in FTAC-obs is able to correct largely these simulated SST, thermocline and rainfall errors in the AO and also produces some changes in the two other tropical basins (Figs. 1d-f). In other words, the comparison of CTRL, FTAC and FTAC-obs (or FTPC and FTPC-obs) runs is useful to isolate the specific contribution of the biased SST background mean-state in the coupled model.

More generally, the aim of these simulations is to isolate the effects of the PO and AO SST variability on the simulated ISMR and ENSO-ISM relationship. First, FTPC and FTPC-obs will be used to assess the « direct » relationship between AO SSTs and ISMR in a climate without any counteracting ENSO forcing. Second, FTAC and FTAC-obs are useful to assess if and how AO SST variability modulates ENSO and the simulated monsoon-ENSO relationship, e.g. if AO SST anomalies are able to produce an « indirect » effect on the ISMR.

Table 1 summarizes the specifications of the simulations used here and the different nudging domains are displayed in Fig. 1a. Finally, in all the analyses described below, the first 10 years of all simulations have been excluded due to the spin-up of the coupled model.

3. ISMR, ENSO and AO relationships in observations and SINTEX-F2

3.a AO SST variability and its relationship with ENSO in SINTEX-F2

Before assessing the role of AO SST variability on ISMR and its relationship with ENSO, it is important to document the performance of SINTEX-F2 in simulating AO variability, especially the AZM and AMM (see Introduction for details). In this way, we can first appreciate if the SST, rainfall and Z20 mean-state biases discussed in Section 2 are also a cause of concern for a realistic simulation of AO SST variability in CTRL. Such analysis will also be useful to interpret the differences between the AO decoupled experiments and CTRL in the following sections as the nudged AO region encompasses the tropical AO.

AZM and AMM are the two dominant modes of SST monthly anomalies in the tropical AO (Lübbecke et al. 2018; Cabos et al. 2019 and references herein). Thus, Empirical Orthogonal Function (EOF) analysis of observed and simulated tropical AO SST monthly anomalies provides a convenient tool for describing the performance of CTRL in simulating both the AZM and AMM modes and their relative importance. Note also that the different datasets have been detrended before the EOF analysis. Fig. 2 displays the first two leading EOFs of observed and simulated monthly SST anomalies in the tropical AO. These two EOFs of ERAi and CTRL SSTs are clearly distinct from the lower EOFs as EOF3 accounts for only 8% of the AO SST variance in both ERAi and CTRL (not shown).

The first EOF of ERAi SSTs describes 25% of the AO SST variance and depicts a basin-wide pattern with positive SST anomalies covering the whole tropical AO (Fig. 2a). However, the spatial loadings in this EOF1 are particularly high in the coastal upwelling regions near the Angola–Benguela coast and in the equatorial cold tongue region explaining why this first EOF is usually associated with the AZM in the literature (Lübbecke et al. 2018; Cabos et al. 2019; Jiang and Li 2021). The second EOF of ERAi SSTs accounts for 23% of the AO SST variance (Fig. 2b). This EOF2 depicts a cross-equatorial SST gradient in the AO, which is usually interpreted as the manifestation of the AMM (Chiang and Vimont 2004; Cabos et al. 2019). These two leading EOFs are very similar to other published EOF analysis of AO SSTs using different datasets, spatial domains or time periods, both in terms of spatial patterns and variance described by these leading modes (Lübbecke et al. 2018; Cabos et al. 2019; Jiang and Li 2021). Of special interest is the possible connection of these two leading EOFs with ENSO, which is simply assessed here by computing the simultaneous correlation between the associated amplitude monthly time series and the Nino34 index. These observed EOF modes have no simultaneous relationship with ENSO (r=-0.07 and 0.08 for Nino34 vs EOF1 and EOF2, respectively). Their lead and lag relationships with Nino34 index will be explored in Section 3.c.

Figs. 2cd display the two leading EOFs of CTRL SST monthly anomalies in the same AO domain, which explain, respectively, 28 and 16% of the SST variance. SINTEX-F2 is able to simulate with a reasonable accuracy both the spatial patterns and variances described by the leading EOFs of observed AO SSTs as well as their relative importance in term of explained variance. Note, however, that the L-shaped structure of the anomalous SSTs linking the equatorial cold tongue to the southeast AO in EOF1 of observed SSTs is not well represented and shifted westward in the EOF1 of simulated SSTs. This suggests that AZM events may be weaker and are partly disconnected from the upwelling region near the Angola–Benguela coast in CTRL compared to observations. This error is further confirmed by the comparison of observed and simulated SST monthly means and standard-deviations in the ATL3 region (Fig. 3). Consistent with Fig. 1a, ATL3 region is affected by a warm mean-state bias, which is particularly prominent during June-July when the observed ATL3 SST variability is maximum (Fig. 3), which corresponds to the peak of AZM events in observations (Lübbecke et al. 2018). By contrast, the simulated ATL3 SST variability is prominent around three months earlier and is drastically reduced in amplitude. This shortcoming, which is also found in many other CGCMs (Voldoire et al. 2019; Bi et al. 2022), is related to the coupled mean-state biases (e.g., SST, Z20, rainfall, etc.) reducing the intensity of the equatorial cold tongue during boreal summer in CTRL, especially the flatten thermocline in the equatorial AO, which may reduce the thermocline feedback and, thus, weakens the local Bjerknes feedback and the AZM variability (see Figs. 1 and S1). The observed ATL3 SST variability has also a secondary peak in winter, but this weaker maximum is well simulated in CTRL (Fig. 3b). On the other hand, the second EOF of simulated AO SSTs closely matches the second EOF estimated from ERAi SSTs in terms of spatial pattern and can also be regarded as the manifestation of the AMM (Figs. 2bd). Finally, the correlations between the associated two amplitude time series and the Nino34 index in CTRL are, respectively, 0.36 and 0.01, and the first correlation is highly significant, even at the 99.9 % confidence level according to a phase-scrambling bootstrap test (Ebisuzaki 1997). This suggests a significant association of the simulated AZM with ENSO in CTRL, which is not found in observations (see above). On the other hand, EOF2 of (simulated) AO SSTs, which can also be regarded as the manifestation of the AMM, is not significantly associated with ENSO in CTRL; a result consistent with observations.

In summary, the two leading modes of the tropical AO SST variability in CTRL share many features with those in observations, but the simulated AZM has a much weaker amplitude and a significant relationship with ENSO, suggesting a too strong ENSO teleconnection to the tropical AO or vice versa.

3.b ISMR regression analysis

We now present the results of a lead-lag regression analysis of tropical SST, rainfall, 850-hPa wind and 200-hPa velocity potential quarterly time series onto the ISMR index in order to provide a clear picture of the relationships between ISMR, ENSO and AO climate variability in observations and CTRL (Figures 4 and 5). The ISMR index is fixed at the JJAS season and the 4-month averaged SST, rainfall, 850-hPa wind and 200-hPa velocity potential time series are shifted backward and forward in time. The results are presented in a two-year window from the beginning of year -1 (preceding the ISMR year) to the end of year 0, year 0 referring to the year of the ISM season. Note that the results remain unchanged if the different time series are detrended before the regression analysis (not shown). While it is known that the ISM-ENSO relationship includes some asymmetry in observations (Terray et al. 2003, 2005; Boschat et al. 2012; Chakraborty and Singhai 2021), this regression analysis is used here as a first order method to assess the realism of CTRL in simulating the ISMR teleconnections.

The regression results from observations (Fig. 4) illustrate that ISMR is associated with different phases of ENSO in a two-year window (Boschat et al. 2012; Chakraborty 2018). Strong positive SST anomalies in the central and eastern PO, which are out of phase with anomalies in the western part of the PO are found during year -1, consistent with the occurrence of an El Niño one year before a strong ISM (Fig. 4a). The atmospheric anomalous patterns are consistent with this hypothesis as they describe an eastward shift of the Pacific Walker circulation with persistent westerly 850-hPa wind anomalies over the western equatorial Pacific, positive rainfall anomalies and negative 200-hPa velocity potential anomalies over the central Pacific during year -1 (Figs. 4bc). The regression patterns during year 0 are more or less a mirror image of those during year -1 with an opposite sign (Fig. 4). In other words, this analysis demonstrates that ENSO and ISMR are still highly inter-related and followed a sustained biennial rythm during recent decades (Meehl et al. 2003; Terray et al. 2003, 2021).

Focusing now on the relationships between ISMR and IO SSTs, we note that IO SST anomalies are small and insignificant during boreal winter of year -1 and the pre-monsoon period of year 0. During boreal summer of year 0, the IO is also devoid of any significant SST anomalies associated with ISMR variability (Fig. 4a). This suggests that the « direct » effect of IO SSTs on ISMR is small (Cretat et al. 2017; Terray et al. 2021).

On the other hand, a significant positive correlation emerges between TNA SSTs during boreal spring of year 0 and ISMR (Fig. 4a). This result is in agreement with the results of Vittal et al. (2020), Yang and Huang (2021) and Ham et al. (2013ab), which suggest that TNA SSTs during boreal spring are a significant precursor of ISMR and can also serve as a trigger for the following La Niña event, respectively. However, this statistical relationship quickly fades away during boreal summer of year 0 (Fig. 4a). Furthermore, during ISM, the SST anomalies are insignificant in the tropical AO, which partly disagree with recent studies highlighting the role of AZM on the ISMR (Kucharski et al. 2007, 2009; Pottapinjara et al. 2014), but are in agreement with the work of Ding et al. (2012).

In order to further elucidate the relationships between tropical SSTs, ENSO and ISMR in observations, the above lead-lag regression analysis has been repeated after removing the ENSO contribution to the monthly SST fields by a simple linear regression method (Fig. S2a). This is equivalent to assume that ENSO has a simultaneous linear impact on tropical SSTs (Kucharski et al. 2009). Despite the simplicity of this approach, the results demonstrate that most of the lead-lag relationships between tropical SST anomalies and ISMR (displayed in Fig. 4a) can be understood as the results of simultaneous ENSO teleconnections on both ISMR and SST anomalies elsewhere, as most of the correlations are now insignificant, especially those during boreal summer of year 0 (Fig. S2a). One notable exception is, however, again the TNA SSTs during boreal spring of year 0, which remain significant at the 90% confidence level even after removing the ENSO contribution from the observed SST fields. On the other hand, despite the independence of AZM and ENSO in observations (see Section 3.a) and removal of the ENSO-related contribution to the SST anomalies, the tropical AO SSTs are again not linearly linked to ISMR during year 0.

CTRL is performing relatively well in reproducing the simultaneous inverse relationship between ISMR and ENSO during year 0 (Fig. 5). However, the model fails to reproduce the significant positive lead correlation between TNA SSTs during boreal spring and the following ISM. Also, ISMR is much more linked to ENSO during year -1 and the pre-monsoon season of year 0 in CTRL (Fig. 5; see also Terray et al. 2021). This suggests an overly strong control of ENSO on ISMR in CTRL as for the AZM (see Section 3.a above). Removing the ENSO contribution to the CTRL monthly SST fields by a simple linear regression method before the regression analysis reveals a significant contribution of the subtropical North Pacific SST anomalies during year 0, but again no significant relationships with TNA or tropical AO SSTs during year 0 (Fig. S2b).

In the context of the ENSO-ISM relationship, the physical consistency of a direct link between TNA SSTs during boreal spring and ISMR independent of ENSO, as found in observations, is thus questionable. This positive correlation between TNA SSTs during boreal spring and ISMR may be more an artifact of the ENSO forcing on both TNA and ISMR than a sign of a physical connection between TNA SSTs and ISMR (Zhang et al. 2021b). This alternative scenario is also consistent with the significant La Niña SST and atmospheric patterns during year 0, associated with the ENSO biennial rhythm during recent decades (Fig. 4a; Wang et al. 2017), and the insignificant atmospheric anomalous patterns over TNA during boreal spring of year 0 in our ISMR regression analysis from observations (Fig. 4bc).

3.c Nino34 regression analysis

We now revisit the two-way interactions between AO SSTs and ENSO for a better understanding of the AO SSTs and ISMR relationships. Figures S3 and S4 show the lead-lag regressions between the Nino34 index during boreal winter (e.g., ONDJ season) and tropical SST, rainfall and 850-hPa wind anomalies, again during a two-year window, in both observations and CTRL. In the following discussion, we will refer to year 0 as the developing year and year +1 as the decaying year of ENSO events, respectively. CTRL reproduces reasonably well the observed lifecycle of ENSO events with El Niño onset during boreal spring, a developing phase during boreal summer and fall, a peak phase during boreal winter and a decaying phase during boreal spring and summer of year +1 (Fig. S3).

The SST and atmospheric anomalous patterns during ENSO onset (e.g., during boreal spring of year 0) are very similar in observations and CTRL and are reminiscent of the Seasonal Footprinting Mechanism (SFM; Vimont et al. 2003; Boschat et al. 2013). We also note significant cold SST anomalies in the tropical AO and TNA during boreal spring of year 0 (especially in observations see Fig. S3a) consistent with past studies (Rodriguez-Fonseca et al. 2009; Ham et al. 2013ab; Jiang and Li 2021). Ham et al. (2013a) argues that these TNA SST anomalies may influence the tropical PO and that this forcing is mediated by the SFM (Fig. S4a). Such TNA forcing on El Niño onset is also suggested in CTRL, but with much weaker amplitude (Figs. S3b and S4b).

A first notable difference between CTRL and observations is that simulated ENSO teleconnections are significantly stronger than observed, as illustrated by the enhanced IO and AO basin-wide warming in CTRL at the end of year 0 (Fig. S3b). The rainfall response over the central equatorial Pacific per °C of Nino34 warming during boreal winter of year 0 is much stronger in CTRL; about 5 mm/day per °C against only 2.6 mm/day per °C in observations (Fig. S4). The associated latent heating induces an enhanced tropospheric warming, which stabilizes the atmosphere and reduces convection, cloudiness and evaporation over the AO and IO more in CTRL than in observations (not shown; Chiang and Sobel 2002; Chang et al. 2006).

The climate anomalies during year +1 depict the transition from El Niño to La Niña (or vice versa since the analysis is linear) and the related changes in ENSO teleconnections (Figs. S3 and S4). First, the simulated and observed SST anomalies during boreal winter of year 0 and spring of year +1 show that most warm TNA events can be initiated by ENSO itself (see Fig. S3; Garcia-Serrano et al. 2017; Jiang and Li 2019). This TNA warming is mainly driven by the weakening of the local northeasterly trade winds during FMAM of year +1 in both observations and CTRL (Fig. S4). These warm TNA events may induce wind anomalies over the tropical Pacific that oppose the ongoing ENSO event and accelerate its demise (Ham et al. 2013ab). This TNA forcing can be interpreted as a delayed negative feedback that accelerates the decay of ENSO as the IO capacitor effect (Xie et al. 2009, 2016; Wang et al. 2017). This is consistent with many previous CGCM studies, which found that decoupling the IO or AO in CGCMs increases the length of ENSO events (Ohba and Ueda 2007; Santoso et al. 2012; Terray et al. 2016, 2021; Kajtar et al. 2017).

A second notable difference between CTRL and observations is that, despite this stronger ENSO-induced capacitor effect over the tropical IO or AO in CTRL, the simulated ENSO signal in the tropical Pacific lasts longer and persists well up to boreal summer and fall of year +1 in CTRL (Fig. S4b). This contradiction has already been examined in Terray et al. (2021) and their results highlight that, besides the amplitude of the basin-wide IO warming, the intensity of the negative IO feedback on ENSO is heavily dependent on the realism of the equatorial SST gradient in the IO during the ENSO peak and decaying phases. An open question, which will be examined with the help of partial decoupling experiments in the following section, is to determine if the erroneous mean equatorial SST gradient in the AO (Fig. 1a) is also playing a role in the longer ENSO period in CTRL.

In summary, this section illustrates how it is difficult to isolate the specific effect of AO SST anomalies on ISMR in observations or coupled simulations as the three players, ISM, ENSO and the AO SST modes, interact with each other in a complex manner.

4. AO direct and indirect effects on ISMR in SINTEX-F2

In order to assess both the possible “direct” and “indirect” effects of AO SSTs on ISMR, we now focus on the analysis of the partial decoupling experiments described in Section 2b.

4.a AO direct effect on ISMR

We estimate the "direct" effect of AO SST variability on ISMR with the help of the PO decoupling experiments in which ENSO has been removed.

In order to document how the simulated AO SST variability is modified in the absence of ENSO, Fig. 6 displays the first two EOFs of tropical AO SST anomalies simulated in the two PO decoupling experiments. We first note that these leading EOFs estimated from FTPC and FTPC-obs are very similar both in terms of spatial pattern and described variance. EOF1 (EOF2) is associated with SST variability to the South (North) of the Equator and the Angola–Benguela (Senegal-Mauritania) upwelling system. This suggests that, in both PO experiments, these EOFs are excited by wind-driven evaporation or dynamic in each hemisphere, but that they do not involve an active WES feedback, which is usually associated with the AMM (Chiang and Vimont 2004; Cabos et al. 2019).

These EOFs can be compared to those estimated from CTRL, which are shown in Figs. 2cd. Consistent with the overly strong ENSO forcing on the simulated AZM found in CTRL (e.g., EOF1 of CTRL SSTs in Fig. 2c), the leading EOFs in the PO experiments are no more associated with SST variability in the equatorial AO and they further suggest that the two poles of the AMM may vary independently of each other. This questions the physical consistency of the AMM and its underlying mechanism, both in observations and CTRL, as its inter-hemispheric SST dipole structure depicted by the EOF2 of (observed and CTRL) AO SST anomalies may result from orthogonality constraints of the EOF analysis rather than the consequence of an active WES feedback.

The specific role of this “ENSO-free” AO SST variability in modulating ISMR is illustrated by a regression analysis of simulated SST and 200-hPa velocity potential anomalies onto the ISMR index during year 0 (Figure 7). We focus on FTPC-obs in the rest of this section, as the results from FTPC are similar (not shown). Overall, the direct forcing of

AO SST and atmospheric variability on ISMR is insignificant as the AO is devoid of any significant SST or atmospheric anomalies during the pre-monsoon season (e.g., FMAM of year 0) in FTPC-obs (Fig. 7). On the other hand, a well-defined atmospheric teleconnection pattern exists during boreal summer with strong 200-hPa divergence and outflow anomalies from the ISM region towards the south AO in FTPC-obs (Fig. 7b). This upper-level velocity potential pattern is obviously triggered by the diabatic heating associated with ISMR and demonstrates that ISM is a dominant feature of the boreal summer tropical circulation in the absence of ENSO. Interestingly, this ISMR forcing on the AO during boreal summer also promotes an AMM-like SST pattern during boreal fall with negative (positive) SST anomalies in the South (North) AO (Fig. 7a). This leads to the hypothesis that it is ISMR, which is forcing the AO rather than the reverse in the absence of ENSO.

4.b AO forcing on ENSO

The aim of this subsection is to isolate the effect of the AO SST mean-state bias and variability on ENSO with the help of the FTAC and FTAC-obs simulations.

To have a first basic understanding of the ENSO behavior in these two runs, Figure 8 shows the Nino34 SST monthly standard deviations from observation, CTRL and the two AO decoupled experiments. The observed Nino34 SST variability is most prominent during boreal winter (std of about 1.2°C), and it is drastically reduced in April (about 0.6°C), which marks the onset of many ENSO events (Fig. 8). CTRL underestimates the Nino34 SST variability during boreal winter when ENSO events usually peak (Figs. 8 and S1). It is also not able to replicate the sharp decrease of Nino34 SST variability after the ENSO peak and, hence, there is an overestimation of the simulated Nino34 SST variability for a few months from March till July (Fig. 8). One interesting result is how the AO decoupled experiments alter this Nino34 SST variability (Frauen and Dommenget 2012; Ding et al. 2012; Kajtar et al. 2017). The Nino34 SST variability changes in FTAC and FTAC-obs include (i) a consistent increase during boreal summer for the two runs and (ii) an enhanced variability during boreal winter and a more realistic seasonal phase-locking in FTAC-obs compared to both CTRL and FTAC (Fig. 8).

We first focus on the increase of Nino34 SST variability during boreal summer, which is found in both FTAC and FTAC-obs (Fig. 8). In order to explain this feature, Figure 9 shows the regressions between the Nino34 index during boreal winter of year 0 (e.g., ONDJ season) and tropical SST, rainfall and 850-hPa wind anomalies during the preceding boreal winter and spring (e.g., FMAM) in FTAC and FTAC-obs. As discussed in Section 3, boreal spring is the season of El Niño onset and the results suggest that the SFM in the North Pacific plays a key-role in ENSO onset in both observations and CTRL (Figs. S3 and S4). A robust association between the SFM and El Niño onset is also found in the two AO decoupled experiments (Figs. 9ab). But, this El Niño onset occurs during boreal winter of year -1, e.g., one season before the El Niño onset in CTRL and observations, and one year before the El Niño peak (Fig. 8), a feature, which has not been well documented in past studies (Frauen and Dommenget 2012; Terray et al. 2016; Kajtar et al. 2017). Furthermore, warm SST anomalies already cover the whole central and eastern equatorial PO during boreal spring of year 0 in these two runs (Figs. 9cd), e.g. also one season in advance compared to observations or CTRL in which this basin-wide SST anomalous pattern is seen in boreal summer (Fig. S3). The associated rainfall and 850-hPa wind regression patterns during boreal spring of year 0 in FTAC and FTAC-obs also describe an eastward shift of the convection center with positive (negative) rainfall anomalies over the central (western) PO and westerly zonal wind anomalies on the western side of the positive rainfall anomalies (Figs. 9ab). All these features are fully consistent with the early El Niño onset in FTAC-obs and FTAC. Note, furthermore, that the rainfall and 850-hPa regression patterns during boreal winter and spring preceding the ENSO peak are very similar in the two AO decoupled experiments (Figs. 9ab). This suggests that this early El Niño onset can be attributed to the common cancellation of the AO SST variability in the two runs. This early El Niño onset also implies that the warm Nino34 SST anomalies associated with El Niño are already well defined during boreal summer of year 0 consistent with the enhanced Nino34 SST variability during boreal summer found in the two nudged experiments (Fig. 8). These results illustrate the important role played by AO SST variability in generating spread in ENSO timing and amplitude through its influence on the SFM. This is also consistent with several recent studies, which suggest that the SFM and its modulation are an important source of spread in ENSO forecasts during boreal spring and early summer (Ma et al. 2017; Ogata et al. 2019).

We now focus on the improved phase-locking and enhanced ENSO variability during boreal winter found in FTAC-obs (Fig. 8). In order to illustrate the seasonal dependence in the changes of ENSO variability in the different runs and isolate the role of the AO background state, Figure S5 displays the seasonal differences of SST standard-deviation between FTAC-obs and both CTRL and FTAC. Figs. S5a-c first confirm that almost all the tropical AO SST variability has been removed in FTAC-obs. Outside the AO nudged region, the SST variability changes in FTAC-obs relative to CTRL are mainly found in the tropical PO in the form of an enhanced ENSO variability from boreal summer to winter (Figs. S5b-c). This is consistent with the changes of Nino34 SST variability (Fig. 8). Furthermore, a large part of these differences can be attributed to the corrected SST AO mean state as this seasonal pattern of changes is also found in the differences of SST standard-deviation between FTAC-obs and FTAC (Figs. S5d-f). In other words, decoupling the AO SST variability without restoring the observed AO SST climatology leads only to a modest increase of ENSO variability, especially during its peak phase (Fig. 8).

In order to understand why the AO background state has such an impact on ENSO, Figure S6 displays the seasonal differences between FTAC-obs and CTRL climatologies of SST, rainfall and Z20, and Figure 10 shows boreal spring differences of 850- and 200-hPa zonal wind, velocity potential and stream function climatology between the same runs. The differences between FTAC-obs and FTAC are similar as FTAC and CTRL have the same mean state (not shown).

The correction of AO SST biases in FTAC-obs leads to drastic improvements of AO rainfall and Z20 spatial distributions during all the seasons with enhanced precipitation in the northwest tropical AO, reduced precipitation in the southeast tropical AO and, finally, a deeper Z20 in the western AO (Figs. S6bc). These rainfall changes are consistent with the imposed AO SSTs in FTAC-obs altering the regions that are above or below the threshold for deep convection in FTAC-obs compared to CTRL or FTAC (Fig. S6a). An increase of precipitation is also evident over the Amazon basin demonstrating that the reponse is not purely local. These AO rainfall shifts may exert an influence on atmospheric teleconnections because they alter diabatic heating (e.g., Gill 1980). However, surprisingly, while these rainfall changes are significant during all seasons, the rectification of the tropical PO mean state is mainly prominent during boreal spring and is characterized by a shift to an El Niño-like mean state with a warmer (cooler) eastern (western) equatorial PO, a rainfall increase in the central PO near the date line, a flatter thermocline (Figs. S6abc, first row) and, finally, a slowdown of the mean Walker circulation across the tropical PO (Figs. 10ab). The westward shift of rainfall over the AO may produce large heating anomalies at upper level centered over central South America and extending in the eastern and central PO. The 850- and 200-hPa velocity potential differences during boreal spring are in agreement with this hypothesis as they show enhanced convergence (divergence) at 850-hPa (200-hPa) toward a large region encompassing the central equatorial PO and the northwest AO and the opposite patterns elsewhere in the Tropics (Figs. 10cd). The well-defined quadrupole structure of the 850- and 200-hPa stream functions over the eastern PO/western AO (Figs. 10ef) is further consistent with the circulation expected from a Matsuno-Gill response (Gill 1980; Kucharski et al. 2009;

Li et al. 2016). These features directly link SST mean-state changes in the AO with the rectification of the Pacific mean state during boreal spring. Such strong inter-basin connectivity is not seen in the other seasons despite that AO rainfall changes are still prominent (Fig. S6b). This may be related to the ITCZ and Walker cells in all oceanic basins being closer to the Equator during boreal spring, thus providing ideal conditions for the corrected rainfall and SST patterns in the tropical AO to influence the equatorial PO (Chang et al. 2006; Tokinaga et al. 2019).

Not surprisingly, the rainfall and 850-hPa zonal wind variability is also significantly enhanced and shifted eastward in the PO during boreal spring in FTAC-obs (Figs. 11ac), while the related changes are weak in FTAC (Figs. 11bd). This is consistent with the eastward shift of the mean PO SST and rainfall patterns during the same season in FTAC-obs (Figs. S6ab). Furthermore, the changes of rainfall and 850-hPa zonal wind variability over the AO are opposite in FTAC and FTAC-obs, with a large increase (decrease) of rainfall and 850-hPa zonal wind variability over the tropical AO during boreal spring in FTAC (FTAC-obs) despite the absence of AO SST variability in the two runs (Fig. 11). This again highlights strong interactions between the biased AO SST mean-state and atmospheric variability in FTAC, which may further perturb the ENSO onset. In other words, the El-Niño like changes of the PO mean state in FTAC-obs provide more favorable conditions for El Niño to develop through the Bjerknes feedback (e.g., a reduced equatorial SST gradient and a flatter thermocline across the PO) and reduced atmospheric noise over the AO during boreal spring. This finally leads to a much better seasonal phase-locking of the simulated ENSO and an improved ENSO amplitude during its peak phase in FTAC-obs in comparison of CTRL and FTAC (Fig. 8).

Finally, the AO decoupled experiments demonstrate that the AO SST variability significantly modulates ENSO during its decaying phase. This is illustrated by the regression analysis of the ONDJ Nino34 index with quarterly SST time series during the following year (e.g., year +1) in FTAC-obs (Fig. 12). FTAC displays a very similar evolution (not shown). The corresponding regression analyses for observations and CTRL are shown in Fig. S3. The warm SST PO pattern lasts longer in FTAC-obs (and FTAC) than in CTRL and the ENSO signal is still robust at the end of year +1 in this run (Fig. 12c). Overall, the results highlight that the ENSO-induced AO SST anomalies in CTRL (Fig. S3b), which are on the other hand very small in the FTAC-obs by design (Fig. 12), accelerate the transition from El Niño to La Niña (in CTRL) during year +1.

4.c AO indirect effect on ISMR

The AO "indirect" effect on ISMR, mediated by the ISM-ENSO relationship, is now explored again with the help of the AO decoupled experiments.

Figure 13ab shows the ISMR seasonal cycle and monthly standard deviations from observation, CTRL and the two AO decoupled experiments. The ISMR seasonal cycle is not altered in the nudging experiments, and they replicate the same results of CTRL (Fig. 13a). Observed ISMR variability is characterized by a double peak at the onset and withdraw of ISM (Fig. 13b). CTRL underestimates ISMR variability in the pre-monsoon season and overestimates it during June-August. The nudging experiments reduce the simulated ISMR variability during the last half of ISM, especially FTAC-obs (Fig. 13b), despite ENSO is stronger during boreal summer in FTAC and FTAC-obs (Fig. 8).

To assess the AO "indirect" effect, Figure 13c shows the observed and simulated lead-lag correlations between ISMR and Nino34 SST quarterly time series in a three-year window from the beginning of year -1 (preceding the ISMR year) to the end of year +1 (following the ISMR year). Consistent with Fig. 4a, there are significant positive correlations one year before ISM in observations. The sign of the correlation reverses during the pre-monsoon season of year 0 and the correlation gets significantly negative during boreal summer and winter of year 0. These negative correlations fade away during year +1. Thus, the most favorable conditions for a strong ISM are during the transitions from an El Niño during year -1 to a La Niña event in year 0 in agreement with our analysis in Section 3.

CTRL is able to reproduce realistically the significant negative correlation between the ISMR and ENSO during boreal summer of year 0 and the decrease of amplitude of this negative correlation during year +1. However, the model shows large discrepancies from observations with a negative correlation during several months before ISM (Fig. 13c). This bias is again consistent with the results of Section 3. However, the relative success of the model in reproducing the observed simultaneous relationships between ISMR and ENSO is important as the analysis of the nudged experiments can then provide more insights on the precise role of the AO in this system.

In this respect, the lead-lag correlations between ENSO and ISMR are significantly different between the two nudging experiments and CTRL, with a consistent weakening of the simultaneous inverse relationship between ISM and ENSO (Fig. 13c), despite Nino34 SST variability is higher during boreal summer in FTAC and FTAC-obs compared to CTRL (Fig. 8). In FTAC-obs, the simultaneous negative correlation between ISMR and Nino34 SST is not even statistically significant at the 90% confidence level, despite FTAC-obs simulates a stronger ENSO than FTAC. As the warm SST mean-state bias affecting the tropical AO in both CTRL and FTAC is removed in FTAC-obs, these results are consistent with the AGCM experiments performed in Kucharski et al. (2007, 2009) in which a weakening of the monsoon-ENSO relationship is simulated in response to a cooling trend of the tropical AO and allow us to isolate the specific role of the SST AO mean-state biases on the simulated monsoon-ENSO relationship. However, as the simultaneous correlation between ISMR and Nino34 SST is also reduced in FTAC, the reduced AO SST variability in the two runs may also play an important role in the weakening of the inverse relationship between ISM and ENSO in the nudged experiments.

Furthermore, ISMR evolution has different flavors during the ENSO decaying year in each dataset (Figure S7). First, we find more rainfall over the IO during the pre-monsoon season (not shown) and over India and the Arabian Sea during the monsoon of year +1 in observations (Fig. S7a). This is consistent with the warm local SSTs (Fig. S3a) and the fast demise of ENSO induced upper-level subsidence during year +1 in observations (Figs. S7a and 14a). During boreal summer of the ENSO decaying year, the significant 200-hPa velocity potential anomalies are restricted to a regional dipole opposing upper-level divergence over the Arabian Sea to upper-level convergence over the western PO in observations (Fig. 14a). These features are physically consistent with the positive (negative) correlation between precipitation in the Indian (northwest PO) region during ISM of year +1 and the Nino34 index in observations (Fig. S7a). This confirms that with the increase (decrease) of the SST over the Nino34 region during the preceding boreal winter, the ISM of the next year is enhanced (suppressed) or vice versa in observations (Fig 13c; Yang et al. 2007).

CTRL is not able to replicate these precipitation and 200-hPa velocity potential anomalies during year +1 (Figs. S7b and 14b). In CTRL, there is a significant negative correlation between precipitation over the Indian region during the monsoon season of year +1 and Nino34 SST (Fig. S7b). This negative ISMR anomaly is consistent with both the persistent ENSO signal (Fig. S3b) and the (significant) positive 200-hPa velocity potential anomalies over India during boreal summer of year +1 in CTRL (Figs. S7b and 14b).

The effect of removing the AO SST variability on these correlations can now be analyzed (Figs. 14c and S7c), keeping in mind that the ENSO-related SST signal persists even longer and is stronger in FTAC-obs than in CTRL (Fig. 12). Despite this enhanced ENSO forcing, the correlation of Nino34 SST with ISMR during year +1 has vanished and is not significant in FTAC-obs (Fig. S7c). This is consistent with the weakening of the simultaneous ISMR-Nino34 correlation in FTAC-obs (Fig. 13c). The origin of this paradox can be seen from Fig.

S7c, which shows that there is a stronger negative correlation between precipitations over the tropical AO during year +1 with Nino34 SST (during the preceding boreal winter) in FTAC-obs compared to CTRL. Moreover, these negative correlations are also shifted westward in FTAC-obs consistent with the corrected AO mean state in this simulation. This stronger relationship between ENSO and the AO in FTAC-obs during year +1 is further confirmed by the associated 200-hPa velocity potential signal (Fig. 14c). In the 200-hPa velocity potential anomalous pattern during boreal summer of year +1 in FTAC-obs, there is a significant positive correlation over the AO, while the correlation over the Indian region is near zero. This implies that the upper-level divergent flow is mainly from the central PO to the TNA instead toward the Indian region, which results in suppression of rainfall in the AO and a near normal ISM in FTAC-obs. FTAC shows a similar evolution (not shown), but the ENSO-induced subsidence over the AO during boreal summer of the ENSO decaying year is weaker, presumably due to the biased AO SST mean-state in FTAC.

In a nutshell, these last results illustrate that, by artificially removing the SST variability over the tropical AO in the nudged experiments, the ENSO signal is stronger and persists longer during the ENSO decaying year, but the associated upper-level divergent winds will flow mainly from the central PO to the tropical AO, resulting in rainfall suppression in the AO, but only in a weak ENSO forcing on ISM during the ENSO decaying year.

5. Conclusions and discussion

In this study, we use dedicated coupled experiments to isolate both the "direct" and "indirect" effects of AO SSTs on ISMR. The "direct" effect refers to the AO forcing on ISMR in the absence of others dominant forcings like ENSO (Kucharski et al. 2009). The "indirect" effect refers to the AO forcing on ENSO (Rodriguez-Fonseca et al. 2009; Ding et al. 2012; Ham et al. 2013ab; Jiang and Li 2021), which may subsequently affect ISMR through ENSO teleconnections. Furthermore, with the help of these experiments, we also identify the role of AO SST mean-state biases on the simulated ISMR-ENSO relationship.

First, we found that the "direct" effect of AO SST variability on ISMR is insignificant. Overall, the results highlight that ISMR is a major player in the tropical atmospheric circulation in the absence of ENSO, even forcing an AMM SST pattern during boreal fall after ISM, rather than the reverse. Several studies have suggested that the AZM may provide a direct remote forcing on ISMR through a Gill-Matsuno mechanism with a Kelvin wave transporting the signal to the IO (Kucharski et al. 2009; Pottapinjara et al. 2014), but we were not able to isolate this "direct" effect on ISMR in our simulations or observations during recent decades, even when ENSO is removed (Figs. S2 and 7), which is consistent with the modeling results of Ding et al. (2012). However, it is known that current CGCMs struggle to represent this relationship, partly due to their common strong AO SST mean-state biases (Barimalala et al. 2012; Voldoire et al. 2019). Taking into account the warm SST mean-state bias in the southeastern AO found in SINTEX-F2 (see Fig. 1a), the realism and amplitude of the AZM simulated by this CGCM are severely biased (Fig. 3b) and this may also deteriorate the simulated ISMR-AZM relationship in our model.

The global-scale effects of the corrections of tropical AO SST biases are readily apparent when comparing our two AO decoupled experiments with each other and with a long free simulation performed with the same model. When the AO SST mean-state bias (present in CTRL and FTAC) is corrected in FTAC-obs, the rainfall pattern in the AO is shifted northwestward (see Fig. 1f). The associated changes in diabatic heating produce a Matsuno-Gill atmospheric response centered over the eastern equatorial Pacific and generate a trans-basin (e.g., Pacific/Atlantic) atmospheric see-saw with upward motion over a large region encompassing the central and eastern equatorial Pacific and the western tropical AO and descending motion elsewhere in the Tropics. The overall effect is the emergence of an El Niño-like mean-state pattern in FTAC-obs when these AO SST biases are corrected, which is mostly significant during boreal spring (see Fig. S6). This also corresponds to the onset period of El Niño events in observations and the simulations analyzed here.

The comparison of FTAC and FTAC-obs with CTRL suggests that the "indirect" influence of the tropical AO SST variability on ISMR is significant. The main effect of AO SST variability is to modulate the amplitude and length of ENSO events, especially during their onset and decaying phases. First, AO SST variability plays a key-role in ENSO developing phase in agreement with the results of Ham et al. (2013ab). Without AO SST variability, ENSO onset, while still seasonally phase-locked and linked to the SFM over the North Pacific (Vimont et al. 2003; Boschat et al. 2013; Terray et al. 2016), occurs one season before during boreal winter. This finding supports the idea that AO SST variability is also a possible source of ENSO spread, especially during its developing year. This may reduce ENSO predictability and contributes to the spring ENSO predictability barrier (Ma et al. 2017; Ogata et al. 2019). Furthermore, when AO SST mean-state biases are also corrected (e.g., in FTAC-obs), this leads to increased ENSO amplitude during its peak phase (e.g. boreal winter) as well, demonstrating nonlinear interactions between the mean state during boreal spring and ENSO amplitude.

Our results also confirm that AO SST variability modulates the length of the ENSO decaying phase, as ENSO is still active up to the end of the ENSO decaying year in the FTAC and FTAC-obs experiments (Terray et al. 2016; Kajtar et al. 2017). During boreal winter, ENSO influences the subtropical and tropical AO through the atmospheric bridge (Jiang and Li 2019). These ENSO-induced SST AO anomalies may then feedback negatively on ENSO and fasten the transition from El Niño to La Niña. This discharging capacitor effect of the AO (Wang et al. 2017) serves as a phase-reversal mechanism for the ENSO cycle as for the IO (Xie et al. 2009; Terray et al. 2016, 2021).

All these findings are consistent with recent modelling studies that have identified a tight physical linkage between AO and PO variability on decadal timescales (Kucharski et al. 2011) or in a global warming context (McGregor et al 2014) and also demonstrate that the prominent AO SST biases play a significant role in modulating the simulated Pacific Walker circulation at both the seasonal and longer time scales in current CGCMs (Kajtar et al 2018; McGregor et al. 2018; Li et al. 2020).

Finally, the absence of AO SST variability weakens the simultaneous inverse relationship between ISM and ENSO despite ENSO is stronger during boreal summer and persists longer. This result is opposite to the one found in similar IO decoupling experiments in which ENSO is also stronger and more persistent (Terray et al. 2021). The origin of this paradox lies mainly in the modulation of the Walker circulation when SST variability is removed in one of the two oceanic basins, especially during boreal summer of the ENSO decaying year (see Fig. 14). The upper-level divergent wind flows mainly from the PO to the AO, resulting in rainfall suppression in the AO, but in a weaker forcing on ISMR in the AO decoupled experiments (Fig. 14c). On the other hand, both the stronger ENSO amplitude and the enhanced upper-level convergence towards the Indian domain act in concert and result in a much stronger inverse ENSO-ISMR relationship in similar IO decoupled experiments (Terray et al. 2021).

In conclusion, while the AO “direct” effect on ISMR is insignificant in our coupled model, we highlight that the AO “direct“ effect on ENSO is significant in many aspects including the ENSO triggering mechanism and AO capacitor effect, which have also a significant “indirect” impact on ISMR mediated by the ENSO teleconnections. We hope that these encouraging results will promote the interest of performing similar IO, PO and AO decoupled experiments with other coupled models in order to verify if the insignificant “direct” effect of AO SSTs on ISMR found here is model dependent or not.

Acknowledgments: Pascal Terray is funded by Institut de Recherche pour le Développement (IRD, France). The Centre for Climate Change Research (CCCR) at the Indian Institute of Tropical Meteorology (IITM) is fully funded by the Ministry of Earth Sciences, Government of India. The SINTEX-F2 simulations are performed using HPC resources in France from GENCI-IDRIS (Grant 0106895 over the last 5 years). Analysis was done with the STATPACK and NCSTAT softwares available at https://terray.locean-ipsl.upmc.fr/software.html. Simulation data will be made available on reasonable request.

References

Barimalala R, Bracco A, Kucharski F (2012) The representation of the South Tropical Atlantic teleconnection to the Indian Ocean in the AR4 coupled models. Clim Dyn 38:1147-1166 doi:10.1007/s00382-011-1082-5

Bi D, Wang G, Cai W, Santoso A, Sullivan A, Ng B, Jia F (2022). Improved simulation of ENSO variability through feedback from the equatorial Atlantic in a pacemaker experiment. Geophys Res Lett, *49*, e2021GL096887. https://doi. org/10.1029/2021GL096887

Boschat G, Terray P, Masson S (2012) Robustness of SST teleconnections and precursory patterns associated with the Indian summer monsoon. Clim Dyn 38:2143-2165 doi: 10.1007/s00382-011-1100-7

Boschat G, Terray P, Masson S (2013) Extratropical forcing of ENSO. Geophys Res Lett 40:1-7 doi:10.1002/grl.50229

Cabos W, de la Vara A, Koseki S (2019) Tropical Atlantic variability: observations and modeling. Atmosphere 10:502 https://doi.org/ 10.3390/atmos10090502

Cai W, Wu L, Lengaigne M, Li T, McGregor S, Kug J-S, Yu J-Y, Stuecker MF, Santoso A, Li X, Ham Y-G, Chikamoto Y, Ng B, McPhaden MJ, Du Y, Dommenget D, Jia F, Kajtar JB, Keenlyside N, Lin X, Luo JJ, Martin-Rey M, Ruprich-Robert Y, Wang G, Xie SP, Yang Y, Kang SM, Choi J-Y, Gan B, Kim G-I, Kim C-E, Kim S, Kim J-H, Chang P (2019) Pantropical climate interactions. Science 363:6430 https://doi.org/10.1126/science.aav42

Carton JL, Giese BS (2008) A Reanalysis of Ocean Climate Using Simple Ocean Data Assimilation (SODA). Mon Weather Rev 136:2999-3017

Chakraborty A (2018) Preceding winter La Niña reduces Indian summer monsoon rainfall. Environmental Research Letters, 13(5):p.054030

Chakraborty A, Singhai P (2021) Asymmetric response of the Indian summer monsoon to positive and negative phases of major tropical climate patterns. Sci Rep 11:22561

Chang P, Fang Y, Saravanan R et al (2006) The cause of the fragile relationship between the Pacific El Niño and the Atlantic Niño. Nature 443:324-328 doi: https://doi.org/10.1038/nature05053

Cherchi A, Terray P, Ratna SB, Sankar S, Sooraj KP, Behera T (2021) Indian Ocean Dipole influence on Indian summer monsoon and ENSO: a review. Chapter 8 in *Indian summer monsoon variability: El Nino teleconnections and beyond*, Chowdary JS, Parekh, A, Gnanaseelan C (eds). Elsevier, ISBN: 978-0-12-822402-1. Chapter 8:157-182, https://doi.org/10.1016/B978-0-12-822402-1.00011-9

Chiang JCH, Sobel AH (2002) Tropical tropospheric temperature variations caused by ENSO and their influence on the remote tropical climate. J Clim 15:2616-2631 https://doi.org/10.1175/1520- 0442(2002)015%3c2616:TTTVCB%3e2.0.CO;2

Chiang JCH, Vimont DJ (2004) Analogous meridional modes of atmosphere-ocean variability in the tropical Pacifc and tropical Atlantic. J Clim 17(21):4143-4158

Chowdary JS, Parekh, A, Gnanaseelan C (2021) Indian summer monsoon variability: El Nino teleconnections and beyond. Chowdary JS, Parekh, A, Gnanaseelan C (eds). Elsevier, ISBN: 978-0-12-822402-1, 494 pp

Cretat J, Terray P, Masson S, Sooraj KP, Roxy MK (2017) Indian Ocean and Indian Summer Monsoon: relationships without ENSO in ocean-atmosphere coupled simulations. Clim Dyn 49:1429-1448 doi:10.1007/s00382-016-3387-x

Cretat J, Terray P, Masson S, Sooraj KP (2018) Intrinsic precursors and timescale of the tropical Indian Ocean Dipole: insights from partially decoupled experiment. Clim Dyn 51:1311-1352 https://doi.org/10.1007/s00382-017-3956-7

Dee DP et al (2011) The ERA-Interim reanalysis: Configuration and performance of the data assimilation system. Q J Roy Meteorol Soc 137:553-597

Ding H, Keenlyside NS, Latif M (2012) Impact of the equatorial Atlantic on the El Niño Southern Oscillation. Clim Dyn 38:1965-1972 https://doi.org/10.1007/s00382- 011-1097-y.

Ebisuzaki W (1997) A method to estimate the statistical significance of a correlation when the data are serially correlated. J Clim 10:2147-2153

Enfield D, Mayer D (1997) Tropical Atlantic sea surface temperature variability and its relation to El Nino-Southern Oscillation. J Geophys Res 102(C1):929-945 doi:10.1029/96JC03296

Fischer AS, Terray P, Guilyardi E, Gualdi S, Delecluse P (2005) Two independent triggers for the Indian Ocean dipole/ zonal mode in a coupled GCM. J Clim 18:3428-3449 https://doi.org/10.1175/JCLI3478.1

Frauen C, Dommenget D (2012) Influences of the tropical Indian and Atlantic Oceans on the predictability of ENSO. Geophys Res Lett 39:L02706

Gadgil S, Gadgil S (2006) The Indian monsoon, GDP and agriculture. Econ Political Wkly 41:4887-4895

Garcia-Serrano J, Cassou C, Douville H et al (2017) Revisiting the ENSO teleconnection to the Tropical North Atlantic. J Clim 30:6945-6957 https://doi.org/10.1175/JCLI-D-16-0641.1

Gill AE (1980) Some simple solutions for heat-induced tropical circulation. Q J R Meteorol Soc 106:447-462

Ham YG, Kug JS, Park JY, Jin FF (2013a) Sea surface temperature in the north tropical Atlantic as a trigger for El Niño/Southern Oscillation events. Nature Geoscience *6*(2):112

Ham YG, Kug JS, Park JY (2013b) Two distinct roles of Atlantic SSTs in ENSO variability: North Tropical Atlantic SST and Atlantic Niño. Geophys Res Lett 40(15):4012-4017

Huffman GJ, Adler RF, Morrissey MM, Bolvin DT, Curtis S, Joyce R, McGavock B, Susskind J (2001) Global precipitation at one-degree daily resolution from multisatellite observations. J Hydrometeor 2:36-50

Izumo T, Vialard J, Lengaigne M et al (2010) Influence of the state of the Indian Ocean dipole on the following years El Niño. Nat Geosci 3:168-172

Jiang L, Li T (2019) Relative roles of El Niño-induced extratropical and tropical forcing in generating tropical North Atlantic (TNA) SST anomaly. Clim Dyn 53:3791-3804 https://doi.org/10.1007/s00382-019-04748-7

Jiang L, Li T (2021) Impacts of Tropical North Atlantic and Equatorial Atlantic SST Anomalies on ENSO. J Clim 34:5635-5655 https://doi.org/10.1175/JCLI-D-20-0835.1

Kajtar JB, Santoso A, England MH, Cai W (2017) Tropical climate variability: interactions across the Pacific, Indian, and Atlantic Oceans. Clim Dyn 48:2173-2190 https://doi.org/10.1007/ s00382-016-3199-z

Kajtar JB, Santoso A, McGregor S et al (2018) Model under-representation of decadal Pacific trade wind trends and its link to tropical Atlantic bias. Clim Dyn 50:1471-1484 https://doi.org/10.1007/s00382-017-3699-5

Kumar KK, Rajagopalan B, Cane MA (1999) On the weakening relationship between the Indian monsoon and ENSO. Science 284:2156-2159

Kucharski F, Bracco A, Yoo J, Molteni F (2007) Low- frequency variability of the Indian monsoon-ENSO relationship and the tropical Atlantic: The weakening of the 1980s and 1990s. J Clim 20:4255-4266

Kucharski F, Bracco A, Yoo J, Tompkins A, Feudale L, Ruti P, Dell'Aquila A (2009) A Gill-Matsuno-type mechanism explains the tropical Atlantic influence on African and Indian monsoon rainfall. Q J R Meteorol Soc 135(640):569-579 https://doi.org/10.1002/qj.406

Kucharski F, Kang I-S, Farneti R, Feudale L (2011) Tropical Pacific response to 20th century Atlantic warming. Geophys Res Lett 38:L03702

Li X, Xie, S-P, Gille ST and Yoo C (2016) Atlantic-induced pan-tropical climate change over the past three decades. Nat. Clim. Change 6:275-280

Li C, Dommenget D, McGregor S (2020) Trans-basin Atlantic-Pacific connections further weakened by common model Pacific mean SST biases. Nat Comm 11:5677 https://doi.org/10.1038/s41467-020-19338-z

Lübbecke JF, Rodríguez-Fonseca B, Richter I, Martín-Rey M, Losada T, Polo I, Keenlyside NS (2018) Equatorial Atlantic variability: Modes, mechanisms, and global teleconnections. Wiley Interdiscip Rev Clim Change 9(4):e527 https://doi.org/10.1002/wcc.527

Ma J, Xie SP, Xu H (2017) Contributions of the North Pacific Meridional Mode to Ensemble Spread of ENSO prediction. J Clim 30:9167-9181 https://doi.org/10.1175/JCLI-D-17-0182.1

Madec G (2008) NEMO ocean engine. Note du Pole de modelisation, Institut Pierre-Simon Laplace (IPSL) No 27. ISSN No 1288-1619

Masson S, Terray P, Madec G, Luo JJ, Yamagata T, Takahashi K (2012) Impact of intra-daily SST variability on ENSO characteristics in a coupled model. Clim Dyn 39:681-707

McGregor S et al (2014) Recent Walker circulation strengthening and Pacific cooling amplified by Atlantic warming. Nature Clim Change 4:888-892

McGregor S et al (2018) Model tropical Atlantic biases underpin diminished Pacific decadal variability. Nat Clim Change 8:493-498

Meehl GA, Arblaster JM, Loschnigg J (2003) Coupled ocean-atmosphere dynamical processes in the tropical Indian and Pacific oceans and the TBO. J Clim 16:2138-2158 doi: 10.1175/2767.1

Ohba M, Ueda H (2007) An impact of SST anomalies in the Indian Ocean in acceleration of the El Nino to La Nina transition. J Meteor Soc Jpn 85:335-348

Ogata T, Doi T, Morioka Y et al (2019) Mid-latitude source of the ENSO-spread in SINTEX-F ensemble predictions. Clim Dyn 52:2613-2630 https://doi.org/10.1007/s00382-018-4280-6

Pai DS, Sridhar L, Badwaik MR, Rajeevan M (2015) Analysis of the daily rainfall events over India using a new long period (1901-2010) high resolution (0.25 × 0.25) gridded rainfall data set. Clim Dyn 45:755-776

Pottapinjara V, Girishkumar MS, Ravichandran M, Murtugudde R (2014) Influence of the Atlantic zonal mode on monsoon depressions in the Bay of Bengal during boreal summer. J Geophys Res Atmos 119(11):6456-6469 https://doi.org/10.1002/ 2014JD021494

Pottapinjara V, Girishkumar MS, Sivareddy S, Ravichandran M, Murtugudde R (2016) Relation between the upper ocean heat content in the equatorial Atlantic during boreal spring and the Indian monsoon rainfall during June-Spetember. Int J Climatol 36:2469-2480 https://doi.org/10.1002/joc.4506

Rao SA et al (2019) Monsoon mission: a targeted activity to improve monsoon prediction across scales. Bull Am Meteorol Soc 100(12):2509-2532 https://doi.org/10.1175/ BAMS-D-17-0330.1

Rayner NA, Parker DE, Horton EB, Folland CK, Alexander LV, Rowell DP, Kent EC, Kaplan A (2003) Global analyses of sea surface temperature, sea ice, and night marine air temperature since the late nineteenth century. J Geophys Res 108(D14):4407 https://doi.org/10.1029/2002JD002670

Reynolds RW, Smith TM, Liu C, Chelton DB, Casey KS, Schlax MG (2007) Daily high-resolution-blended analyses for sea surface temperature. J Clim 20:5473-5496 https://doi.org/10.1175/2007JCLI1824.1

Richter I, Xie S-P, Behera S, Doi T, Masumoto, Y (2014) Equatorial Atlantic variability and its relation to mean state biases in CMIP5. Clim Dyn 42:171 https://doi.org/doi.10.1007/s00382-012-1624-5

Richter I, Tokinaga H, Kosaka Y, Doi T, Kataoka T (2021) Revisiting the Tropical Atlantic Influence on El Niño-Southern Oscillation. J clim 34:8533-8548 doi:10.1175/JCLI-D-21-0088.1

Richter I, Tokinaga H (2021) The Atlantic zonal mode: Dynamics, thermodynamics, and teleconnections. In: Behera SK (eds) Tropical and extra-tropical air-sea interactions. Elsevier. ISBN: 9780128181560

Rodriguez-Fonseca B, Polo I, Garcia-Serrano J, Losada T, Mohino E, Mechoso CR, Kucharski F (2009) Are Atlantic Ninos enhancing Pacific ENSO events in recent decades? Geophys Res Lett 36:L20705

Roeckner E, Baüml G, Bonaventura L, Brokopf R, Esch M, Girogetta M, Hagemann S, Kirchner I, Kornblueh L, Manzini E, Rhodin A, Schlese U, Schulzweida U, Tompkins A (2003) The atmospheric general circulation model ECHAM 5. Part I, MPI Report, vol 349. Hamburg, Max-Planck-Institut für Meteorologie

Sabeerali C, Ajayamohan R, Bangalath HK, Chen N (2019) Atlantic zonal mode: an emerging source of indian summer monsoon variability in a warming world. Geophys Res Lett 46(8):4460-4467 https://doi.org/10.1029/2019GL082379

Santoso A, England MH, Cai W (2012) Impact of Indo-Pacic feedback interactions on ENSO dynamics diagnosed using ensemble climate simulations. J Clim 25:7743-7763

Srivastava G, Chakraborty A, Nanjundiah RS (2019) Multidecadal see-saw of the impact of ENSO on Indian and West African summer monsoon rainfall. Clim Dyn 52**:**6633-6649

Stuecker MF, Timmermann A, Jin FF, Chikamoto Y, Zhang W, Wittenberg AT, Widiasih E, Zhao S (2017) Revisiting ENSO/Indian Ocean Dipole phase relationships. Geophys Res Lett 44:2481-2492 doi:10.1002/2016GL072308

Terray P, Delecluse P, Labattu S, Terray L (2003) Sea Surface Temperature Associations with the Late Indian Summer Monsoon. Clim Dyn 21:593-618 doi:10.1007/s00382-003-0354-0

Terray P, Dominiak S, Delecluse P (2005) Role of the southern Indian Ocean in the transitions of the monsoon-ENSO system during recent decades. Clim Dyn 24:169-195 doi:10.1007/s00382- 0040480-3

Terray P, Masson S, Prodhomme C, Roxy MK, Sooraj KP (2016) Impacts of Indian and Atlantic oceans on ENSO in a comprehensive modeling framework. Clim Dyn 46:2507-2533 https:// doi.org/10.1007/s00382-015-2715-x

Terray P, Sooraj KP, Masson S et al (2021) Anatomy of the Indian Summer Monsoon and ENSO relationships in state-of-the-art CGCMs: role of the tropical Indian Ocean. Clim Dyn 56**:**329-356 https://doi.org/10.1007/s00382-020-05484-z

Timmermann R, Goosse H, Madec G, Fichefet T, Ethe C, Duliere V (2005) On the representation of high latitude processes in the ORCA-LIM global coupled sea ice-ocean model. Ocean Model 8:175-201

Tokinaga H, Richter I, Kosaka Y (2019) ENSO influence on the Atlantic Niño, revisited: Multi-year versus single-year ENSO events. J Clim 32:4585-4600 doi: https://doi.org/10.1175/ JCLI-D-18-0683.1.

Valcke S (2006) OASIS3 user guide (prism_2-5). CERFACS technical report TR/CMGC/06/73, PRISM report no. 3, Toulouse, pp 64

Vimont DJ, Wallace JM, Battisti DS (2003) The seasonal footprinting mechanism in the Pacific: Implications for ENSO. J Clim 16(16):2668-2675

Vittal H, Villarini G, Zhang W (2020) Early prediction of the Indian summer monsoon rainfall by the Atlantic Meridional Mode. Clim Dyn 54:2337-2346 https://doi.org/10.1007/s00382-019-05117-0

Voldoire A, Exarchou E, Sanchez-Gomez E, Demissie T, Deppenmeier AL, Frauen C, Goubanova K, Hazeleger W, Keenlyside N, Koseki S et al (2019) Role of wind stress in driving SST biases in the tropical Atlantic. Clim Dyn 53(5–6):3481–3504

Wang L, Yu J-Y, Paek H (2017) Enhanced biennial variability in the Pacific due to Atlantic capacitor effect . Nat Comm 8:14887 doi:10.1038/ncomms14887

Webster PJ, Magana V, Palmer TN, Shukla J, Tomas RA, Yanai M, Yasunari T (1998) Monsoons: processes, predictability and the prospects for prediction. J Geophys Res 103:14451-14510 doi:10.1029/97JC02719

Xie SP, Hu K, Hafner J et al (2009) Indian Ocean capacitor effect on Indo-Western pacific climate during the summer following El Niño. J Clim 22:730-747 https://doi.org/10.1175/2008JCLI2544.1

Xie SP, Kosaka Y, Du Y et al (2016) Indo-western Pacific Ocean capacitor and coherent climate anomalies in post-ENSO summer: a review. Adv Atmos Sci 33:411-432 https://doi.org/10.1007/ s00376-015-5192-6

Yang JL, Liu QY, Xie S-P, et al (2007) Impact of the Indian Ocean SST basin mode on the Asian summer monsoon. Geophys Res Lett 34:L02708 doi:10.1029/2006GL028571

Yang X, Huang P (2021) Restored relationship between ENSO and Indian summer monsoon rainfall around 1999/2000. The Innovation 2(2):100102

Zhang L, Han W (2021) Indian Ocean Dipole leads to Atlantic Niño. Nat Comm 12:5952 https://doi.org/10.1038/s41467-021-26223-w

Zhang Y, Zhou W, Li T (2021a) Impact of the Indian Ocean Dipole on Evolution of the Subsequent ENSO: Relative Roles of Dynamic and Thermodynamic Processes. J Clim 34: 3591-3607

Zhang W, Jiang F, Stuecker MF, Jin F-F, Timermann A (2021b) Spurious North Tropical Atlantic precursors to El Niño. Nat Comm 12:3096 https://doi.org/10.1038/s41467-021-23411-6

Figure captions

Figure 1: **a)** SST annual means difference (unit: °C) between CTRL and ERAi; **b)** Z20 annual means difference (unit: m) between CTRL and SODA; **c)** Rainfall annual means difference (unit: mm/day) between CTRL and GPCP; **d)** SST annual means difference (unit: °C) between FTAC-obs and CTRL; **e)** Z20 annual means difference (unit: m) between FTAC-obs and CTRL; **f)** Rainfall annual means difference (unit: mm/day) FTAC-obs and CTRL. The nudging domain for FTPC and FTPC-obs (FTAC and FTAC-obs) is shown in blue (purple) in panel a. See Section 2 and Table 1 for more details.

Figure 2: Empirical Orthogonal Function (EOF) 1st and 2nd modes for detrended SST anomalies with monthly means removed obtained from ERAi and CTRL. **a)** and **b)** EOF1 and EOF2 from ERAi SST detrended anomalies (1979-2015 period), respectively. **c)** and **d)** EOF1 and EOF2 from CTRL SST detrended anomalies (11-210 period), respectively. The number in parentheses for each panel gives the % of SST variance described by the EOF mode.

Figure 3: a) Monthly means of ATL3 SST (unit: °C) index from ERAi (blue) and CTRL (orange); **b)** Monthly standard deviations of ATL3 SST (unit: °C) from ERAi (blue) and CTRL (orange).

Figure 4: a) Quarterly SST time series (from ERAi) during the preceding (e.g. year -1) and simultaneous (e.g. year 0) ISM years, regressed against the ISMR index (e.g. JJAS ISM rainfall from GPCP). Unit for the SST regression coefficient is °C by mm/day. **b)** Same as **a)**, but for regression using quarterly rainfall and 850-hPa wind time series. Units for the rainfall and 850-hPa wind regression coefficients are mm/day by mm/day and m s^{-1} by mm/day, respectively. **c),** Same as **a)**, but for quarterly 200-hPa velocity potential time series. Unit for the 200-hPa velocity potential regression coefficient is 10^5 m^2 s^{-1} by mm/day. Regression coefficients reaching the 90% significance level according to a phase-scrambling bootstrap test (Ebisuzaki 1997) with 999 samples are contoured (SST or 200-hPa velocity potential) or shown (rainfall and 850-hPa wind). Quarterly time series refer to to the seasons February-May, June-September, October-January and so on.

Figure 5: a) Quarterly SST time series during year 0 regressed against the ISMR index (e.g. JJAS ISM rainfall) in CTRL. Unit for the SST regression coefficient is °C by mm/day. **b)** Same as **a)**, but for regression using quarterly rainfall and 850-hPa wind time series in CTRL. Units for the rainfall and 850-hPa wind regression coefficients are mm/day by mm/day and m s^{-1} by mm/day, respectively. **c),** Same as **a)**, but for quarterly 200-hPa velocity potential time series in CTRL. Unit for the 200-hPa velocity potential regression coefficient is 10^5 m^2 s^{-1} by

mm/day. Regression coefficients reaching the 90% significance level according to a phase-scrambling bootstrap test (Ebisuzaki 1997) are contoured (SST or 200-hPa velocity potential) or shown (rainfall and 850-hPa wind).

Figure 6: Empirical Orthogonal Function (EOF) 1st and 2nd modes for 12-monthly anomaly of detrended SST obtained from FTPC and FTPC-obs experiments. **a)** and **b)** EOF1 and EOF2 from FTPC SST detrended anomalies (11-110 period), respectively. **c)** and **d)** EOF1 and EOF2 from FTPC-obs SST detrended anomalies (11-50 period), respectively. The number in parentheses for each panel gives the % of SST variance described by the EOF mode.

Figure 7: **a)** Quarterly SST time series during year 0 regressed against the ISMR index (e.g. JJAS ISM rainfall) in FTPC-obs. Unit for the SST regression coefficient is °C by mm/day. **b)** Same as **a)**, but for quarterly 200-hPa velocity potential time series in FTPC-obs. Unit for the 200-hPa velocity potential regression coefficient is 10^5 m^2 s^{-1} by mm/day. Regression coefficients reaching the 90% significance level according to a phase-scrambling bootstrap test (Ebisuzaki 1997) are contoured.

Figure 8: Monthly standard deviations of Nino34 SST (unit:°C) from ERAi (blue), CTRL (orange), FTAC (green) and FTAC-obs (red).

Figure 9: **a)** Quarterly rainfall and 850-hPa wind time series during boreal winter and spring regressed against the Nino34 index during the following boreal winter (e.g. ONDJ Nino34 SST) in FTAC-obs. **b)** Same as **a)**, but in FTAC. **c)** Quarterly SST time series during boreal winter and spring regressed against the Nino34 index during the following boreal winter in FTAC-obs. **d)** Same as **c)**, but in FTAC. Unit for the SST regression coefficient is °C by °C. Units for the rainfall and 850-hPa wind regression coefficients are mm/day by °C and m s^{-1} by °C, respectively. Regression coefficients reaching the 90% significance level according to a phase-scrambling bootstrap test (Ebisuzaki 1997) are contoured (SST or 200-hPa velocity potential) or shown (rainfall and 850-hPa wind).

Figure 10: **a)** 850-hPa zonal wind boreal spring means differences (unit: m s^{-1}) between FTAC-obs and CTRL; **b)** 200-hPa zonal wind boreal spring means differences (unit: m s^{-1}) between FTAC-obs and CTRL; **c)** 850-hPa velocity potential boreal spring means differences (unit: 10^6 m^2 s^{-1}) between FTAC-obs and CTRL; **d)** 200-hPa velocity potential boreal spring means differences (unit: 10^6 m^2 s^{-1}) between FTAC-obs and CTRL; **e)** 850-hPa stream function boreal spring means differences (unit: 10^6 m^2 s^{-1}) between FTAC-obs and CTRL; **f)**

200-hPa stream function boreal spring means differences (unit: 10^6 m^2 s^{-1}) between FTAC-obs and CTRL.

Figure 11: **a)** Rainfall boreal spring standard deviation differences (unit: mm/day) between FTAC-obs and CTRL. **b)** Same as **a)**, but for FTAC and CTRL. **c)** 850-hPa zonal wind boreal spring standard deviation differences (unit: m s^{-1}) between FTAC-obs and CTRL. **d)** Same as **c)**, but for FTAC and CTRL.

Figure 12: **a)** Boreal spring SST time series regressed against the Nino34 index during the preceding boreal winter (e.g. ONDJ Nino34 SST) in FTAC-obs; **b)** Boreal summer SST time series regressed against the Nino34 index during the preceding boreal winter in FTAC-obs; **c)** Boreal winter SST time series regressed against the Nino34 index during the preceding boreal winter in FTAC-obs. Unit for the SST regression coefficient is °C by °C. Regression coefficients reaching the 90% significance level according to a phase-scrambling bootstrap test (Ebisuzaki 1997) are contoured.

Figure 13: **a)** Monthly means of ISMR (unit: mm/day) from GPCP (blue), CTRL (orange), FTAC (green) and FTAC-obs (red); **b)** Monthly standard deviations of ISMR (unit: mm/day) from GPCP (blue), CTRL (orange), FTAC (green) and FTAC-obs (red); **c)** Lead-lag correlations between ISMR and quarterly Nino3.4 SSTs starting from the beginning of the previous year (e.g. year - 1) to the end of the following year of the monsoon (e.g. year +1) in observations (blue), CTRL (orange), FTAC (green) and FTAC-obs (red). X-axis indicates the lag (in 4 months interval) for a 36 months period starting one year before the developing year of ISMR (e.g. year 0) and Y-axis is the amplitude of the correlation. Thus, the coefficients corresponding to -1, 0, +1 lags refer, respectively, to the correlations between ISMR in year 0 (e.g. JJAS ISM rainfall) and February-May, June-September and October-January Niño-3.4 SSTs, also during year 0, and so on. Circles indicate correlations that are above the 90% significance confidence level according to a phase-scrambling bootstrap test (Ebisuzaki 1997).

Figure 14: **a)** Boreal spring and summer 200-hPa velocity potential time series regressed against the preceding boreal winter Nino34 SST in ERAi. **b)** Same as **a)**, but for CTRL. **c)** Same as **a)**, but for FTAC-obs. Unit for the 200-hPa velocity potential regression coefficient is 10^5 m^2 s^{-1} by mm/day. Regression coefficients reaching the 90% significance level according to a phase-scrambling bootstrap test (Ebisuzaki 1997) are contoured.

Figure S1: **a)** SST seasonal standard deviations (unit: °C) computed from ERAi. **b)** SST seasonal standard deviation differences (unit: °C) computed between CTRL and ERAi.

Figure S2: **a)** Quarterly (residual) SST time series during the preceding (e.g. year -1) and simultaneous (e.g. year 0) ISM years regressed against the ISMR index (e.g. JJAS ISM rainfall) in ERAi and GPCP after the simultaneous linear effect of the Nino34 index has been removed from the SST time series by a linear regression method. Unit for the SST regression coefficient is °C by mm/day. **b)** Same as **a),** but for CTRL**.**

Figure S3: **a)** Quarterly SST time series during years 0 and +1 regressed against the Nino34 index during boreal winter (e.g. ONDJ Nino34 SST) in ERAi. **b)** Same as **a)**, but in CTRL. Unit for the SST regression coefficient is °C by °C. Regression coefficients reaching the 90% significance level according to a phase-scrambling bootstrap test (Ebisuzaki 1997) are contoured.

Figure S4: **a)** Quarterly rainfall and 850-hPa wind time series during years 0 and +1 regressed against the Nino34 index during boreal winter (e.g. ONDJ Nino34 SST) in GPCP and ERAi. **b)** Same as **a)**, but in CTRL. Units for the rainfall and 850-hPa wind regression coefficients are mm/day by °C and m s^{-1} by °C, respectively. Regression coefficients reaching the 90% significance level according to a phase-scrambling bootstrap test (Ebisuzaki 1997) are shown.

Figure S5: **a)** SST standard-deviation differences (unit: °C) between FTAC-obs and CTRL during boreal spring (e.g. FMAM); **b)** SST standard-deviation differences (unit: °C) between FTAC-obs and CTRL during boreal summer (e.g. JJAS); **c)** SST standard-deviation differences (unit: °C) between FTAC-obs and CTRL during boreal winter (e.g. ONDJ). **d)**, **e)** and **f)** Same as **a)**, **b)** and **c),** but for SST standard-deviation differences between FTAC-obs and FTAC.

Figure S6: **a)** SST seasonal mean climatological differences (unit: °C) between FTAC-obs and CTRL; **b)** Rainfall seasonal means differences (unit: mm/day) between FTAC-obs and CTRL; **c)** Z20 seasonal means differences (unit: m) between FTAC-obs and CTRL.

Figure S7: **a)** Correlation coefficients between the Nino34 index during boreal winter (e.g. ONDJ) and boreal summer (e.g. JJAS) rainfall during the following year in ERAi and GPCP. **b)** Same as **a)**, but in CTRL. **c)** Same as **a)**, but in FTAC-obs. Correlation coefficients above the 90% significance confidence level according to a phase-scrambling bootstrap test (Ebisuzaki 1997) are contoured.

Table captions

Table 1: Summary of the numerical experiments with their main characteristics, including length, nudging domain and SST climatology used for the nudging in the AO or PO decoupled experiments. The nudged experiments are the Forced Tropical Pacific Climatology (FTPC), the Forced Tropical Pacific observed Climatology (FTPC-obs), the Forced Tropical Atlantic Climatology (FTAC) and, finally, the Forced Tropical Atlantic observed Climatology (FTAC-obs) runs. See text for more details. For the FTPC and FTPC-obs experiments only ocean grid-points in the PO are included in the correction or smoothing areas and, similarly, for the FTAC and FTAC-obs experiments. The different correction domains are also displayed in Figure 1a. The observed daily SST climatology used in the FTPC-obs and FTAC-obs experiments is derived from the AVHRR only daily Optimum Interpolation SST version 2 (OISSTv2) dataset for the 1982-2010 period (Reynolds et al. 2007).

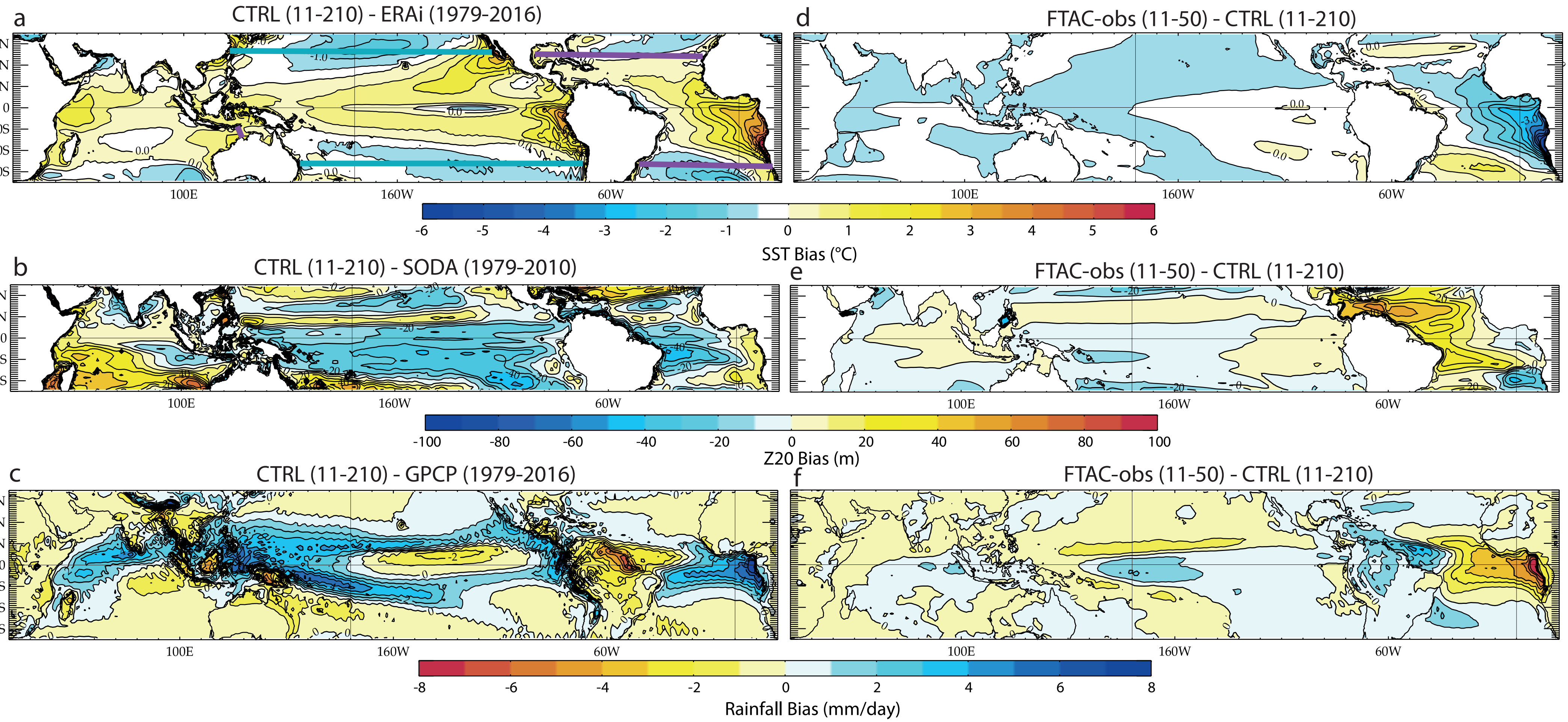

Figure 1: a) SST annual means difference (unit: °C) between CTRL and ERAi; b) Z20 annual means difference (unit: m) between CTRL and SODA; c) Rainfall annual means difference (unit: mm/day) between CTRL and GPCP; d) SST annual means difference (unit: °C) between FTAC-obs and CTRL; e) Z20 annual means difference (unit: m) between FTAC-obs and CTRL; f) Rainfall annual means difference (unit: mm/day) FTAC-obs and CTRL. The nudging domain for FTPC and FTPC-obs (FTAC and FTAC-obs) is shown in blue (purple) in panel a. See Section 2 and Table 1 for more details.

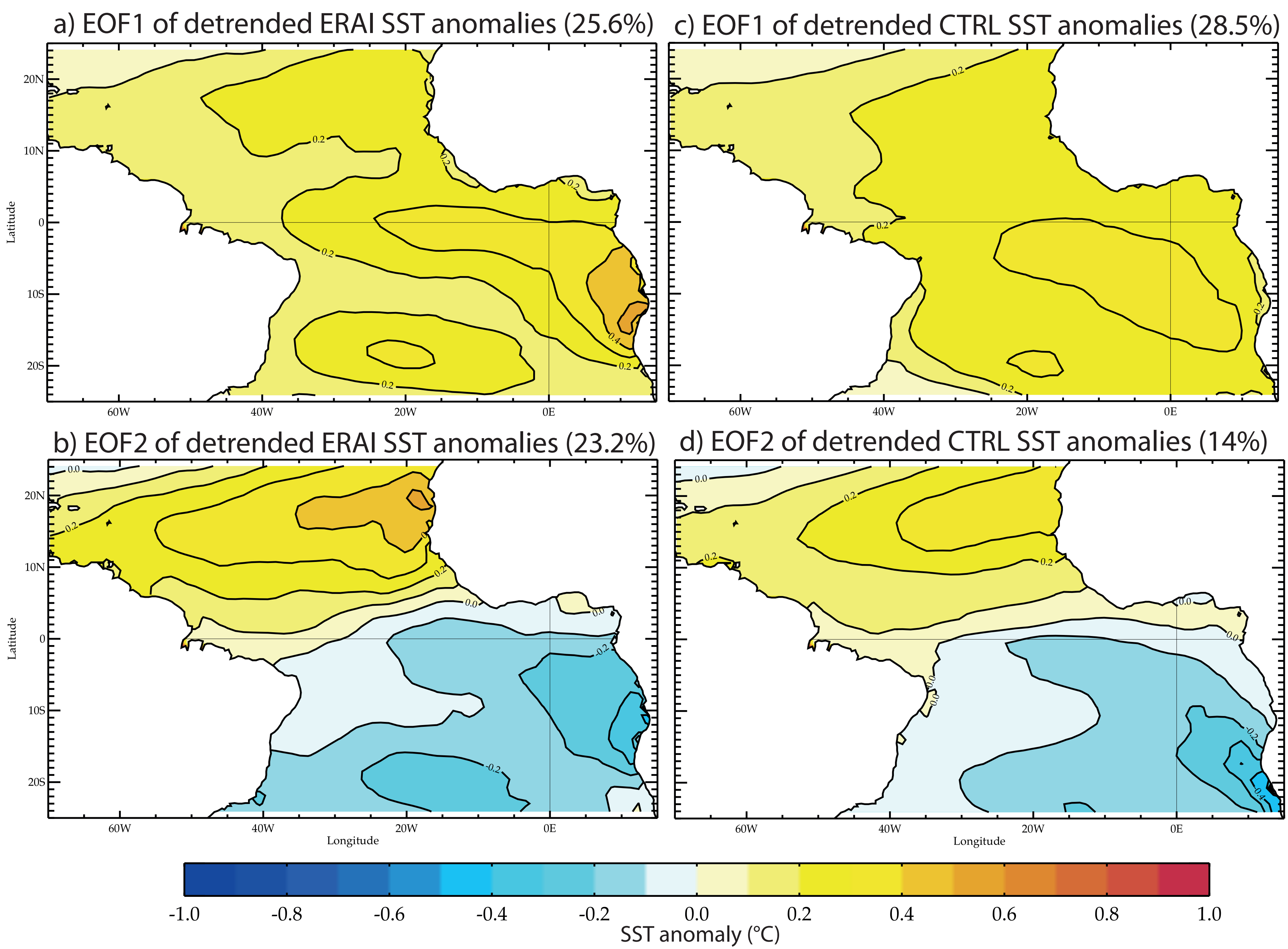

Figure 2: Empirical Orthogonal Function (EOF) 1st and 2nd modes for 12-monthly anomaly of detrended SST obtained from ERAi and CTRL. a) and b) EOF1 and EOF2 from ERAi SST detrended anomalies (1979-2015 period), respectively. c) and d) EOF1 and EOF2 from CTRL SST detrended anomalies (11-210 period), respectively. The number in parentheses for each panel gives the % of SST variance described by the EOF mode.

a) ATL3 SST monthly climatology

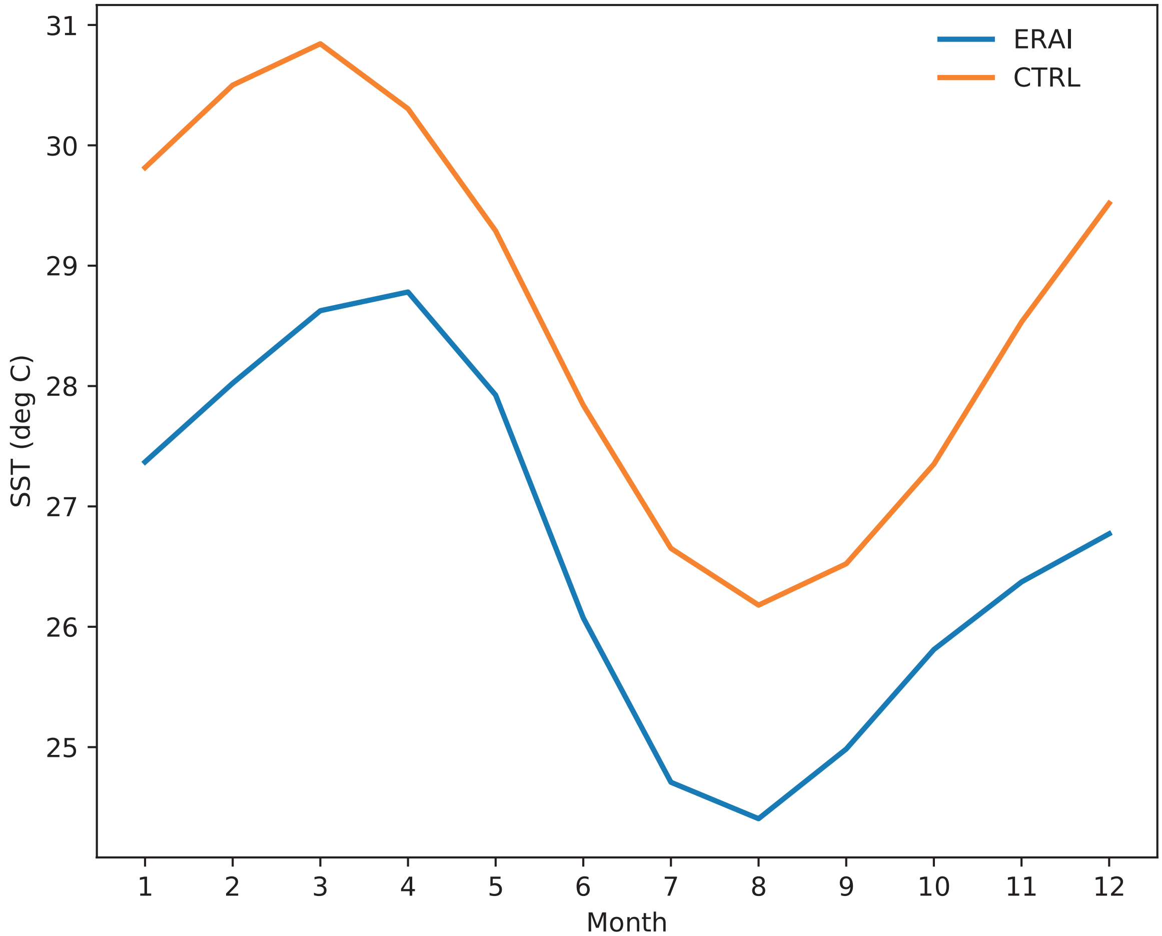

b) ATL3 SST monthly standard deviations

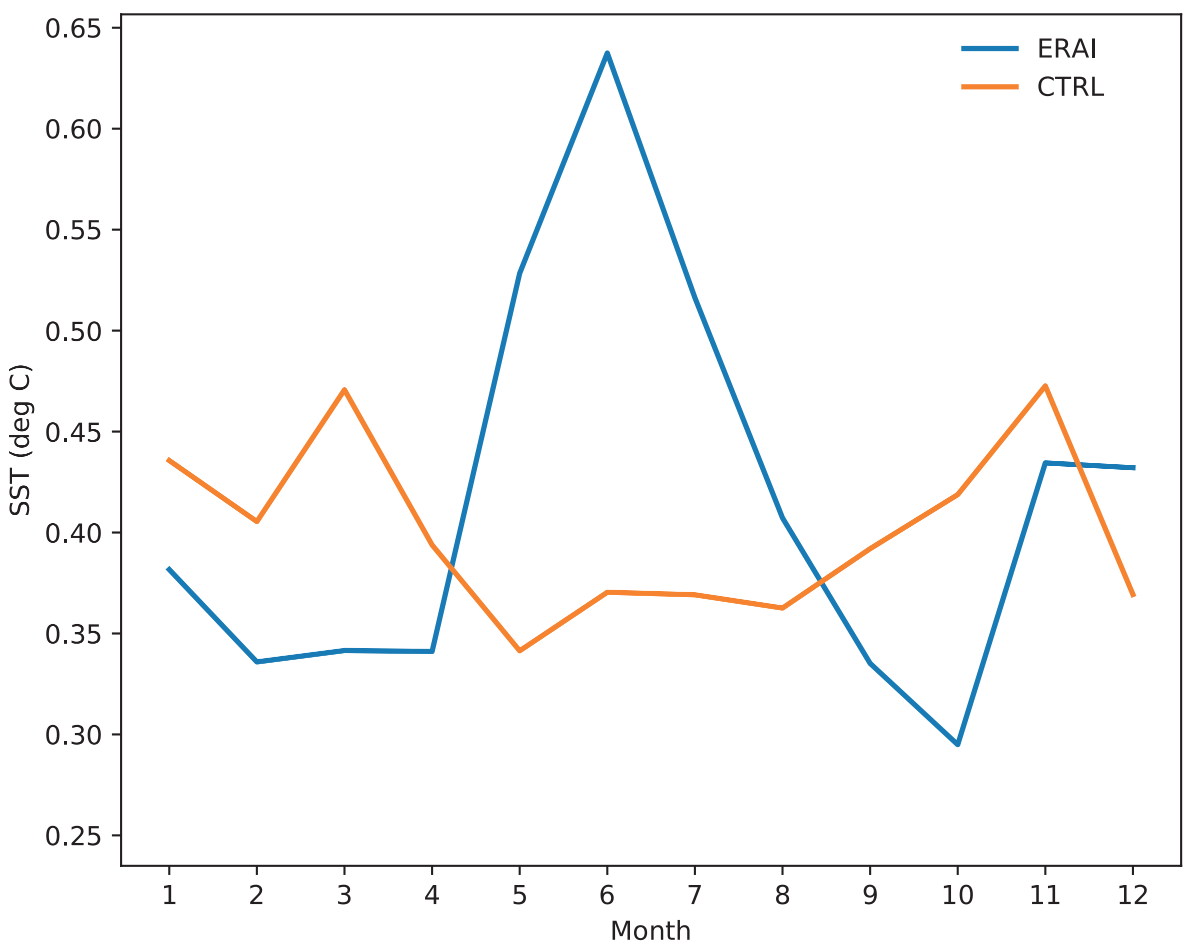

Figure 3: a) Monthly means of ATL3 SST (unit: °C) index from ERAi (blue) and CTRL (orange); b) Monthly standard deviations of ATL3 SST (unit: °C) from ERAi (blue) and CTRL (orange).

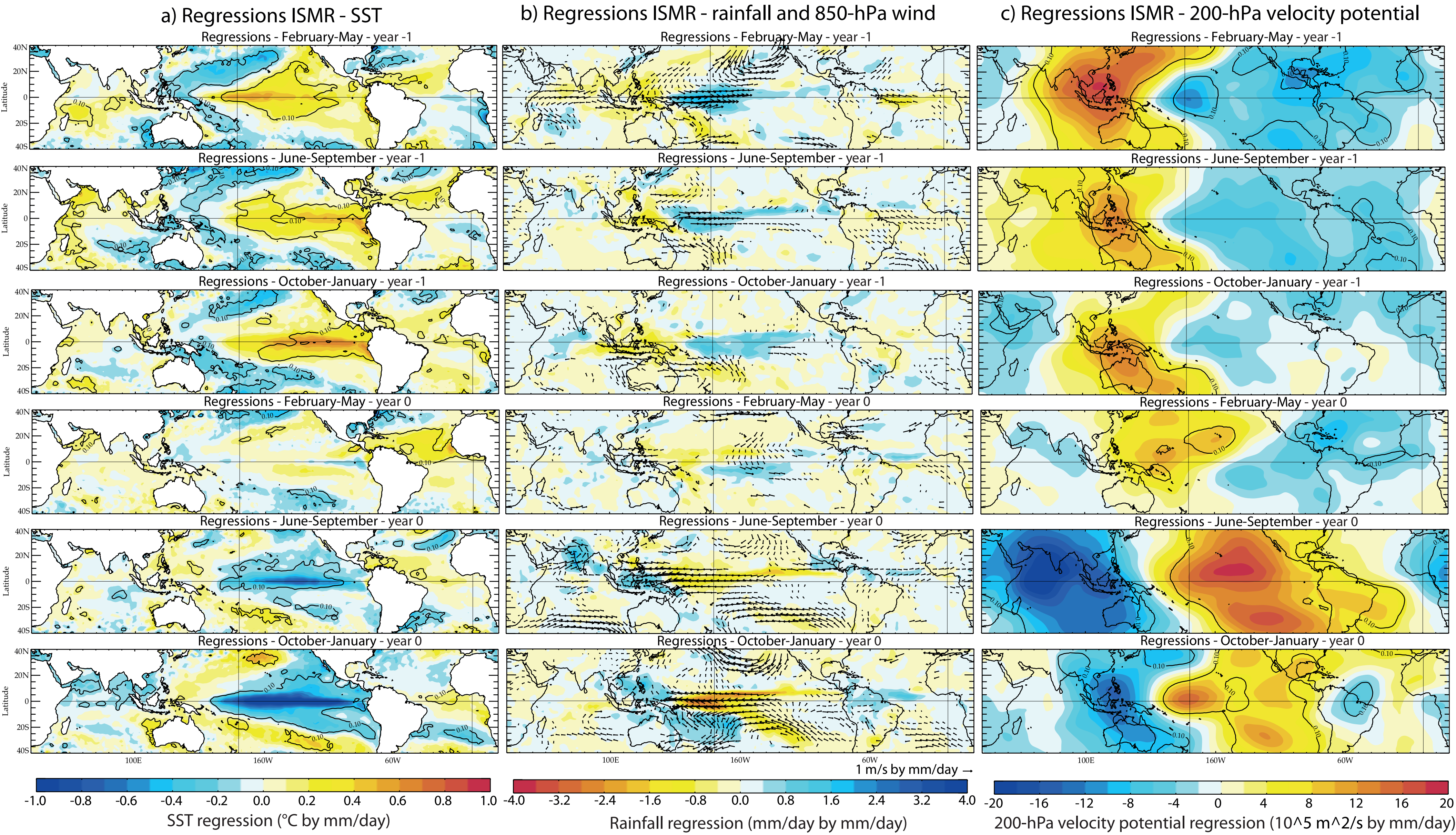

Figure 4: a) Quarterly SST time series (from ERAi) during the preceding (e.g. year -1) and simultaneous (e.g. year 0) ISM years, regressed against the ISMR index (e.g. JJAS ISM rainfall from GPCP). Unit for the SST regression coefficient is °C by mm/day. b) Same as a), but for regression using quarterly rainfall and 850-hPa wind time series. Units for the rainfall and 850-hPa wind regression coefficients are mm/day by mm/day and m s-1 by mm/day, respectively. c), Same as a), but for quarterly 200-hPa velocity potential time series. Unit for the 200-hPa velocity potential regression coefficient is 105 m2 s-1 by mm/day. Regression coefficients reaching the 90% significance level according to a phase-scrambling bootstrap test (Ebisuzaki 1997) with 999 samples are contoured (SST or 200-hPa velocity potential) or shown (rainfall and 850-hPa wind). Quarterly time series refer to to the seasons February-May, June-September, October-January and so on.

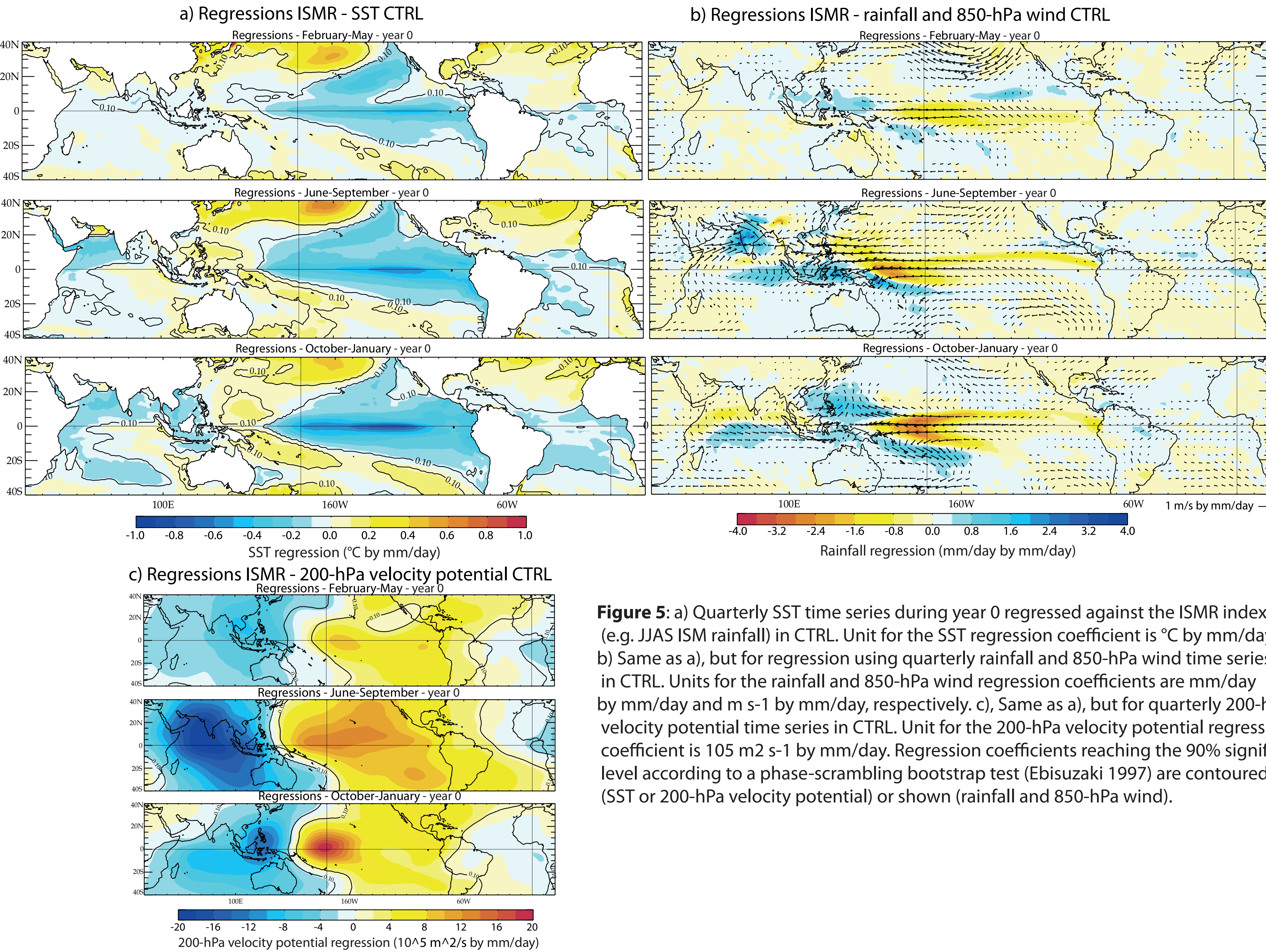

Figure 5: a) Quarterly SST time series during year 0 regressed against the ISMR index (e.g. JJAS ISM rainfall) in CTRL. Unit for the SST regression coefficient is °C by mm/day. b) Same as a), but for regression using quarterly rainfall and 850-hPa wind time series in CTRL. Units for the rainfall and 850-hPa wind regression coefficients are mm/day by mm/day and m s-1 by mm/day, respectively. c), Same as a), but for quarterly 200-hPa velocity potential time series in CTRL. Unit for the 200-hPa velocity potential regression coefficient is 105 m2 s-1 by mm/day. Regression coefficients reaching the 90% significance level according to a phase-scrambling bootstrap test (Ebisuzaki 1997) are contoured (SST or 200-hPa velocity potential) or shown (rainfall and 850-hPa wind).

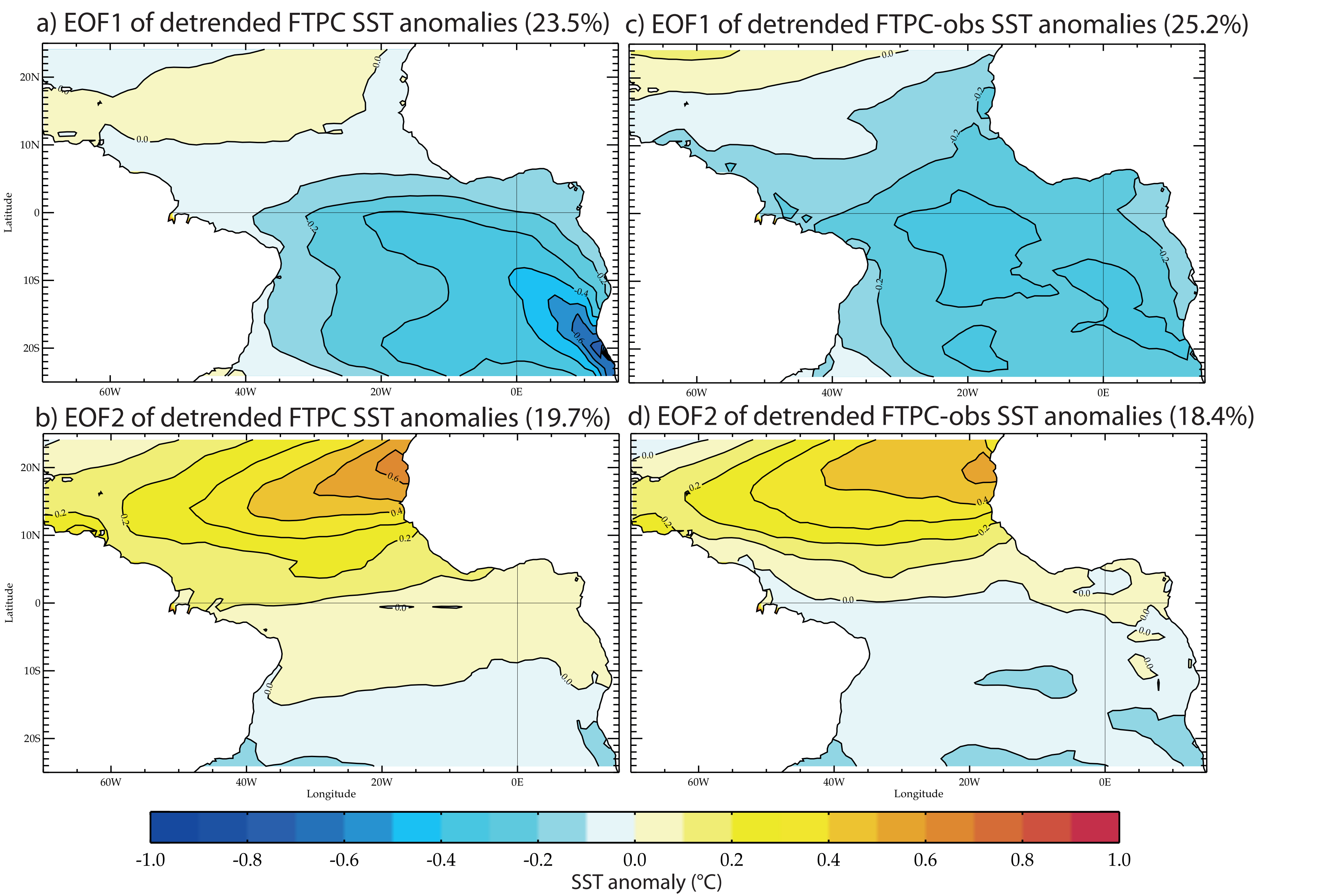

Figure 6: Empirical Orthogonal Function (EOF) 1st and 2nd modes for 12-monthly anomaly of detrended SST obtained from FTPC and FTPC-obs experiments. a) and b) EOF1 and EOF2 from FTPC SST detrended anomalies (11-110 period), respectively. c) and d) EOF1 and EOF2 from FTPC-obs SST detrended anomalies (11-50 period), respectively. The number in parentheses for each panel gives the % of SST variance described by the EOF mode.

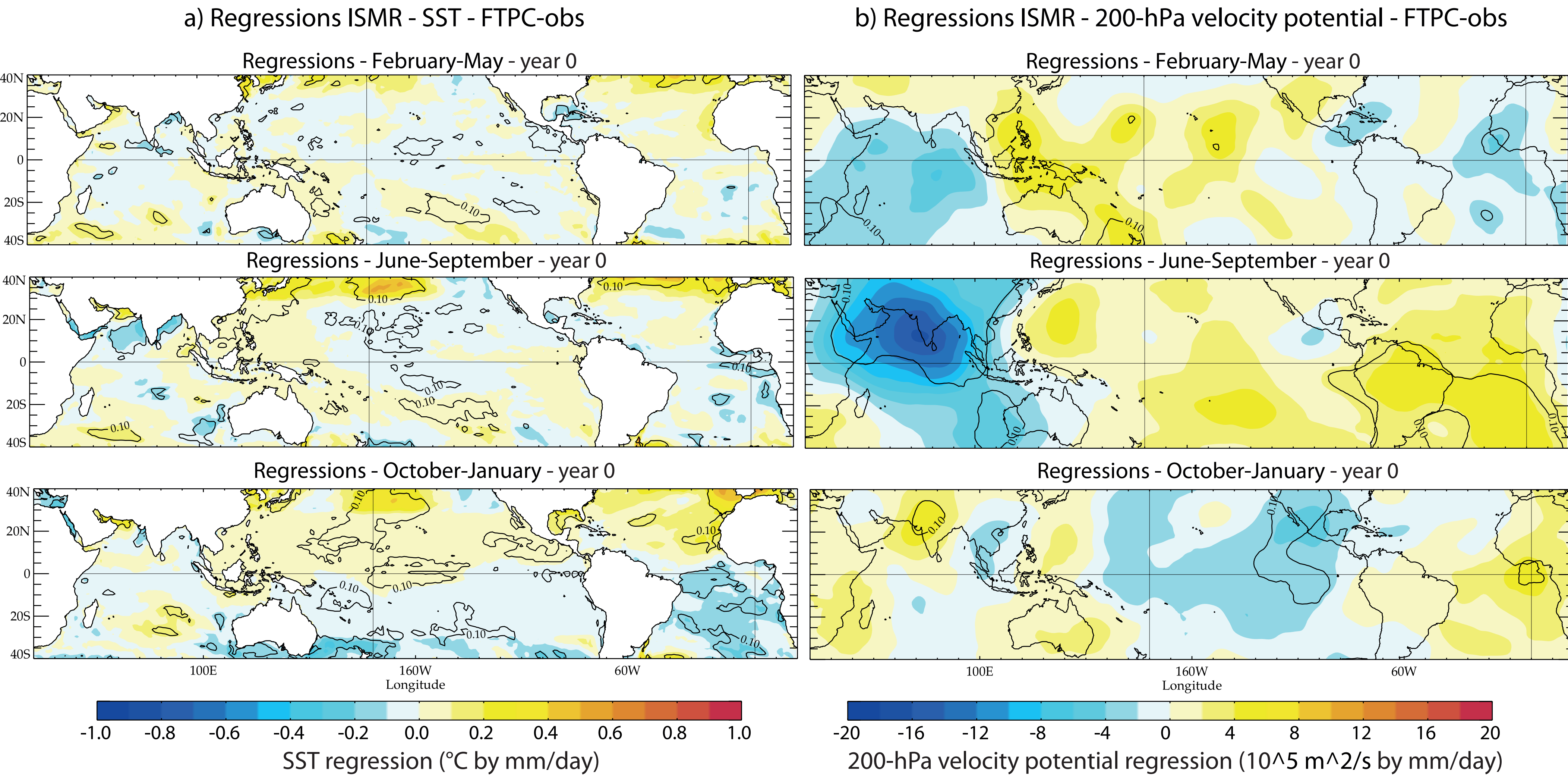

Figure 7: a) Quarterly SST time series during year 0 regressed against the ISMR index (e.g. JJAS ISM rainfall) in FTPC-obs. Unit for the SST regression coefficient is °C by mm/day. b) Same as a), but for quarterly 200-hPa velocity potential time series in FTPC-obs. Unit for the 200-hPa velocity potential regression coefficient is 105 m2 s-1 by mm/day. Regression coefficients reaching the 90% significance level according to a phase-scrambling bootstrap test (Ebisuzaki 1997) are contoured.

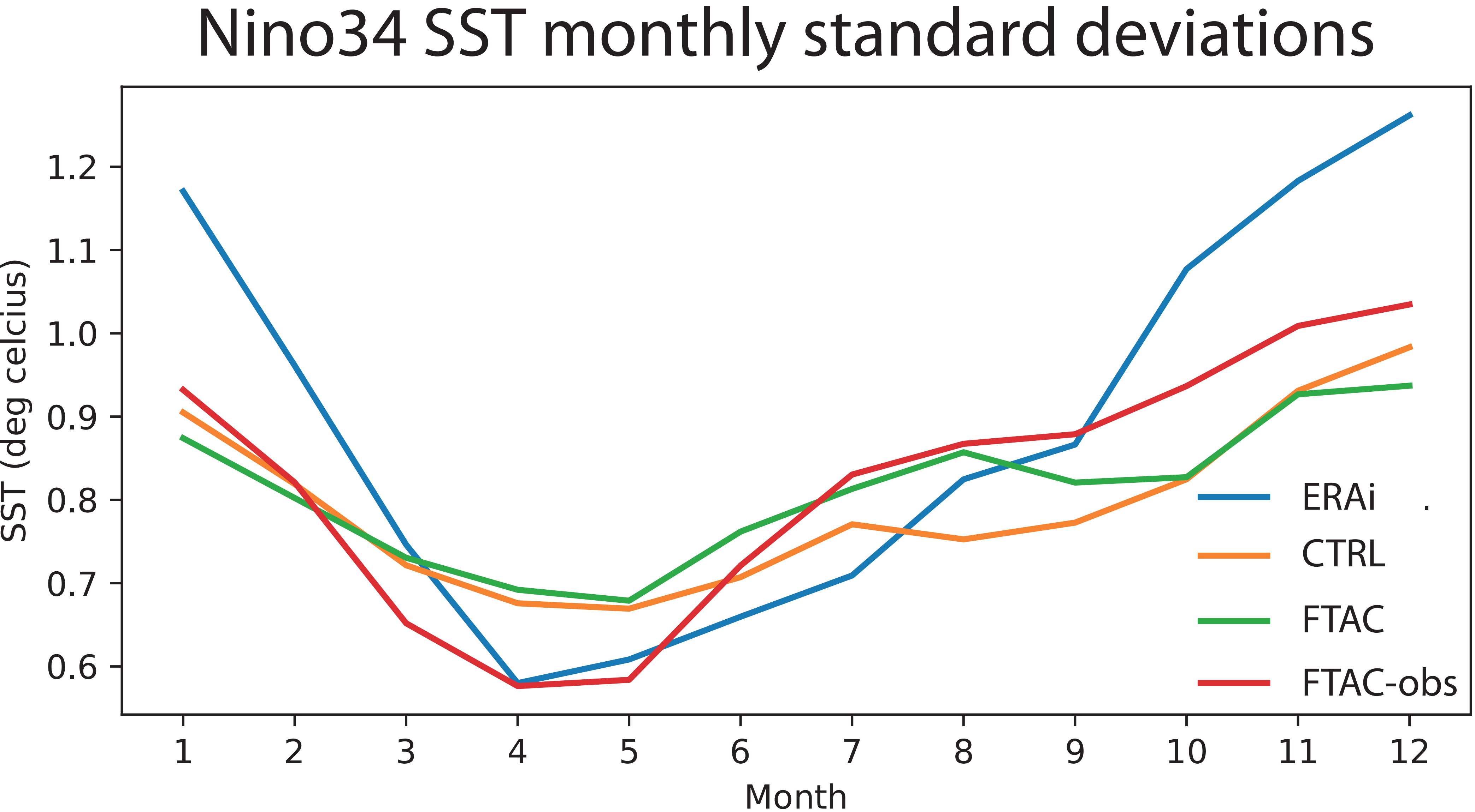

Figure 8: Monthly standard deviations of Nino34 SST (unit:°C) from ERAi (blue), CTRL (orange), FTAC (green) and FTAC-obs (red).

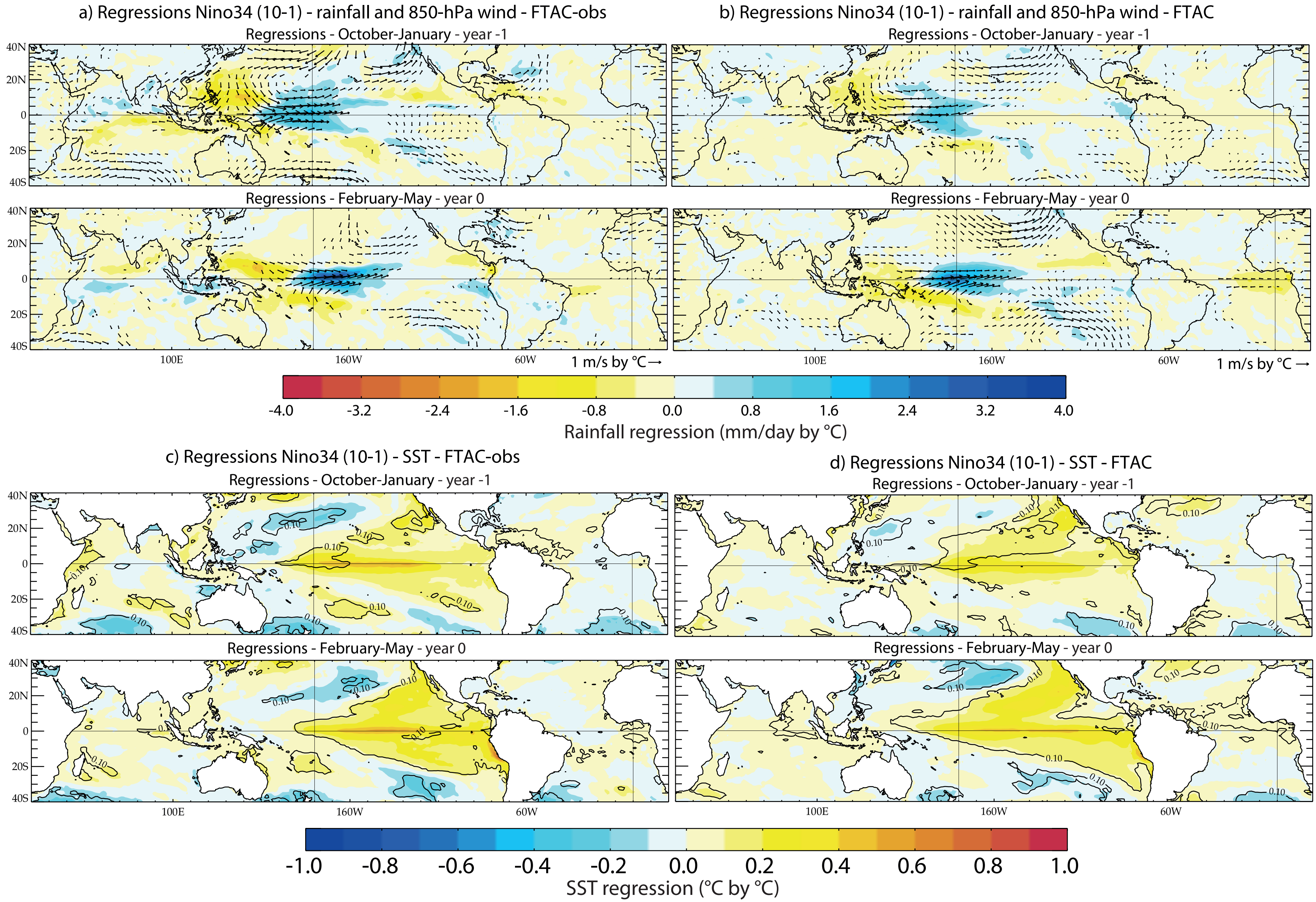

Figure 9: a) Quarterly rainfall and 850-hPa wind time series during boreal winter and spring regressed against the Nino34 index during the following boreal winter (e.g. ONDJ Nino34 SST) in FTAC-obs. b) Same as a), but in FTAC. c) Quarterly SST time series during boreal winter and spring regressed against the Nino34 index during the following boreal winter in FTAC-obs. d) Same as c), but in FTAC. Unit for the SST regression coefficient is °C by °C. Units for the rainfall and 850-hPa wind regression coefficients are mm/day by °C and m s-1 by °C, respectively. Regression coefficients reaching the 90% significance level according to a phase-scrambling bootstrap test (Ebisuzaki 1997) are contoured (SST or 200-hPa velocity potential) or shown (rainfall and 850-hPa wind).

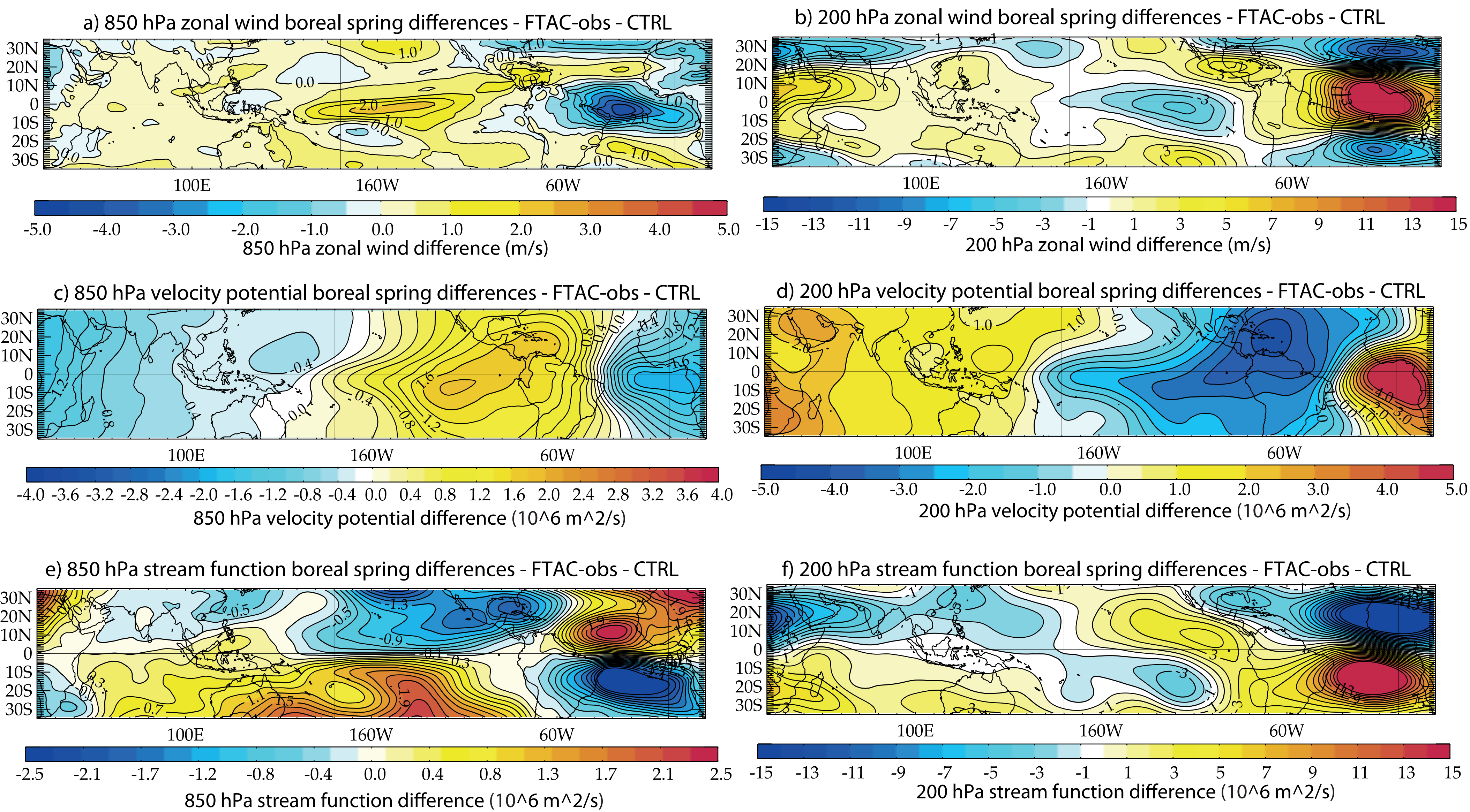

Figure 10: a) 850-hPa zonal wind boreal spring means differences (unit: m s-1) between FTAC-obs and CTRL; b) 200-hPa zonal wind boreal spring means differences (unit: m s-1) between FTAC-obs and CTRL; c) 850-hPa velocity potential boreal spring means differences (unit: 106 m2 s-1) between FTAC-obs and CTRL; d) 200-hPa velocity potential boreal spring means differences (unit: 106 m2 s-1) between FTAC-obs and CTRL; e) 850-hPa stream function boreal spring means differences (unit: 106 m2 s-1) between FTAC-obs and CTRL; f) 200-hPa stream function boreal spring means differences (unit: 106 m2 s-1) between FTAC-obs and CTRL.

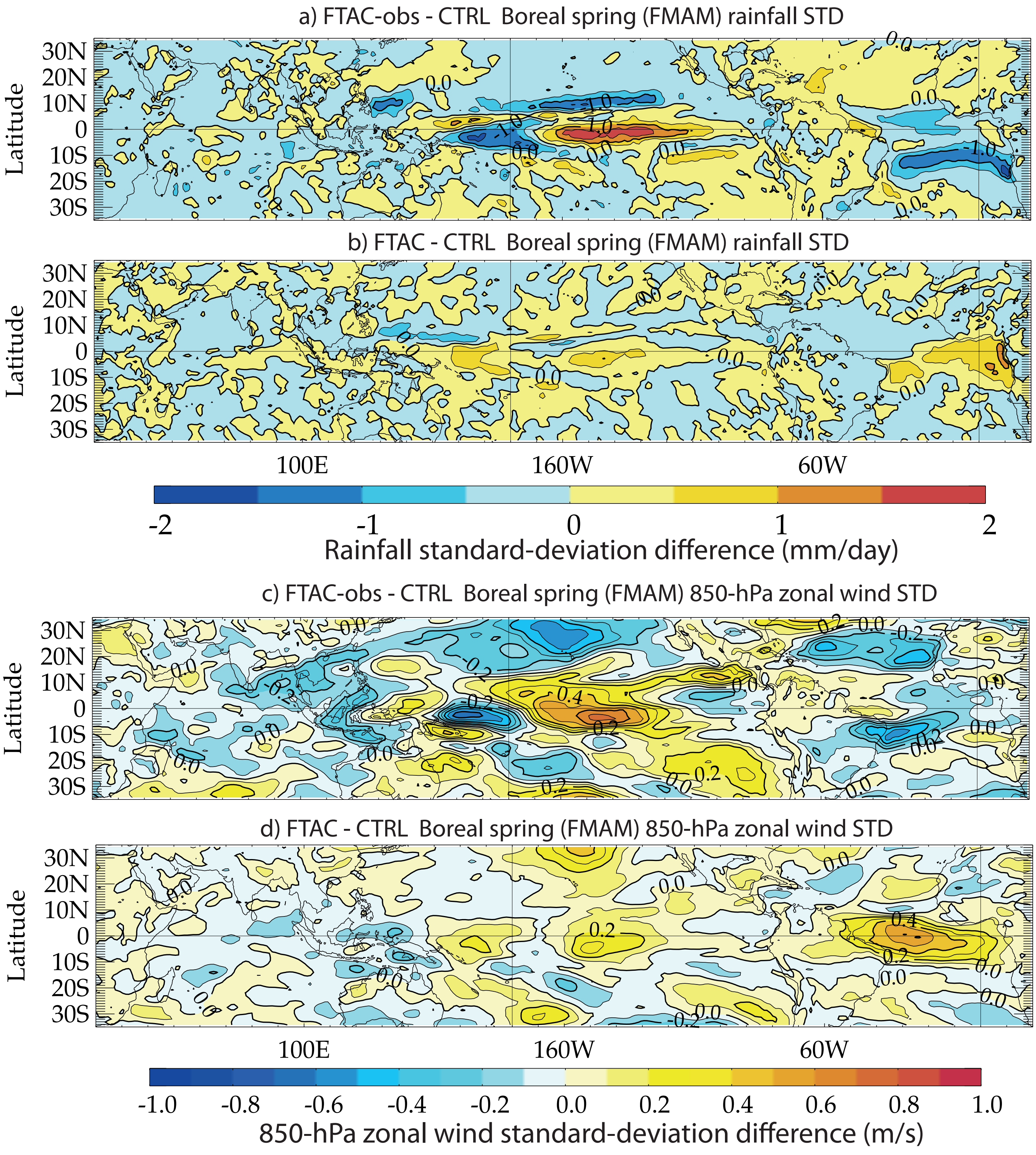

Figure 11: a) Rainfall boreal spring standard deviation differences (unit: mm/day) between FTAC-obs and CTRL. b) Same as a), but for FTAC and CTRL. c) 850-hPa zonal wind boreal spring standard deviation differences (unit: m s-1) between FTAC-obs and CTRL. d) Same as c), but for FTAC and CTRL.

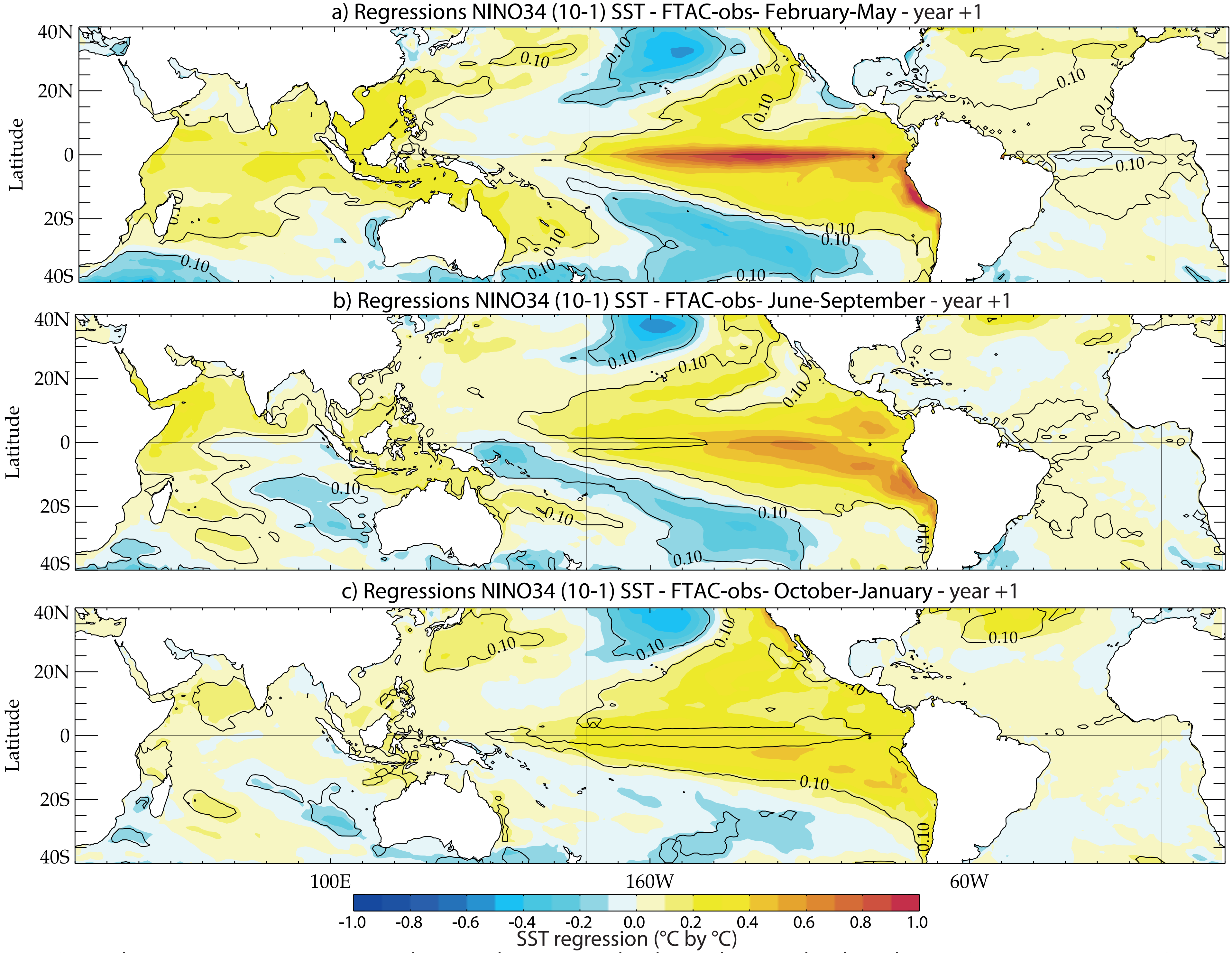

Figure 12: a) Boreal spring SST time series regressed against the Nino34 index during the preceding boreal winter (e.g. ONDJ Nino34 SST) in FTAC-obs; b) Boreal summer SST time series regressed against the Nino34 index during the preceding boreal winter in FTAC-obs; c) Boreal winter SST time series regressed against the Nino34 index during the preceding boreal winter in FTAC-obs. Unit for the SST regression coefficient is °C by °C. Regression coefficients reaching the 90% significance level according to a phase-scrambling bootstrap test (Ebisuzaki 1997) are contoured.

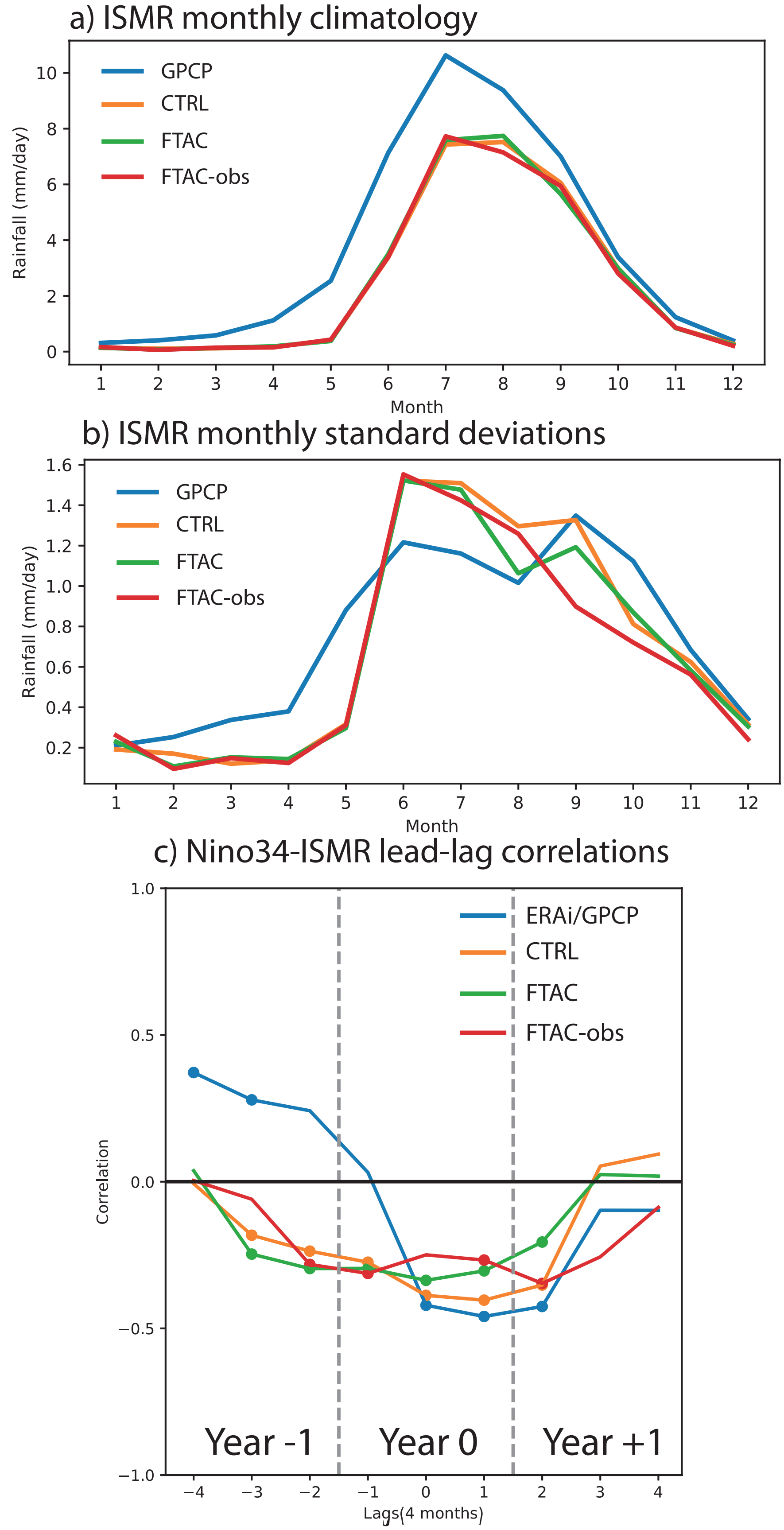

Figure 13: a) Monthly means of ISMR (unit: mm/day) from GPCP (blue), CTRL (orange), FTAC (green) and FTAC-obs (red); b) Monthly standard deviations of ISMR (unit: mm/day) from GPCP (blue), CTRL (orange), FTAC (green) and FTAC-obs (red); c) Lead-lag correlations between ISMR and quarterly Nino3.4 SSTs starting from the beginning of the previous year (e.g. year - 1) to the end of the following year of the monsoon (e.g. year +1) in observations (blue), CTRL (orange), FTAC (green) and FTAC-obs (red). X-axis indicates the lag (in 4 months interval) for a 36 months period starting one year before the developing year of ISMR (e.g. year 0) and Y-axis is the amplitude of the correlation. Thus, the coefficients corresponding to -1, 0, +1 lags refer, respectively, to the correlations between ISMR in year 0 (e.g. JJAS ISM rainfall) and February-May, June-September and October-January Niño-3.4 SSTs, also during year 0, and so on. Circles indicate correlations that are above the 90% significance confidence level according to a phase-scrambling bootstrap test (Ebisuzaki 1997).

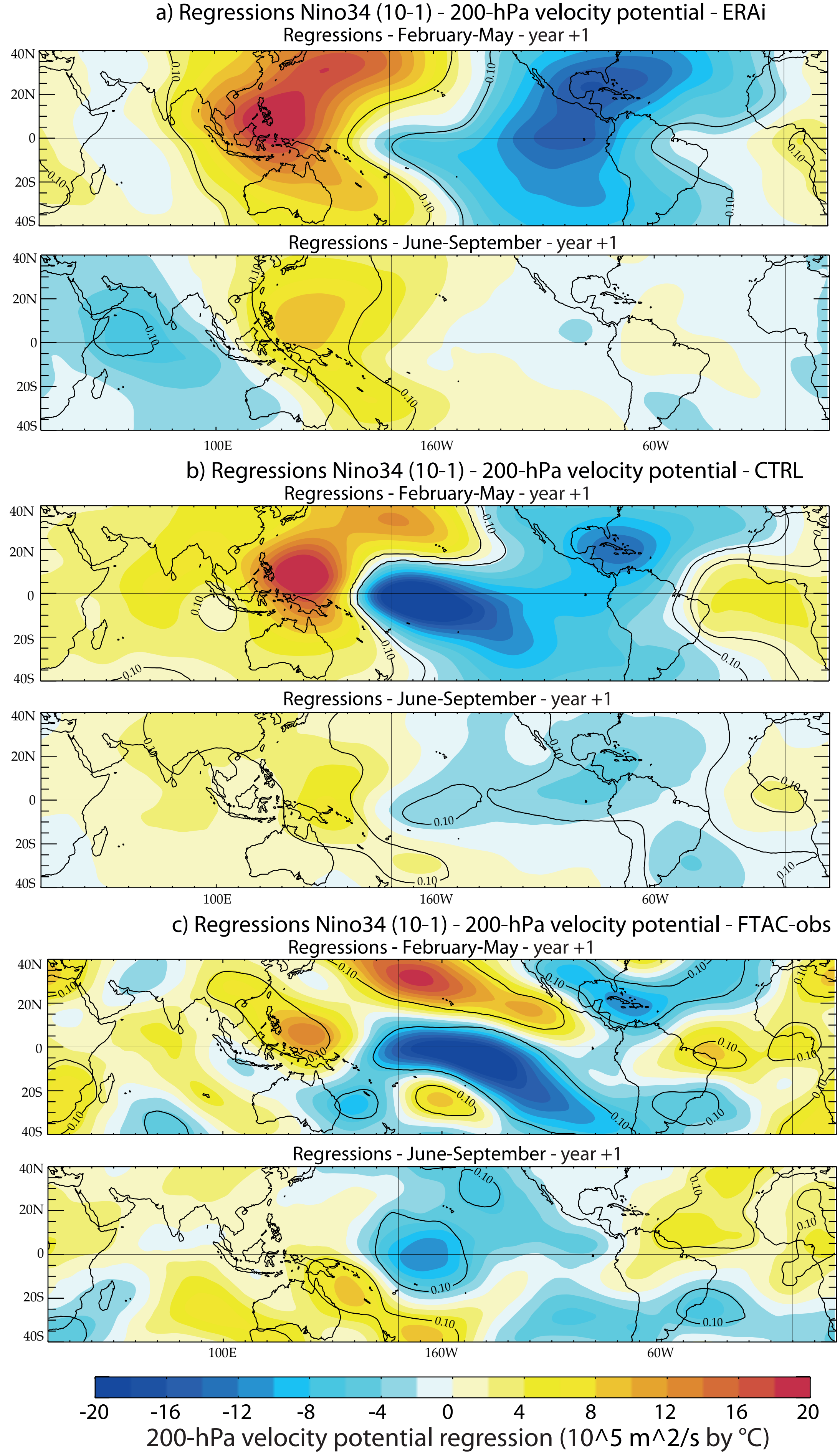

Figure 14: a) Boreal spring and summer 200-hPa velocity potential time series regressed against the preceding boreal winter Nino34 SST in ERAi. b) Same as a), but for CTRL. c) Same as a), but for FTAC-obs. Unit for the 200-hPa velocity potential regression coefficient is 105 m2 s-1 by mm/day. Regression coefficients reaching the 90% significance level according to a phase-scrambling bootstrap test (Ebisuzaki 1997) are contoured.

Table 1

Name	CTRL	FTPC	FTPC-obs	FTAC	FTAC-obs
Correction area	None	Pacific Ocean coast to coast 25°S-25°N	Pacific Ocean coast to coast 25°S-25°N	Atlantic Ocean coast to coast 25°S-25°N	Atlantic Ocean coast to coast 25°S-25°N
Smoothing area	None	30°S-25°S 25°N-30°N	30°S-25°S 25°N-30°N	30°S-25°S 25°N-30°N	30°S-25°S 25°N-30°N
SST data	None	CTRL	OISSTv2	CTRL	OISSTv2
Time duration (Year)	210	110	50	110	50

Table 1: Summary of the numerical experiments with their main characteristics, including length, nudging domain and SST climatology used for the nudging in the AO or PO decoupled experiments. The nudged experiments are the Forced Tropical Pacific Climatology (FTPC), the Forced Tropical Pacific observed Climatology (FTPC-obs), the Forced Tropical Atlantic Climatology (FTAC) and, finally, the Forced Tropical Atlantic observed Climatology (FTAC-obs) runs. See text for more details. For the FTPC and FTPC-obs experiments only ocean grid-points in the PO are included in the correction or smoothing areas and, similarly, for the FTAC and FTAC-obs experiments. The different correction domains are also displayed in Figure 1a. The observed SST daily climatology used in the FTPC-obs and FTAC-obs experiments is derived from the AVHRR only daily Optimum Interpolation SST version 2 (OISSTv2) dataset for the 1982-2010 period (Reynolds et al. 2007).

Click here to access/download
Electronic Supplementary Material
FigureS1.eps

Click here to access/download

Electronic Supplementary Material

FigureS2.eps

Click here to access/download
Electronic Supplementary Material
FigureS5.eps

Click here to access/download
Electronic Supplementary Material
FigureS6.eps

Click here to access/download

Electronic Supplementary Material

FigureS7.eps

Anatomy of the Indian Summer Monsoon and ENSO relationship in a state-of-the-art CGCM: Role of the tropical Atlantic Ocean

Pascal Terray[1], Ligin Joseph[2], KP Sooraj[3]

[1] LOCEAN/IPSL, Sorbonne Universités (UPMC, Univ Paris 06)-CNRS-IRD-MNHN, Paris, France
[2]Institut Universitaire Européen de la Mer, Université de Bretagne Occidentale, Brest, France
[3]CCCR, Indian Institute of Tropical Meteorology, Ministry of Earth Sciences, Pune, India

Revised for **Climate Dynamics**

15~~20~~ June~~April~~ 2022

Corresponding author address: Pascal Terray, LOCEAN-IPSL, Sorbonne Universités (Campus Université Pierre et Marie Curie), BP100 – 4 Place Jussieu, 75252 Paris cedex 05, France. Tel : +33 1 44 27 70 72. E-mail : pascal.terray@locean.ipsl.fr

Abstract

The main paradigm for prediction of Indian Summer Monsoon Rainfall (ISMR) is its inverse relation with El Niño-Southern Oscillation (ENSO). In this study, we focus on the role of the Atlantic Ocean (AO) Sea Surface Temperature (SST) variability on the ISMR. There are basically two ways by which AO SSTs can impact the ISMR: a "direct pathway" in which the AO may directly force the ISMR in the absence of interactions with other dominant forcings like ENSO, and an "indirect pathway" in which AO forces ENSO and modulates the ENSO teleconnection to ISMR. These two pathways are studied with the help of sensitivity experiments performed with a Coupled General Circulation Model (CGCM). Two pairs of decoupling experiments have been done. In the first, the SST variability in the tropical AO or Pacific Ocean (PO) is removed by nudging the SST in these regions from a control run's SST climatology. In the second set, the SST nudging is performed from the observed SST climatology, which allows us to assess the robustness of the results and the specific role of the model's SST mean-state biases.

The direct pathway linking tropical AO SST variability onto ISMR is insignificant in the PO decoupled experiments or in recent observations. Furthermore, these experiments suggest on the contrary that many AO SST anomalous patterns could be forced by ISMR. On the other hand, for the indirect pathway, the AO decoupled experiments demonstrate that AO SST variability modulates the onset and decaying phases of ENSO events. Despite ENSO is as strong and persists longer than in the control simulation, the AO SST nudging resulted in a significant weakening of the inverse relationship between ENSO and ISMR. The ENSO-monsoon relationship is mainly modulated during the ENSO decaying phase. The upper-level divergent wind flows mainly from the Pacific to the AO resulting in rainfall suppression in the AO, but only in a weak forcing on ISMR during boreal summer of the ENSO decaying year in the AO decoupled experiments. Thus, the AO rainfall variability in these experiments is decoupled from the surface and mainly modulated by the upper-level convergence or divergence induced by the remote ENSO forcing.

Finally, the rectification of the AO SST mean-state biases in the CGCM also induces an El Niño-like mean pattern over the tropical Pacific during boreal spring and promotes a stronger ENSO during its peak phase. This demonstrates that the prominent AO SST mean-state biases in current CGCMs further complicate the dynamical prediction and simulation of ISMR and ENSO.

Keywords: Indian Summer Monsoon; El Niño-Southern Oscillation; tropical Atlantic Ocean; ocean-atmosphere interactions; Walker circulation, coupled climate model.

1. Introduction

In India, the rainy season is from June to September (JJAS) and Indian Summer Monsoon Rainfall (ISMR) provides 80% of India's total annual precipitation. Despite the standard deviation of ISMR is only about 10% of its mean, ISMR variability has a tremendous impact on water resource management, agricultural yield and India's gross domestic product (Gadgil and Gadgil 2006). However, forecasting ISMR variability is still a scientific challenge (Rao et al. 2019) and an active research area as it involves many factors and their complex interactions (see Chowdary et al. 2021 for recent review).

Numerous studies have examined climatic controls on ISMR interannual variability and most of them showed the role played by tropical Pacific, Indian and Atlantic oceans Sea Surface Temperature (SST) anomalies (Chowdary et al. 2021). El Niño-Southern Oscillation (ENSO) is the primary forcing of year-to-year ISMR variability (Webster et al. 1998). However, since ENSO can only explain about 35% the interannual variance of ISMR and the ISM-ENSO relationship has weakened during the latter part of the 20th century, partly in response to coherent multi-decadal variability of the climate system (Kumar et al. 1999; Kucharski et al. 2007; Srivastava et al. 2019; Yang and Huang 2021), it is important to look for other sources of ISMR predictability.

First, many studies have suggested a connection between ISM and Indian Ocean (IO) SSTs, especially the Indian Ocean Dipole (IOD; see reviews in Cherchi et al. 2021). The IOD is an irregular interannual SST oscillation in which the eastern equatorial IO gets alternately colder and then warmer than the western part during boreal fall. Positive IOD events (e.g., warm in the western IO) may enhance ISMR through moisture transport over the western IO or modification of the local Hadley cell with increased ascendance over the Indian region (Cherchi et al. 2021). However, the influence of IOD on both ISMR and ENSO remains a controversial topic (Meehl et al. 2003; Fischer et al. 2005; Izumo et al. 2010; Cretat et al. 2017, 2018; Stuecker et al. 2017; Terray et al. 2021; Cherchi et al. 2021; Zhang et al. 2021a).

The Atlantic Ocean (AO) can also add its impact on ISMR (Kucharski et al. 2007, 2009; Pottapinjara et al. 2014, 2016; Sabeerali et al. 2019; Vittal et al. 2020; Yang and Huang 2021). First, a basin-warming mode exists in the tropical AO and is known as Atlantic Niño or the Atlantic Zonal Mode (AZM; Lübbecke et al. 2018; Cabos et al. 2019; Richter and Tokinaga 2021). These Atlantic Niños peak during boreal summer and are formed due to a Bjerknes feedback as for ENSO, but last only for 3-4 months due to the weaker ocean-atmosphere interactions in this basin (Lübbecke et al. 2018; Cabos et al. 2019; Richter and

Tokinaga 2021). It is still debated whether and how ENSO affects the AZM (Tokinaga et al. 2019). However, Atlantic Niños give rise to important shifts in local rainfall and are associated with a Matsuno-Gill atmospheric response during boreal summer (Gill 1980; Kucharski et al. 2009; Li et al. 2016; Jiang and Li 2021), which may modulate the tropospheric temperature gradient in the Indo-Pacific sector and ISMR (Kucharski et al. 2009, Pottapinjara et al. 2014, 2016; Sabeerali et al. 2019; Jiang and Li 2021). The second leading mode of tropical AO SST variability involves fluctuations of the interhemispheric SST gradient in the AO and is known as the Atlantic Meridional Mode (AMM; Chiang and Vimont 2004; Jiang and Li 2021). The AMM is triggered and sustained by a Wind-Evaporation-SST (WES) feedback (Chiang and Vimont 2004; Cabos et al. 2019). However, the Tropical North Atlantic (TNA) SST anomaly dominates AMM variability (Enfield and Mayer 1997; Jiang and Li 2021) and ENSO plays a dominant role in causing the spring time trade wind variability over the TNA and the generation of local SST anomalies by evaporative cooling/warming through ENSO teleconnections (Enfield and Mayer 1997; Garcia-Serrano et al. 2017; Jiang and Li 2019). A few studies also suggest a link between the AMM or warm SST TNA anomalies and ISMR (Vittal et al. 2020; Yang and Huang 2021).

An important difficulty for assessing the role of AO on ISMR, is that it interacts also directly with the PO and IO in a complex manner and at different time scales (Kucharski et al. 2009, 2011; Rodriguez-Fonseca et al. 2009; Ham et al. 2013ab, McGregor et al. 2014, 2018; Li et al. 2016; Terray et al. 2016; Wang et al. 2017; Cai et al. 2019; Li et al. 2020; Jiang and Li 2021; Zhang and Han 2021). Recent studies suggest that warm TNA and AZM SST anomalies can force a La Niña-like SST pattern in the Pacific (Rodriguez-Fonseca et al. 2009; Ding et al. 2012; Ham et al. 2013ab; Wang et al. 2017; Jiang and Li 2021). But, again the role of AO in ENSO and ISMR is debated in the literature (Ding et al. 2012; Zhang et al. 2021b; Richter et al. 2021). As an illustration, previous studies suggest that Altantic Niños may reduce ISMR (Kucharski et al. 2007, 2009; Pottapinjara et al. 2016), but at the same times it may promote La Niña conditions over the Pacific (Rodriguez-Fonseca et al. 2009; Ding et al. 2012; Jiang and Li 2021), which will be associated with enhanced ISMR. Therefore, it is difficult to isolate the net effect of AO SST anomalies as the players, ISM, ENSO and AO modes interact with each other in multiple different ways (Kucharski et al. 2009; Ding et al. 2012; Ham et al. 2013b; Cai et al. 2019; Jiang and Li 2021; Yang and Huang 2021).

This review highlights that there are two pathways by which the AO SSTs can affect ISMR, one by a “direct” forcing on the ISMR and the other, “indirect”, by the AO forcing on ENSO, which, in turn, will modulate the ISMR. However, as noted above, these two pathways are not really independent of each other and the complexity of these interactions implies that it is very difficult to assess the distinct causal relationships between the Atlantic, Indian and Pacific SSTs and ISMR, or even the net effect of AO SSTs on ISMR from observations alone. Considering these difficulties, we will assess the role of the tropical AO on ISMR with the help of dedicated experiments performed with a Coupled General Circulation Model (CGCM).

This paper is organised as follows. The validation datasets, CGCM and sensitivity experiments used in this study are described in Section 2. In Section 3, the observed and simulated relationships between ISMR, ENSO and AO SSTs at the interannual time scale are documented. In Section 4, the AO "direct" and "indirect" effects on ISMR are assessed through sensitivity coupled experiments. The final section summarizes the results of the present work and presents some perspectives.

2. Datasets, coupled model and sentivity experiments

2.a Observed datasets and time series indices.

Multiple data sources are used for model validation. SST and atmospheric variables (e.g., 850- and 200-hPa winds, velocity potentials and stream functions) are taken or computed from ERA-Interim reanalysis (ERAi; Dee et al. 2011) available from 1979 onwards. The depth of the 20°C isotherm (Z20) is used as a proxy of the thermocline depth and is extracted from the Simple Ocean Data Assimilation reanalysis for the 1979-2010 period (Carton and Giese 2008; SODA version 2.2.4). We also used the Global Precipitation Climatology Project rainfall dataset (GPCP; Huffman et al. 2001), which combines measures of precipitation gauges and satellite data. GPCP is analyzed for the 1979-2016 period. All these quantities are interpolated onto the model resolution to foster direct comparison with the simulations.

To monitor ISM, ENSO and AZM variability both in observations and simulations, we define three standard time series indices:

- The ISMR time series is defined as the average of rainfall anomalies for the land grid points in the region 5°-25°N and 70°-95°E.

- The Niño-3.4 SST (monthly average of SST anomalies in the region 5°S-5°N and 170°-120°W; Nino34 hereafter) time series is chosen for the ENSO index since in observations the strongest correlations between ISMR and tropical Pacific SSTs occur over this region.

- The ATL3 SST (monthly average of SST anomalies in the region 3°S-3°N and 20°W-0°E) time series, which is a convenient index for the AZM (Lübbecke et al. 2018).

Note that our analysis of observations is robust if we estimate our Nino34, ATL3 and ISMR time series from the Hadley Centre Sea Ice and SST dataset (Rayner et al. 2003) and the rainfall dataset obtained from the Indian Meteorological Department (Pai et al. 2015).

2.b Coupled model and sensitivity experiments.

Here we employ a CGCM, the SINTEX-F2 (Masson et al. 2012), to assess the influence of AO on ISMR variability and the ISM-ENSO relationship. The different model components are ECHAM5.3 atmospheric model (Roeckner et al. 2003) at T106 spectral resolution (~1.125° x 1.125°) and 31 hybrid sigma-pressure levels, NEMO ocean model (Madec 2008) at 0.5° x 0.5° horizontal resolution, 31 vertical levels and the LIM2 ice model (Timmermann et al. 2005). The three model components are coupled using the Ocean-Atmosphere-Sea-Ice-Soil (OASIS3) coupler (Valcke 2006). The model simulates the tropical Pacific SST mean state, ENSO and ISMR variability reasonably well (Masson et al. 2012, Terray et al. 2016, 2021; Cretat et al. 2017, 2018).

First, a 210-yr fully coupled ocean-atmosphere simulation is used as a control (CTRL hereafter). In order to disentangle the complex interactions between ISMR, ENSO and AO SST variability, two partially coupled configurations of SINTEX-F2 are used and two dedicated experiments have been performed with each of these configurations (see Table 1 for details). In the first partial coupled configuration, full ocean-atmosphere coupling is used everywhere except in the subtropical and tropical AO (25°S-25°N band), where SST is nudged toward a daily SST climatology computed from CTRL or AVHRR-V2 daily Optimum Interpolation SST observations during the 1982-2010 period (Reynolds et al. 2007). These two AO decoupling experiments will be called FTAC and FTAC-obs and have been run for 110-yr and 50-yr, respectively. In the second partial coupled configuration, ocean-atmosphere coupling is active except in the subtropical and tropical Pacific (25°S-25°N band) where, again, SST is nudged toward a daily SST climatology computed from CTRL or observations. These two PO decoupling experiments will be called FTPC and FTPC-obs, and have been run for 110-yr and 50-yr, respectively.

The nudging method used in these partial decoupling experiments modifies the non-solar heat fluxes in the selected domain through a correction term that completely removes the SST variability in the nudging domain (Terray et al. 2021). The damping term used in this nudging technique (-2400 W m^{-2} K^{-1}) corresponds to the 1-day relaxation time for temperature in a 50-

m ocean layer. To avoid sharp SST gradients, a buffer zone is used between the “free” ocean and regions of prescribed SST forcing such that the SSTs in these buffer regions are gradually merged (over 5° latitude) with the prescribed SSTs. This strong SST restoring leads to an almost complete decoupling between the ocean and atmosphere in the nudging domain with SSTs, which ~~will~~ differ by no more than 0.1 K from the prescribed space-time climatology.

In FTAC and FTPC, there are no significant changes in SST mean-state in the nudged region, but also in the whole Tropics compared to CTRL (not shown). On the other hand, in FTAC-obs (and also FTPC-obs), the strong SST restoring removes the SST mean-state biases present in CTRL in addition to suppressing SST variability in the selected domain. CTRL exhibits a strong warm bias in the southeast AO (Fig. 1a), which is a common problem for most CGCMs (Richter et al. 2014; Voldoire et al. 2019; Bi et al. 2022). This bias is attributed to errors in simulating zonal trade winds during boreal spring and is related to a deeper thermocline, which weakens the upwelling of cold waters in the eastern AO (Fig. 1b). Consistent with this erroneous east-west SST gradient, the rainfall pattern in the tropical AO is shifted southeastward in CTRL compared to observations (Fig. 1c). Also consistent with these mean-state biases, CTRL simulates a weaker SST variability over the eastern equatorial AO compared to observations (Fig. S1b), especially during boreal summer, which is the season of maximum SST variability in observations (Fig. S1a) as this is also the season when the (observed) thermocline is the shallowest. Focusing on the PO, we note that CTRL is also affected by a double Inter-Tropical Convergence Zone (ITCZ) bias (Fig. 1c) and a reduced ENSO amplitude during boreal winter (Fig. S1b). As we will demonstrate in the following sections, the inability of CTRL to realistically reproduce the seasonal cycle in the AO is a cause of concern not only for the AO region, but also for ENSO and ISMR.

On the other hand, the SST restoring applied in FTAC-obs is able to correct largely these simulated SST, thermocline and rainfall errors in the AO and also produces some changes in the two other tropical basins (Figs. 1d-f). In other words, the comparison of CTRL, FTAC and FTAC-obs (or FTPC and FTPC-obs) runs is ~~can be~~ useful to isolate the specific contribution of the biased SST background mean-state in the coupled model.

More generally, the aim of these simulations is to isolate the effects of the PO and AO SST variability on the simulated ISMR and ENSO-ISM relationship. First, FTPC and FTPC-obs will be used to assess the « direct » relationship between AO SSTs and ISMR in a climate without any counteracting ENSO forcing. Second, FTAC and FTAC-obs are useful to assess if and how AO SST variability modulates ENSO and the simulated monsoon-ENSO relationship, e.g. if AO SST anomalies are able to produce an « indirect » effect on the ISMR.

Table 1 summarizes the specifications of the simulations used here and the different nudging domains are displayed in Fig. 1a. Finally, in all the analyses described below, the first 10 years of all simulations have been excluded due to the spin-up of the coupled model.

3. ISMR, ENSO and AO relationships in observations and SINTEX-F2

3.a AO SST variability and its relationship with ENSO in SINTEX-F2

Before assessing the role of AO SST variability on ISMR and its relationship with ENSO, it is important to document the performance of SINTEX-F2 in simulating AO variability, especially the AZM and AMM (see Introduction for details). In this way, we can first appreciate if the SST, rainfall and Z20 mean-state biases discussed in Section 2 are also a cause of concern for a realistic simulation of AO SST variability in CTRL. Such analysis will also be useful to interpret the differences between the AO decoupled experiments and CTRL in the following sections as the nudged AO region encompasses the tropical AO.

AZM and AMM are the two dominant modes of SST monthly anomalies in the tropical AO (Lübbecke et al. 2018; Cabos et al. 2019 and references herein). Thus, Empirical Orthogonal Function (EOF) analysis of observed and simulated tropical AO SST monthly anomalies provides a convenient tool for describing the performance of CTRL in simulating both the AZM and AMM modes and their relative importance. Note also that the different datasets have been detrended before the EOF analysis. Fig. 2 displays the first two leading EOFs of observed and simulated monthly SST anomalies in the tropical AO. These two EOFs of ERAi and CTRL SSTs are clearly distinct from the lower EOFs as EOF3 accounts for only 8% of the AO SST variance in both ERAi and CTRL (not shown).

The first EOF of ERAi SSTs describes 25% of the AO SST variance and depicts a basin-wide pattern with positive SST anomalies covering the whole tropical AO (Fig. 2a). However, the spatial loadings in this EOF1 are particularly high in the coastal upwelling regions near the Angola–Benguela coast and in the equatorial cold tongue region explaining why this first EOF is usually associated with the AZM in the literature (Lübbecke et al. 2018; Cabos et al. 2019; Jiang and Li 2021). The second EOF of ERAi SSTs accounts for 23% of the AO SST variance (Fig. 2b). This EOF2 depicts a cross-equatorial SST gradient in the AO, which is usually interpreted as the manifestation of the AMM (Chiang and Vimont 2004; Cabos et al. 2019). These two leading EOFs are very similar to other published EOF analysis of AO SSTs using different datasets, spatial domains or time periods, both in terms of spatial patterns and variance described ~~explained~~ by these leading modes (Lübbecke et al. 2018; Cabos et al.

2019; Jiang and Li 2021). Of special interest is the possible connection of these two leading EOFs with ENSO, which is simply assessed here by computing the simultaneous correlation between the associated amplitude monthly time series and the Nino34 index. These observed EOF modes have no simultaneous relationship with ENSO (r=-0.07 and 0.08 for Nino34 vs EOF1 and EOF2, respectively). Their lead and lag relationships with Nino34 index will be explored in Section 3.c.

~~The results (-0.07 for EOF1 and 0.08 for EOF2) suggest that these EOFs are not linearly linked to ENSO (at least when all months and no lags are taken into account) as both correlations are statistically insignificant even at the 80% confidence level according to a phase-scrambling bootstrap test (Ebisuzaki 1997).~~

Figs. 2cd display the two leading EOFs of CTRL SST monthly anomalies in the same AO domain, which explain, respectively, 28 and 16% of the SST variance. SINTEX-F2 is able to simulate with a reasonable accuracy both the spatial patterns and variances described by the leading EOFs of observed AO SSTs as well as their relative importance in term of explained variance. Note, however, that the L-shaped structure of the anomalous SSTs linking the equatorial cold tongue to the southeast AO in EOF1 of observed SSTs is not well represented and shifted westward in the EOF1 of simulated SSTs. This suggests that AZM events may be weaker and are partly disconnected from the upwelling region near the Angola–Benguela coast in CTRL compared to observations. This error is further confirmed by the comparison of observed and simulated SST monthly means and standard-deviations in the ATL3 region (Fig. 3). Consistent with Fig. 1a, ATL3 region is affected by a warm mean-state bias, which is particularly prominent during June-July when the observed ATL3 SST variability is maximum (Fig. 3), which corresponds to the peak of AZM events in observations (Lübbecke et al. 2018). By contrast, the simulated ATL3 SST variability is prominent around three months earlier and is drastically reduced in amplitude. This shortcoming, which is also found in many other CGCMs (Voldoire et al. 2019; Bi et al. 2022), is~~may be~~ related to the coupled mean-state biases (e.g., SST, Z20, rainfall, etc.) reducing the intensity of the equatorial cold tongue during boreal summer in CTRL, especially the flatten thermocline in the equatorial AO, which may reduce the thermocline feedback and, thus, weakens the local Bjerknes feedback and the AZM variability (see Figs. 1 and S1). The observed ATL3 SST variability has also a secondary peak in winter, but this weaker maximum is well simulated in CTRL (Fig. 3b). On the other hand, the second EOF of simulated AO SSTs closely matches the second EOF estimated from ERAi SSTs in terms of spatial pattern and can also be regarded as the manifestation of the AMM (Figs. 2bd). Finally, the correlations between the associated two amplitude time series and the Nino34 index in CTRL are, respectively, 0.36 and 0.01, and the first correlation is highly significant, even at the 99.9 % confidence level according to a phase-scrambling bootstrap test (Ebisuzaki 1997). This suggests a significant association of the simulated AZM with ENSO in CTRL, which is not found in observations (see above). On the other hand, EOF2 of (simulated) AO SSTs, which can also be regarded as the manifestation of the AMM, is not significantly associated with ENSO in CTRL; a result consistent with ~~the one found from~~ observations.

In summary, the two leading modes of the tropical AO SST variability in CTRL share many features with those in observations, but the simulated AZM has a much weaker amplitude and a significant relationship with ENSO, suggesting a too strong ENSO teleconnection to the tropical AO or vice versa.

3.b ISMR regression analysis

We now present the results of a lead-lag regression analysis of tropical SST, rainfall, 850-hPa wind and 200-hPa velocity potential quarterly time series onto the ISMR index in order to provide a clear picture of the relationships between ISMR, ENSO and AO climate variability in observations and CTRL (Figures 4 and 5). The ISMR index is fixed at the JJAS season and the 4-month averaged SST, rainfall, 850-hPa wind and 200-hPa velocity potential time series are shifted backward and forward in time. The results are presented in a two-year window from the beginning of year -1 (preceding the ISMR year) to the end of year 0, year 0 referring to the year of the ISM season. Note that the results remain unchanged if the different time series are detrended before the regression analysis (not shown). While it is known that the ISM-ENSO relationship includes some asymmetry in observations (Terray et al. 2003, 2005; Boschat et al. 2012; Chakraborty and Singhai 2021), this regression analysis is used here as a first order method to assess the realism of CTRL in simulating the ISMR teleconnections.

The regression results from observations (Fig. 4) illustrate that ISMR is associated with different phases of ENSO in a two-year window (Boschat et al. 2012; Chakraborty 2018). Strong positive SST anomalies in the central and eastern PO, which are out of phase with anomalies in the western part of the PO are found during year -1, consistent with the occurrence of an El Niño one year before a strong ISM (Fig. 4a). The atmospheric anomalous patterns are consistent with this hypothesis as they describe an eastward shift of the Pacific Walker circulation with persistent westerly 850-hPa wind anomalies over the western equatorial Pacific, positive rainfall anomalies and negative 200-hPa velocity potential anomalies over the central Pacific during year -1 (Figs. 4bc). The regression patterns during year 0 are more or less a mirror image of those during year -1 with an opposite sign (Fig. 4). In other words, this analysis demonstrates that ENSO and ISMR are still highly inter-related and followed a sustained biennial rythm during recent decades (Meehl et al. 2003; Terray et al. 2003, 2021).

Focusing now on the relationships between ISMR and IO SSTs, we note that IO SST anomalies are small and insignificant during boreal winter of year -1 and the pre-monsoon period of year 0. During boreal summer of year 0, the IO is also devoid of any significant SST anomalies associated with ISMR variability (Fig. 4a). This suggests that the « direct » effect of IO SSTs on ISMR is small (Cretat et al. 2017; Terray et al. 2021).

On the other hand, a significant positive correlation emerges between TNA SSTs during boreal spring of year 0 and ISMR (Fig. 4a). This result is in agreement with the results of Vittal et al. (2020), Yang and Huang (2021) and Ham et al. (2013ab), which suggest that TNA SSTs during boreal spring are a significant precursor of ISMR and can also serve as a trigger for the following La Niña event, respectively. However, this statistical relationship quickly fades away during boreal summer of year 0 (Fig. 4a). Furthermore, during ISM, the SST anomalies are insignificant in the tropical AO, which partly disagree with recent studies highlighting the role of AZM on the ISMR (Kucharski et al. 2007, 2009; Pottapinjara et al. 2014), but are in agreement with the work of Ding et al. (2012).

In order to further elucidate the relationships between tropical SSTs, ENSO and ISMR in observations, the above lead-lag regression analysis has been repeated after removing the ENSO contribution to the monthly SST fields by a simple linear regression method (Fig. S2a). This is equivalent to assume that ENSO has a simultaneous linear impact on tropical SSTs (Kucharski et al. 2009). Despite the simplicity of this approach, the results demonstrate that most of the lead-lag relationships between tropical SST anomalies and ISMR (displayed in Fig. 4a) can be understood as the results of simultaneous ENSO teleconnections on both ISMR and SST anomalies elsewhere, as most of the correlations are now insignificant, especially those during boreal summer of year 0 (Fig. S2a). One notable exception is, however, again the TNA SSTs during boreal spring of year 0, which remain significant at the 90% confidence level even after removing the ENSO contribution from the observed SST fields. On the other hand, despite the independence of AZM and ENSO in observations (see Section 3.a) and removal of the ENSO-related contribution to the SST anomalies, the tropical AO SSTs are again not linearly linked to ISMR during year 0.

CTRL is performing relatively well in reproducing the simultaneous inverse relationship between ISMR and ENSO during year 0 (Fig. 5). However, the model fails to reproduce the significant positive lead correlation between TNA SSTs during boreal spring and the following ISM. Also, ISMR is much more linked to ENSO during year -1 and the pre-monsoon season of year 0 in CTRL (Fig. 5; see also Terray et al. 2021). This suggests an overly strong control of ENSO on ISMR in CTRL as for the AZM (see Section 3.a above). Removing the ENSO contribution to the CTRL monthly SST fields by a simple linear regression method before the regression analysis reveals a significant contribution of the subtropical North Pacific SST anomalies during year 0, but again no significant relationships with TNA or tropical AO SSTs during year 0 (Fig. S2b).

In the context of the ENSO-ISM relationship, the physical consistency of a direct link between TNA SSTs during boreal spring and ISMR independent of ENSO, as found in observations, is thus questionable. This positive correlation between TNA SSTs during boreal spring and ISMR may be more an artifact of the ENSO forcing on both TNA and ISMR than a sign of a physical connection between TNA SSTs and ISMR (Zhang et al. 2021b). This alternative scenario is also consistent with the significant La Niña SST and atmospheric patterns during year 0, associated with the ENSO biennial rhythm during recent decades (Fig. 4a; Wang et al. 2017), and the insignificant atmospheric anomalous patterns over TNA during boreal spring of year 0 in our ISMR regression analysis from observations (Fig. 4bc).

3.c Nino34 regression analysis

We now revisit the two-way interactions between AO SSTs and ENSO for a better understanding of the AO SSTs and ISMR relationships. Figures S3 and S4 show the lead-lag regressions between the Nino34 index during boreal winter (e.g., ONDJ season) and tropical SST, rainfall and 850-hPa wind anomalies, again during a two-year window, in both observations and CTRL. In the following discussion, we will refer to year 0 as the developing year and year +1 as the decaying year of ENSO events, respectively. CTRL reproduces reasonably well the observed lifecycle of ENSO events with El Niño onset during boreal spring, a developing phase during boreal summer and fall, a peak phase during boreal winter and a decaying phase during boreal spring and summer of year +1 (Fig. S3).

The SST and atmospheric anomalous patterns during ENSO onset (e.g., during boreal spring of year 0) are very similar in observations and CTRL and are reminiscent of the Seasonal Footprinting Mechanism (SFM; Vimont et al. 2003; Boschat et al. 2013). We also note significant cold SST anomalies in the tropical AO and TNA during boreal spring of year

0 (~~, ~~especially in observations see ~~(~~Fig. S3a)~~,~~ consistent with past studies (Rodriguez-Fonseca et al. 2009; Ham et al. 2013ab; Jiang and Li 2021). Ham et al. (2013a) argues that these TNA SST anomalies may influence the tropical PO and that this forcing is mediated by the SFM (Fig. S4a). Such TNA forcing on El Niño onset is also suggested in CTRL, but with much weaker amplitude (Figs. S3b and S4b).

A first notable difference between CTRL and observations is that simulated ENSO teleconnections are significantly stronger than observed, as illustrated by the enhanced IO and AO basin-wide warming in CTRL at the end of year 0 (Fig. S3b). The rainfall response over the central equatorial Pacific per °C of Nino34 warming during boreal winter of year 0 is much stronger in CTRL; about 5 mm/day per °C against only 2.6 mm/day per °C in observations (Fig. S4). The associated latent heating induces an enhanced tropospheric warming, which stabilizes the atmosphere and reduces convection, cloudiness and evaporation over the AO and IO more in CTRL than in observations (not shown; Chiang and Sobel 2002; Chang et al. 2006).

The climate anomalies during year +1 depict~~s~~ the transition from El Niño to La Niña (or vice versa since the analysis is linear) and the related changes in ENSO teleconnections (Figs. S3 and S4). First, the simulated and observed SST anomalies during boreal winter of year 0 and spring of year +1 show that most warm TNA events can be initiated by ENSO itself (see Fig. S3; Garcia-Serrano et al. 2017; Jiang and Li 2019). This TNA warming is mainly driven by the weakening of the local northeasterly trade winds during FMAM of year +1 in both observations and CTRL (Fig. S4). These warm TNA events may induce wind anomalies over the tropical Pacific that oppose the ongoing ENSO event and accelerate its demise (Ham et al. 2013ab). This TNA forcing can be interpreted as a delayed negative feedback that accelerates the decay of ENSO as the IO capacitor effect (Xie et al. 2009, 2016; Wang et al. 2017). This is consistent with many previous CGCM studies, which found that decoupling the IO or AO in CGCMs increases the length of ENSO events (Ohba and Ueda 2007; Santoso et al. 2012; Terray et al. 2016, 2021; Kajtar et al. 2017).

A~~In this respect, a~~ second notable difference between CTRL and observations is that, despite this stronger ENSO-induced capacitor effect over the tropical IO or AO in CTRL, the simulated ENSO signal in the tropical Pacific lasts longer and persists well up to boreal summer and fall of year +1 in CTRL (Fig. S4b). This contradiction has already been examined in Terray et al. (2021) and their results highlight that, besides the amplitude of the basin-wide IO warming, the intensity of the negative IO feedback on ENSO is heavily dependent on the realism of the equatorial SST gradient in the IO during the ENSO peak and decaying phases. An open question, which will be examined with the help of partial decoupling experiments in the following section, is to determine if the erroneous mean equatorial SST gradient in the AO (Fig. 1a) is also playing a role in the longer ENSO period in CTRL.

In summary, this section illustrates how it is difficult to isolate the specific effect of AO SST anomalies on ISMR in observations or coupled simulations as the three players, ISM, ENSO and the AO SST modes, interact with each other in a complex manner.

4. AO direct and indirect effects on ISMR in SINTEX-F2

In order to assess both the possible “direct” and “indirect” effects of AO SSTs on ISMR, we now focus on the analysis of the partial decoupling experiments described in Section 2b.

4.a AO direct effect on ISMR

We estimate the "direct" effect of AO SST variability on ISMR with the help of the PO decoupling experiments in which ENSO has been removed.

In order to document how the simulated AO SST variability is modified in the absence of ENSO~~ in a first step~~, Fig. 6 displays the first two EOFs of tropical AO SST anomalies simulated in the two PO decoupling experiments. We first note that these leading EOFs estimated from FTPC and FTPC-obs are very similar both in terms of spatial pattern and described variance. EOF1 (EOF2) is associated with SST variability to the South (North) of the Equator and the Angola–Benguela (Senegal-Mauritania) upwelling system. This suggests that, in both PO experiments, these EOFs are excited by wind-driven evaporation or dynamic in each hemisphere, but that they do not involve an active WES feedback, which is usually associated with the AMM (Chiang and Vimont 2004; Cabos et al. 2019).

These EOFs can be compared to those estimated from CTRL, which are shown in Figs. 2cd. Consistent with the overly strong ENSO forcing on the simulated AZM found in CTRL (e.g., EOF1 of CTRL SSTs in Fig. 2c), the leading EOFs in the PO experiments are no more associated with SST variability in the equatorial AO and they further suggest that the two poles of the AMM may vary independently of each other. This questions the physical consistency of the AMM and its underlying mechanism, both in observations and CTRL, as its inter-hemispheric SST dipole structure depicted by the EOF2 of (observed and CTRL) AO SST anomalies may result from orthogonality constraints of the EOF analysis rather than the consequence of an active WES feedback.

The specific role of this "ENSO-free" AO SST variability in modulating ISMR is illustrated by a regression analysis of simulated SST and 200-hPa velocity potential anomalies onto the ISMR index during year 0 (Figure 7). We ~~mainly~~ focus on FTPC-obs in the rest of this section, as the results from FTPC are similar (not shown). Overall, the direct forcing of AO SST and atmospheric variability on ISMR is insignificant as the AO is devoid of any significant SST or atmospheric anomalies during the pre-monsoon season (e.g., FMAM of year 0) in FTPC-obs (Fig. 7)~~.~~. On the other hand, a well-defined atmospheric teleconnection pattern exists during boreal summer with strong 200-hPa divergence and outflow anomalies from the ISM region towards the south AO in FTPC-obs (Fig. 7b). This upper-level velocity potential pattern is obviously triggered by the diabatic heating associated with ISMR and demonstrates that ISM is a dominant feature of the boreal summer tropical circulation in the absence of ENSO. Interestingly, this ISMR forcing on the AO during boreal summer also promotes an AMM-like SST pattern during boreal fall with negative (positive) SST anomalies in the South (North) AO (Fig. 7a). This leads to the hypothesis that it is ISMR, which is forcing the AO rather than the reverse in the absence of ENSO.

4.b AO forcing on ENSO

The aim of this subsection is to isolate the effect of the AO SST mean-state bias and variability on ENSO with the help of the FTAC and FTAC-obs simulations.

To have a first basic understanding of the ENSO behavior in these two runs, Figure 8 shows the Nino34 SST monthly standard deviations from observation~~s~~, CTRL and the two AO decoupled experiments. The observed Nino34 SST variability is most prominent during boreal winter (std of about 1.2°C), and it is drastically reduced in April (about 0.6°C), which marks the onset of many ENSO events (Fig. 8). CTRL underestimates the Nino34 SST variability during boreal winter when ENSO events usually peak (Figs. 8 and S1). It is also not able to replicate the sharp decrease of Nino34 SST variability after the ENSO peak and, hence, there is an overestimation of the simulated Nino34 SST variability for a few months from March till July (Fig. 8). One interesting result is how the AO decoupled experiments alter this Nino34 SST variability (Frauen and Dommenget 2012; Ding et al. 2012; Kajtar et al. 2017). The Nino34 SST variability changes in FTAC and FTAC-obs include (i) a consistent increase during boreal summer for the two runs and (ii) an enhanced variability during boreal winter and a more realistic seasonal phase-locking in FTAC-obs compared to both CTRL and FTAC (Fig. 8).

We first focus on the increase of Nino34 SST variability during boreal summer, which is found in both FTAC and FTAC-obs (Fig. 8). In order to explain this feature, Figure 9 shows the regressions between the Nino34 index during boreal winter of year 0 (e.g., ONDJ season) and tropical SST, rainfall and 850-hPa wind anomalies during the preceding boreal winter and spring (e.g., FMAM) in FTAC and FTAC-obs. As discussed in Section 3, boreal spring is the season of El Niño onset and the results suggest that the SFM in the North Pacific plays a key-role in ENSO onset in both observations and CTRL (Figs. S3 and S4). A robust association between the SFM and El Niño onset is also found in the two AO decoupled experiments (Figs. 9ab). But, this El Niño onset occurs during boreal winter of year -1, e.g., one season before the El Niño onset in CTRL and observations, and one year before the El Niño peak (Fig. 8), a feature, which has not been well documented in past studies (Frauen and Dommenget 2012; Terray et al. 2016; Kajtar et al. 2017). Furthermore, warm SST anomalies already cover the whole central and eastern equatorial PO during boreal spring of year 0 in these two runs (Figs. 9cd), e.g. also one season in advance compared to observations or CTRL in which this basin-wide SST anomalous pattern is seen in boreal summer (Fig. S3). The associated rainfall and 850-hPa wind regression patterns during boreal spring of year 0 in FTAC and FTAC-obs also describe an eastward shift of the convection center with positive (negative) rainfall anomalies over the central (western) PO and westerly zonal wind anomalies on the western side of the positive rainfall anomalies (Figs. 9ab). All these features are fully consistent with the early El Niño onset in FTAC-obs and FTAC. Note, furthermore, that the rainfall and 850-hPa regression patterns during boreal winter and spring preceding the ENSO peak are very similar in the two AO decoupled experiments (Figs. 9ab). This suggests that this early El Niño onset can be attributed to the common cancellation of the AO SST variability in the two runs. This early El Niño onset also implies that the warm Nino34 SST anomalies associated with El Niño are already well defined during boreal summer of year 0 consistent with the enhanced Nino34 SST variability during boreal summer found in the two nudged experiments (Fig. 8). These results illustrate the important role played by AO SST variability in generating spread in ENSO timing and amplitude through its influence on the SFM. This is also consistent with several recent studies, which suggest that the SFM and its modulation are an important source of spread in ENSO forecasts during boreal spring and early summer (Ma et al. 2017; Ogata et al. 2019).

We now focus on the improved phase-locking and enhanced ENSO variability during boreal winter found in FTAC-obs (Fig. 8). In order to illustrate the seasonal dependence in the changes of ENSO variability in the different runs and isolate the role of the AO background state, Figure S5 displays the seasonal differences of SST standard-deviation between FTAC-obs and both CTRL and FTAC. Figs. S5a-c first confirm that almost all the tropical AO SST variability has been removed in FTAC-obs. Outside the AO nudged region, the SST variability changes in FTAC-obs relative to CTRL are mainly found in the tropical PO in the form of an enhanced ENSO variability from boreal summer to winter (Figs. S5b-c). This is consistent with the changes of Nino34 SST variability (Fig. 8). Furthermore, a large part of these differences can be attributed to the corrected SST AO mean state as this seasonal pattern of changes is also found in the differences of SST standard-deviation between FTAC-obs and FTAC (Figs. S5d-f). In other words, decoupling the AO SST variability without restoring the observed AO SST climatology leads only to a modest increase of ENSO variability, especially during its peak phase (Fig. 8).

In order to understand why the AO background state has such an impact on ENSO, Figure S6 displays the seasonal differences between FTAC-obs and CTRL climatologies of SST, rainfall and Z20, and Figure 10 shows boreal spring differences of 850- and 200-hPa zonal wind, velocity potential and stream function climatology between the same runs. The differences between FTAC-obs and FTAC are similar as FTAC and CTRL have the same mean state (not shown).

The correction of AO SST biases in FTAC-obs leads to drastic improvements of AO rainfall and Z20 spatial distributions during all the seasons with enhanced precipitation in the northwest tropical AO, reduced precipitation in the southeast tropical AO and, finally, a deeper Z20 in the western AO (Figs. S6bc). These rainfall changes are consistent with the imposed AO SSTs in FTAC-obs altering the regions that are above or below the threshold for deep convection in FTAC-obs compared to CTRL or FTAC (Fig. S6a). An increase of precipitation is also evident over the Amazon basin demonstrating that the reponse is not purely local. These AO rainfall shifts may exert an influence on atmospheric teleconnections because they alter diabatic heating (e.g., Gill 1980). However, surprisingly, while these rainfall changes are significant during all seasons, the rectification of the tropical PO mean state is mainly prominent during boreal spring and is characterized by a shift to an El Niño-like mean state with a warmer (cooler) eastern (western) equatorial PO, a rainfall increase in the central PO near the date line, a flatter thermocline (Figs. S6abc, first row) and, finally, a slowdown of the mean Walker circulation across the tropical PO (Figs. 10ab). The westward shift of rainfall over the AO may produce large heating anomalies at upper level centered over central South America and extending in the eastern and central PO. The 850- and 200-hPa velocity potential differences during boreal spring are in agreement with this hypothesis as they show enhanced convergence (divergence) at 850-hPa (200-hPa) toward a large region encompassing the central equatorial PO and the northwest AO and the opposite patterns elsewhere in the Tropics (Figs. 10cd). The well-defined quadrupole structure of the 850- and 200-hPa stream functions over the eastern PO/western AO (Figs. 10ef) is further consistent with the circulation expected from a Matsuno-Gill response (Gill 1980; Kucharski et al. 2009; Li et al. 2016). These features directly link SST mean-state changes in the AO with the rectification of the Pacific mean state during boreal spring. Such strong inter-basin connectivity is not seen in the other seasons despite that AO rainfall changes are still prominent (Fig. S6b). This may be related to the ITCZ and Walker cells in all oceanic basins being closer to the Equator during boreal spring, thus providing ideal conditions for the corrected rainfall and SST patterns in the tropical AO to influence the equatorial PO (Chang et al. 2006; Tokinaga et al. 2019).

Not surprisingly, the rainfall and 850-hPa zonal wind variability is also significantly enhanced and shifted eastward in the PO during boreal spring in FTAC-obs (Figs. 11ac), while the related changes are weak in FTAC (Figs. 11bd). This is consistent with the eastward shift of the mean PO SST and rainfall patterns during the same season in FTAC-obs (Figs. S6ab). Furthermore, the changes of rainfall and 850-hPa zonal wind variability over the AO are opposite in FTAC and FTAC-obs, with a large increase (decrease) of rainfall and 850-hPa zonal wind variability over the tropical AO during boreal spring in FTAC (FTAC-obs) despite the absence of AO SST variability in the two runs (Fig. 11). This again highlights strong interactions between the biased AO SST mean-state and atmospheric variability in FTAC, which may further perturb the ENSO onset. In other words, the El-Niño like changes of the PO mean state in FTAC-obs provide more favorable conditions for El Niño to develop through the Bjerknes feedback (e.g., a reduced equatorial SST gradient and a flatter thermocline across the PO) and reduced atmospheric noise over the AO during boreal spring. This finally leads to a much better seasonal phase-locking of the simulated ENSO and an improved ENSO amplitude during its peak phase in FTAC-obs in comparison of CTRL and FTAC (Fig. 8).

Finally, the AO decoupled experiments demonstrate that the AO SST variability significantly modulates ENSO during its decaying phase. This is illustrated by the regression analysis of the ONDJ Nino34 index with quarterly SST time series during the following year (e.g., year +1) in FTAC-obs (Fig. 12). FTAC displays a very similar evolution (not shown). The corresponding regression analyses for observations and CTRL are shown in Fig. S3. The warm SST PO pattern lasts longer in FTAC-obs (and FTAC) than in CTRL and the ENSO signal is still robust at the end of year +1 in this run (Fig. 12c). Overall, the results highlight that the ENSO-induced AO SST anomalies in CTRL (Fig. S3b), which are on the other hand very small in the FTAC-obs by design (Fig. 12), accelerate the transition from El Niño to La Niña (in CTRL) during year +1.

4.c AO indirect effect on ISMR

The AO “indirect” effect on ISMR, mediated by the ISM-ENSO relationship, is now explored again with the help of the AO decoupled experiments.

Figure 13ab shows the ISMR seasonal cycle and monthly standard deviations from observation~~s~~, CTRL and the two AO decoupled experiments. The ISMR seasonal cycle is not altered in the nudging experiments, and they replicate the same results of CTRL (Fig. 13a). Observed ISMR variability is characterized by a double peak at the onset and withdraw of ISM (Fig. 13b). CTRL underestimates ISMR variability in the pre-monsoon season and overestimates it during June-August. The nudging experiments reduce the simulated ISMR variability during the last half of ISM, especially FTAC-obs (Fig. 13b), despite ENSO is stronger during boreal summer in FTAC and FTAC-obs (Fig. 8).

To assess the AO “indirect” effect, Figure 13c shows the observed and simulated lead-lag correlations between ISMR and Nino34 SST quarterly time series in a three-year window from the beginning of year -1 (preceding the ISMR year) to the end of year +1 (following the ISMR year). Consistent with Fig. 4a, there are significant positive correlations one year before ISM in observations. The sign of the correlation reverses during the pre-monsoon season of year 0 and the correlation gets significantly negative during boreal summer and winter of year 0. These negative correlations fade away during year +1. Thus, the most favorable conditions for a strong ISM are during the transitions from an El Niño during year -1 to a La Niña event in year 0 in agreement with our analysis in Section 3.

CTRL is able to reproduce realistically the significant negative correlation between the ISMR and ENSO during boreal summer of year 0 and the decrease of amplitude of this negative correlation during year +1. However, the model shows large discrepancies from observations with a negative correlation during several months before ISM (Fig. 13c). This bias is again consistent with the results of Section 3. However, the relative success of the model in reproducing the observed simultaneous relationships between ISMR and ENSO is important as the analysis of the nudged experiments can then provide more insights on the precise role of the AO in this system.

In this respect, the lead-lag correlations between ENSO and ISMR are significantly different between the two nudging experiments and CTRL, with a consistent weakening of the simultaneous inverse relationship between ISM and ENSO (Fig. 13c), despite Nino34 SST variability is higher during boreal summer in FTAC and FTAC-obs compared to CTRL (Fig. 8). In FTAC-obs, the simultaneous negative correlation between ISMR and Nino34 SST is not even statistically significant at the 90% confidence level, despite FTAC-obs simulates a stronger ENSO than FTAC. As the warm SST mean-state bias affecting the tropical AO in both CTRL and FTAC is removed in FTAC-obs, these results are consistent with the AGCM experiments performed in Kucharski et al. (2007, 2009) in which a weakening of the monsoon-ENSO relationship is simulated in response to a cooling trend of the tropical AO and allow us to isolate the specific role of the SST AO mean-state biases on the simulated monsoon-ENSO relationship. However, as the simultaneous correlation between ISMR and Nino34 SST is also reduced in FTAC, the reduced AO SST variability in the two runs may also play an important role in the weakening of the inverse relationship between ISM and ENSO in the nudged experiments.

Furthermore, ISMR evolution has different flavors during the ENSO decaying year in each dataset (Figure S7). First, we find more rainfall over the IO during the pre-monsoon season (not shown) and over India and the Arabian Sea during the monsoon of year +1 in observations (Fig. S7a). This is consistent with the warm local SSTs (Fig. S3a) and the fast demise of ENSO induced upper-level subsidence during year +1 in observations (Figs. S7a and 14a). During boreal summer of the ENSO decaying year, the significant 200-hPa velocity potential anomalies are restricted to a regional dipole opposing upper-level divergence over the Arabian Sea to upper-level convergence over the western PO in observations (Fig. 14a). These features are physically consistent with the positive (negative) correlation between precipitation in the Indian (northwest PO) region during ISM of year +1 and the Nino34 index in observations (Fig. S7a). This confirms that with the increase (decrease) of the SST over the Nino34 region during the preceding boreal winter, the ISM of the next year is enhanced (suppressed) or vice versa in observations (Fig 13c; Yang et al. 2007).

CTRL is not able to replicate these precipitation and 200-hPa velocity potential anomalies during year +1 (Figs. S7b and 14b). In CTRL, there is a significant negative correlation between precipitation over the Indian region during the monsoon season of year +1 and Nino34 SST (Fig. S7b). This negative ISMR anomaly is consistent with both the persistent ENSO signal (Fig. S3b) and the (significant) positive 200-hPa velocity potential anomalies over India during boreal summer of year +1 in CTRL (Figs. S7b and 14b).

The effect of removing the AO SST variability on these correlations can now be analyzed (Figs. 14c and S7c), keeping in mind that the ENSO-related SST signal persists even longer and is stronger in FTAC-obs than in CTRL (Fig. 12). Despite this enhanced ENSO forcing, the correlation of Nino34 SST with ISMR during year +1 has vanished and is not significant in FTAC-obs (Fig. S7c). This is consistent with the weakening of the simultaneous ISMR-Nino34 correlation in FTAC-obs (Fig. 13c). The origin of this paradox can be seen from Fig. S7c, which shows that there is a stronger negative correlation between precipitations over the tropical AO during year +1 with Nino34 SST (during the preceding boreal winter) in FTAC-obs compared to CTRL. Moreover, these negative correlations are also shifted westward in FTAC-obs consistent with the corrected AO mean state in this simulation. This stronger relationship between ENSO and the AO in FTAC-obs during year +1 is further confirmed by the associated 200-hPa velocity potential signal (Fig. 14c). In the 200-hPa velocity potential anomalous pattern during boreal summer of year +1 in FTAC-obs, there is a significant positive correlation over the AO, while the correlation over the Indian region is near zero. This implies that the upper-level divergent flow is mainly from the central PO to the TNA instead toward the Indian region, which results in suppression of rainfall in the AO and a near normal ISM in FTAC-obs. FTAC shows a similar evolution (not shown), but the ENSO-induced subsidence over the AO during boreal summer of the ENSO decaying year is weaker, presumably due to the biased AO SST mean-state in FTAC.

In a nutshell, these last results illustrate that, by artificially removing the SST variability over the tropical AO in the nudged experiments, the ENSO signal is stronger and persists longer during the ENSO decaying year, but the associated upper-level divergent winds will flow mainly from the central PO to the tropical AO, resulting in rainfall suppression in the AO, but only in a weak ENSO forcing on ISM during the ENSO decaying year.

5. Conclusions and discussion

In this study, we use dedicated coupled experiments to isolate both the “direct” and “indirect” effects of AO SSTs on ISMR. The “direct” effect refers to the AO forcing on ISMR in the absence of others dominant forcings like ENSO (Kucharski et al. 2009). The “indirect” effect refers to the AO forcing on ENSO (Rodriguez-Fonseca et al. 2009; Ding et al. 2012; Ham et al. 2013ab; Jiang and Li 2021), which may subsequently affect ISMR through ENSO teleconnections. Furthermore, with the help of these experiments, we also identify the role of AO SST mean-state biases on the simulated ISMR-ENSO relationship.

First, we found that the "direct" effect of AO SST variability on ISMR is insignificant. Overall, the results highlight that ISMR is a major player in the tropical atmospheric circulation in the absence of ENSO, even forcing an AMM SST pattern during boreal fall after ISM, rather than the reverse. Several studies have suggested that the AZM may provide a direct remote forcing on ISMR through a Gill-Matsuno mechanism with a Kelvin wave transporting the signal to the IO (Kucharski et al. 2009; Pottapinjara et al. 2014), but we were not able to isolate this "direct" effect on ISMR in our simulations or observations during recent decades, even when ENSO is removed (Figs. S2 and 7), which is consistent with the modeling results of Ding et al. (2012). However, it is known that current CGCMs struggle to represent this relationship, partly due to their common strong AO SST mean-state biases (Barimalala et al. 2012; Voldoire et al. 2019). Taking into account the warm SST mean-state bias in the southeastern AO found in SINTEX-F2 (see Fig. 1a), the realism and amplitude of the AZM simulated by this CGCM are~~is~~ severely biased (Fig. 3b) and this may also deteriorate the simulated ISMR-AZM relationship in our model.

The global-scale effects of the corrections of tropical AO SST biases are readily apparent when comparing our two AO decoupled experiments with each other and with a long free simulation performed with the same model. When the AO SST mean-state bias (present in CTRL and FTAC) is corrected in FTAC-obs, the rainfall pattern in the AO is shifted northwestward (see Fig. 1f). The associated changes in diabatic heating produce a Matsuno-Gill atmospheric response centered over the eastern equatorial Pacific and generate a trans-basin (e.g., Pacific/Atlantic) atmospheric see-saw with upward motion over a large region encompassing the central and eastern equatorial Pacific and the western tropical AO and descending motion elsewhere in the Tropics. The overall effect is the emergence of an El Niño-like mean-state pattern in FTAC-obs when these AO SST biases are corrected, which is mostly significant during boreal spring (see Fig. S6). This also corresponds to the onset period of El Niño events in observations and the simulations analyzed here.

The comparison of FTAC and FTAC-obs with CTRL suggests that the "indirect" influence of the tropical AO SST variability on ISMR is significant. The main effect of AO SST variability is to modulate the amplitude and length of ENSO events, especially during their onset and decaying phases. First, AO SST variability plays a key-role in ENSO developing phase in agreement with the results of Ham et al. (2013ab). Without AO SST variability, ENSO onset, while still seasonally phase-locked and linked to the SFM over the North Pacific (Vimont et al. 2003; Boschat et al. 2013; Terray et al. 2016), occurs one season before during boreal winter. This finding supports the idea that AO SST variability is also a possible source of ENSO spread, especially during its developing year. This may reduce ENSO predictability and contributes to the spring ENSO predictability barrier (Ma et al. 2017; Ogata et al. 2019). Furthermore, when AO SST mean-state biases are also corrected (e.g., in FTAC-obs), this leads to ~~an~~ increased ENSO amplitude during its peak phase (e.g. boreal winter) as well, demonstrating nonlinear interactions between the mean state during boreal spring and ENSO amplitude.

Our results also confirm that AO SST variability modulates the length of the ENSO decaying phase, as ENSO is still active up to the end of the ENSO decaying year in the FTAC and FTAC-obs experiments (Terray et al. 2016; Kajtar et al. 2017). During boreal winter, ENSO influences the subtropical and tropical AO through the atmospheric bridge (Jiang and Li 2019). These ENSO-induced SST AO anomalies may then feedback negatively on ENSO and fasten the transition from El Niño to La Niña. This discharging capacitor effect of the AO (Wang et al. 2017) serves as a phase-reversal mechanism for the ENSO cycle as for the IO (Xie et al. 2009; Terray et al. 2016, 2021).

All these findings are consistent with recent modelling studies that have identified a tight physical linkage between AO and PO variability on decadal timescales (Kucharski et al. 2011) or in a global warming context (McGregor et al 2014) and also demonstrate that the prominent AO SST biases play a significant role in modulating the simulated Pacific Walker circulation at both the seasonal and longer time scales in current CGCMs (Kajtar et al 2018; McGregor et al. 2018; Li et al. 2020).

Finally, the absence of AO SST variability weakens the simultaneous inverse relationship between ISM and ENSO despite ENSO is stronger during boreal summer and persists longer. This result is opposite to the one found in similar IO decoupling experiments in which ENSO is also stronger and more persistent (Terray et al. 2021). The origin of this paradox lies mainly in the modulation of the Walker circulation when SST variability is removed in one of the two oceanic basins, especially during boreal summer of the ENSO decaying year (see Fig. 14). The upper-level divergent wind flows mainly from the PO to the AO, resulting in rainfall suppression in the AO, but in a weaker forcing on ISMR in the AO decoupled experiments (Fig. 14c). On the other hand, both the stronger ENSO amplitude and the enhanced upper-level convergence towards the Indian domain act in concert and result in a much stronger inverse ENSO-ISMR relationship in similar IO decoupled experiments (Terray et al. 2021).

In conclusion, while the AO “direct” effect on ISMR is insignificant in our coupled model, we highlight that the AO “direct“ effect on ENSO is significant in many aspects including the

ENSO triggering mechanism and AO capacitor effect, which ~~also~~ have also a significant “indirect” impact on ISMR mediated by the ENSO teleconnections. We hope that these encouraging results will promote the interest of performing similar IO, PO and AO decoupled experiments with other coupled models in order to verify if the insignificant “direct” effect of AO SSTs on ISMR found here is model dependent or not.

Acknowledgments: Pascal Terray is funded by Institut de Recherche pour le Développement (IRD, France). The Centre for Climate Change Research (CCCR) at the Indian Institute of Tropical Meteorology (IITM) is fully funded by the Ministry of Earth Sciences, Government of India. The SINTEX-F2 simulations are performed using HPC resources in France from GENCI-IDRIS (Grant 0106895 over the last 5 years). Analysis was done with the STATPACK and NCSTAT softwares available at https://terray.locean-ipsl.upmc.fr/software.html. Simulation data will be made available on reasonable request.

References

Barimalala R, Bracco A, Kucharski F (2012) The representation of the South Tropical Atlantic teleconnection to the Indian Ocean in the AR4 coupled models. Clim Dyn 38:1147-1166 doi:10.1007/s00382-011-1082-5

Bi D, Wang G, Cai W, Santoso A, Sullivan A, Ng B, Jia F (2022). Improved simulation of ENSO variability through feedback from the equatorial Atlantic in a pacemaker experiment. Geophys Res Lett, *49*, e2021GL096887. https://doi. org/10.1029/2021GL096887

Boschat G, Terray P, Masson S (2012) Robustness of SST teleconnections and precursory patterns associated with the Indian summer monsoon. Clim Dyn 38:2143-2165 doi: 10.1007/s00382-011-1100-7

Boschat G, Terray P, Masson S (2013) Extratropical forcing of ENSO. Geophys Res Lett 40:1-7 doi:10.1002/grl.50229

Cabos W, de la Vara A, Koseki S (2019) Tropical Atlantic variability: observations and modeling. Atmosphere 10:502 https://doi.org/ 10.3390/atmos10090502

Cai W, Wu L, Lengaigne M, Li T, McGregor S, Kug J-S, Yu J-Y, Stuecker MF, Santoso A, Li X, Ham Y-G, Chikamoto Y, Ng B, McPhaden MJ, Du Y, Dommenget D, Jia F, Kajtar JB, Keenlyside N, Lin X, Luo JJ, Martin-Rey M, Ruprich-Robert Y, Wang G, Xie SP, Yang Y, Kang SM, Choi J-Y, Gan B, Kim G-I, Kim C-E, Kim S, Kim J-H, Chang P (2019) Pantropical climate interactions. Science 363:6430 https://doi.org/10.1126/science.aav42

Carton JL, Giese BS (2008) A Reanalysis of Ocean Climate Using Simple Ocean Data Assimilation (SODA). Mon Weather Rev 136:2999-3017

Chakraborty A (2018) Preceding winter La Niña reduces Indian summer monsoon rainfall. Environmental Research Letters, 13(5):p.054030

Chakraborty A, Singhai P (2021) Asymmetric response of the Indian summer monsoon to positive and negative phases of major tropical climate patterns. Sci Rep 11:22561

Chang P, Fang Y, Saravanan R et al (2006) The cause of the fragile relationship between the Pacific El Niño and the Atlantic Niño. Nature 443:324-328 doi: https://doi.org/10.1038/nature05053

Cherchi A, Terray P, Ratna SB, Sankar S, Sooraj KP, Behera T (2021) Indian Ocean Dipole influence on Indian summer monsoon and ENSO: a review. Chapter 8 in *Indian summer monsoon variability: El Nino teleconnections and beyond*, Chowdary JS, Parekh, A, Gnanaseelan C (eds). Elsevier, ISBN: 978-0-12-822402-1. Chapter 8:157-182, https://doi.org/10.1016/B978-0-12-822402-1.00011-9

Chiang JCH, Sobel AH (2002) Tropical tropospheric temperature variations caused by ENSO and their influence on the remote tropical climate. J Clim 15:2616-2631 https://doi.org/10.1175/1520- 0442(2002)015%3c2616:TTTVCB%3e2.0.CO;2

Chiang JCH, Vimont DJ (2004) Analogous meridional modes of atmosphere-ocean variability in the tropical Pacifc and tropical Atlantic. J Clim 17(21):4143-4158

Chowdary JS, Parekh, A, Gnanaseelan C (2021) Indian summer monsoon variability: El Nino teleconnections and beyond. Chowdary JS, Parekh, A, Gnanaseelan C (eds). Elsevier, ISBN: 978-0-12-822402-1, 494 pp

Cretat J, Terray P, Masson S, Sooraj KP, Roxy MK (2017) Indian Ocean and Indian Summer Monsoon: relationships without ENSO in ocean-atmosphere coupled simulations. Clim Dyn 49:1429-1448 doi:10.1007/s00382-016-3387-x

Cretat J, Terray P, Masson S, Sooraj KP (2018) Intrinsic precursors and timescale of the tropical Indian Ocean Dipole: insights from partially decoupled experiment. Clim Dyn 51:1311-1352 https://doi.org/10.1007/s00382-017-3956-7

Dee DP et al (2011) The ERA-Interim reanalysis: Configuration and performance of the data assimilation system. Q J Roy Meteorol Soc 137:553-597

Ding H, Keenlyside NS, Latif M (2012) Impact of the equatorial Atlantic on the El Niño Southern Oscillation. Clim Dyn 38:1965-1972 https://doi.org/10.1007/s00382- 011-1097-y.

Ebisuzaki W (1997) A method to estimate the statistical significance of a correlation when the data are serially correlated. J Clim 10:2147-2153

Enfield D, Mayer D (1997) Tropical Atlantic sea surface temperature variability and its relation to El Nino-Southern Oscillation. J Geophys Res 102(C1):929-945 doi:10.1029/96JC03296

Fischer AS, Terray P, Guilyardi E, Gualdi S, Delecluse P (2005) Two independent triggers for the Indian Ocean dipole/ zonal mode in a coupled GCM. J Clim 18:3428-3449 https://doi.org/10.1175/JCLI3478.1

Frauen C, Dommenget D (2012) Influences of the tropical Indian and Atlantic Oceans on the predictability of ENSO. Geophys Res Lett 39:L02706

Gadgil S, Gadgil S (2006) The Indian monsoon, GDP and agriculture. Econ Political Wkly 41:4887-4895

Garcia-Serrano J, Cassou C, Douville H et al (2017) Revisiting the ENSO teleconnection to the Tropical North Atlantic. J Clim 30:6945-6957 https://doi.org/10.1175/JCLI-D-16-0641.1

Gill AE (1980) Some simple solutions for heat-induced tropical circulation. Q J R Meteorol Soc 106:447-462

Ham YG, Kug JS, Park JY, Jin FF (2013a) Sea surface temperature in the north tropical Atlantic as a trigger for El Niño/Southern Oscillation events. Nature Geoscience *6*(2):112

Ham YG, Kug JS, Park JY (2013b) Two distinct roles of Atlantic SSTs in ENSO variability: North Tropical Atlantic SST and Atlantic Niño. Geophys Res Lett 40(15):4012-4017

Huffman GJ, Adler RF, Morrissey MM, Bolvin DT, Curtis S, Joyce R, McGavock B, Susskind J (2001) Global precipitation at one-degree daily resolution from multisatellite observations. J Hydrometeor 2:36-50

Izumo T, Vialard J, Lengaigne M et al (2010) Influence of the state of the Indian Ocean dipole on the following years El Niño. Nat Geosci 3:168-172

Jiang L, Li T (2019) Relative roles of El Niño-induced extratropical and tropical forcing in generating tropical North Atlantic (TNA) SST anomaly. Clim Dyn 53:3791-3804 https://doi.org/10.1007/s00382-019-04748-7

Jiang L, Li T (2021) Impacts of Tropical North Atlantic and Equatorial Atlantic SST Anomalies on ENSO. J Clim 34:5635-5655 https://doi.org/10.1175/JCLI-D-20-0835.1

Kajtar JB, Santoso A, England MH, Cai W (2017) Tropical climate variability: interactions across the Pacific, Indian, and Atlantic Oceans. Clim Dyn 48:2173-2190 https://doi.org/10.1007/ s00382-016-3199-z

Kajtar JB, Santoso A, McGregor S et al (2018) Model under-representation of decadal Pacific trade wind trends and its link to tropical Atlantic bias. Clim Dyn 50:1471-1484 https://doi.org/10.1007/s00382-017-3699-5

Kumar KK, Rajagopalan B, Cane MA (1999) On the weakening relationship between the Indian monsoon and ENSO. Science 284:2156-2159

Kucharski F, Bracco A, Yoo J, Molteni F (2007) Low- frequency variability of the Indian monsoon-ENSO relationship and the tropical Atlantic: The weakening of the 1980s and 1990s. J Clim 20:4255-4266

Kucharski F, Bracco A, Yoo J, Tompkins A, Feudale L, Ruti P, Dell'Aquila A (2009) A Gill-Matsuno-type mechanism explains the tropical Atlantic influence on African and Indian monsoon rainfall. Q J R Meteorol Soc 135(640):569-579 https://doi.org/10.1002/qj.406

Kucharski F, Kang I-S, Farneti R, Feudale L (2011) Tropical Pacific response to 20th century Atlantic warming. Geophys Res Lett 38:L03702

Li X, Xie, S-P, Gille ST and Yoo C (2016) Atlantic-induced pan-tropical climate change over the past three decades. Nat. Clim. Change 6:275-280

Li C, Dommenget D, McGregor S (2020) Trans-basin Atlantic-Pacific connections further weakened by common model Pacific mean SST biases. Nat Comm 11:5677 https://doi.org/10.1038/s41467-020-19338-z

Lübbecke JF, Rodríguez-Fonseca B, Richter I, Martín-Rey M, Losada T, Polo I, Keenlyside NS (2018) Equatorial Atlantic variability: Modes, mechanisms, and global teleconnections. Wiley Interdiscip Rev Clim Change 9(4):e527 https://doi.org/10.1002/wcc.527

Ma J, Xie SP, Xu H (2017) Contributions of the North Pacific Meridional Mode to Ensemble Spread of ENSO prediction. J Clim 30:9167-9181 https://doi.org/10.1175/JCLI-D-17-0182.1

Madec G (2008) NEMO ocean engine. Note du Pole de modelisation, Institut Pierre-Simon Laplace (IPSL) No 27. ISSN No 1288-1619

Masson S, Terray P, Madec G, Luo JJ, Yamagata T, Takahashi K (2012) Impact of intra-daily SST variability on ENSO characteristics in a coupled model. Clim Dyn 39:681-707

McGregor S et al (2014) Recent Walker circulation strengthening and Pacific cooling amplified by Atlantic warming. Nature Clim Change 4:888-892

McGregor S et al (2018) Model tropical Atlantic biases underpin diminished Pacific decadal variability. Nat Clim Change 8:493-498

Meehl GA, Arblaster JM, Loschnigg J (2003) Coupled ocean-atmosphere dynamical processes in the tropical Indian and Pacific oceans and the TBO. J Clim 16:2138-2158 doi: 10.1175/2767.1

Ohba M, Ueda H (2007) An impact of SST anomalies in the Indian Ocean in acceleration of the El Nino to La Nina transition. J Meteor Soc Jpn 85:335-348

Ogata T, Doi T, Morioka Y et al (2019) Mid-latitude source of the ENSO-spread in SINTEX-F ensemble predictions. Clim Dyn 52:2613-2630 https://doi.org/10.1007/s00382-018-4280-6

Pai DS, Sridhar L, Badwaik MR, Rajeevan M (2015) Analysis of the daily rainfall events over India using a new long period (1901-2010) high resolution (0.25 × 0.25) gridded rainfall data set. Clim Dyn 45:755-776

Pottapinjara V, Girishkumar MS, Ravichandran M, Murtugudde R (2014) Influence of the Atlantic zonal mode on monsoon depressions in the Bay of Bengal during boreal summer. J Geophys Res Atmos 119(11):6456-6469 https://doi.org/10.1002/ 2014JD021494

Pottapinjara V, Girishkumar MS, Sivareddy S, Ravichandran M, Murtugudde R (2016) Relation between the upper ocean heat content in the equatorial Atlantic during boreal spring and the Indian monsoon rainfall during June-Spetember. Int J Climatol 36:2469-2480 https://doi.org/10.1002/joc.4506

Rao SA et al (2019) Monsoon mission: a targeted activity to improve monsoon prediction across scales. Bull Am Meteorol Soc 100(12):2509-2532 https://doi.org/10.1175/ BAMS-D-17-0330.1

Rayner NA, Parker DE, Horton EB, Folland CK, Alexander LV, Rowell DP, Kent EC, Kaplan A (2003) Global analyses of sea surface temperature, sea ice, and night marine air temperature since the late nineteenth century. J Geophys Res 108(D14):4407 https:// doi.org/10.1029/2002JD002670

Reynolds RW, Smith TM, Liu C, Chelton DB, Casey KS, Schlax MG (2007) Daily high-resolution-blended analyses for sea surface temperature. J Clim 20:5473-5496 https://doi. org/10.1175/2007JCLI1824.1

Richter I, Xie S-P, Behera S, Doi T, Masumoto, Y (2014) Equatorial Atlantic variability and its relation to mean state biases in CMIP5. Clim Dyn 42:171 https://doi.org/doi.10.1007/s00382-012-1624-5

Richter I, Tokinaga H, Kosaka Y, Doi T, Kataoka T (2021) Revisiting the Tropical Atlantic Influence on El Niño-Southern Oscillation. J clim 34:8533-8548 doi:10.1175/JCLI-D-21-0088.1

Richter I, Tokinaga H (2021) The Atlantic zonal mode: Dynamics, thermodynamics, and teleconnections. In: Behera SK (eds) Tropical and extra-tropical air-sea interactions. Elsevier. ISBN: 9780128181560

Rodriguez-Fonseca B, Polo I, Garcia-Serrano J, Losada T, Mohino E, Mechoso CR, Kucharski F (2009) Are Atlantic Ninos enhancing Pacific ENSO events in recent decades? Geophys Res Lett 36:L20705

Roeckner E, Baüml G, Bonaventura L, Brokopf R, Esch M, Girogetta M, Hagemann S, Kirchner I, Kornblueh L, Manzini E, Rhodin A, Schlese U, Schulzweida U, Tompkins A (2003) The atmospheric general circulation model ECHAM 5. Part I, MPI Report, vol 349. Hamburg, Max-Planck-Institut für Meteorologie

Sabeerali C, Ajayamohan R, Bangalath HK, Chen N (2019) Atlantic zonal mode: an emerging source of indian summer monsoon variability in a warming world. Geophys Res Lett 46(8):4460-4467 https://doi.org/10.1029/2019GL082379

Santoso A, England MH, Cai W (2012) Impact of Indo-Pacic feedback interactions on ENSO dynamics diagnosed using ensemble climate simulations. J Clim 25:7743-7763

Srivastava G, Chakraborty A, Nanjundiah RS (2019) Multidecadal see-saw of the impact of ENSO on Indian and West African summer monsoon rainfall. Clim Dyn 52**:**6633-6649

Stuecker MF, Timmermann A, Jin FF, Chikamoto Y, Zhang W, Wittenberg AT, Widiasih E, Zhao S (2017) Revisiting ENSO/Indian Ocean Dipole phase relationships. Geophys Res Lett 44:2481-2492 doi:10.1002/2016GL072308

Terray P, Delecluse P, Labattu S, Terray L (2003) Sea Surface Temperature Associations with the Late Indian Summer Monsoon. Clim Dyn 21:593-618 doi:10.1007/s00382-003-0354-0

Terray P, Dominiak S, Delecluse P (2005) Role of the southern Indian Ocean in the transitions of the monsoon-ENSO system during recent decades. Clim Dyn 24:169-195 doi:10.1007/s00382- 0040480-3

Terray P, Masson S, Prodhomme C, Roxy MK, Sooraj KP (2016) Impacts of Indian and Atlantic oceans on ENSO in a comprehensive modeling framework. Clim Dyn 46:2507-2533 https:// doi.org/10.1007/s00382-015-2715-x

Terray P, Sooraj KP, Masson S et al (2021) Anatomy of the Indian Summer Monsoon and ENSO relationships in state-of-the-art CGCMs: role of the tropical Indian Ocean. Clim Dyn 56**:**329-356 https://doi.org/10.1007/s00382-020-05484-z

Timmermann R, Goosse H, Madec G, Fichefet T, Ethe C, Duliere V (2005) On the representation of high latitude processes in the ORCA-LIM global coupled sea ice-ocean model. Ocean Model 8:175-201

Tokinaga H, Richter I, Kosaka Y (2019) ENSO influence on the Atlantic Niño, revisited: Multi-year versus single-year ENSO events. J Clim 32:4585-4600 doi: https://doi.org/10.1175/ JCLI-D-18-0683.1.

Valcke S (2006) OASIS3 user guide (prism_2-5). CERFACS technical report TR/CMGC/06/73, PRISM report no. 3, Toulouse, pp 64

Vimont DJ, Wallace JM, Battisti DS (2003) The seasonal footprinting mechanism in the Pacific: Implications for ENSO. J Clim 16(16):2668-2675

Vittal H, Villarini G, Zhang W (2020) Early prediction of the Indian summer monsoon rainfall by the Atlantic Meridional Mode. Clim Dyn 54:2337-2346 https://doi.org/10.1007/s00382-019-05117-0

Voldoire A, Exarchou E, Sanchez-Gomez E, Demissie T, Deppenmeier AL, Frauen C, Goubanova K, Hazeleger W, Keenlyside N, Koseki S et al (2019) Role of wind stress in driving SST biases in the tropical Atlantic. Clim Dyn 53(5–6):3481–3504

Wang L, Yu J-Y, Paek H (2017) Enhanced biennial variability in the Pacific due to Atlantic capacitor effect . Nat Comm 8:14887 doi:10.1038/ncomms14887

Webster PJ, Magana V, Palmer TN, Shukla J, Tomas RA, Yanai M, Yasunari T (1998) Monsoons: processes, predictability and the prospects for prediction. J Geophys Res 103:14451-14510 doi:10.1029/97JC02719

Xie SP, Hu K, Hafner J et al (2009) Indian Ocean capacitor effect on Indo-Western pacific climate during the summer following El Niño. J Clim 22:730-747 https://doi.org/10.1175/2008JCLI2544.1

Xie SP, Kosaka Y, Du Y et al (2016) Indo-western Pacific Ocean capacitor and coherent climate anomalies in post-ENSO summer: a review. Adv Atmos Sci 33:411-432 https://doi.org/10.1007/ s00376-015-5192-6

Yang JL, Liu QY, Xie S-P, et al (2007) Impact of the Indian Ocean SST basin mode on the Asian summer monsoon. Geophys Res Lett 34:L02708 doi:10.1029/2006GL028571

Yang X, Huang P (2021) Restored relationship between ENSO and Indian summer monsoon rainfall around 1999/2000. The Innovation 2(2):100102

Zhang L, Han W (2021) Indian Ocean Dipole leads to Atlantic Niño. Nat Comm 12:5952 https://doi.org/10.1038/s41467-021-26223-w

Zhang Y, Zhou W, Li T (2021a) Impact of the Indian Ocean Dipole on Evolution of the Subsequent ENSO: Relative Roles of Dynamic and Thermodynamic Processes. J Clim 34: 3591-3607

Zhang W, Jiang F, Stuecker MF, Jin F-F, Timermann A (2021b) Spurious North Tropical Atlantic precursors to El Niño. Nat Comm 12:3096 https://doi.org/10.1038/s41467-021-23411-6

Figure captions

Figure 1: **a)** SST annual means difference (unit: °C) between CTRL and ERAi; **b)** Z20 annual means difference (unit: m) between CTRL and SODA; **c)** Rainfall annual means difference (unit: mm/day) between CTRL and GPCP; **d)** SST annual means difference (unit: °C) between FTAC-obs and CTRL; **e)** Z20 annual means difference (unit: m) between FTAC-obs and CTRL; **f)** Rainfall annual means difference (unit: mm/day) FTAC-obs and CTRL. The nudging domain for FTPC and FTPC-obs (FTAC and FTAC-obs) is shown in blue (purple) in panel a. See Section 2 and Table 1 for more details.

Figure 2: Empirical Orthogonal Function (EOF) 1st and 2nd modes for detrended SST anomalies with monthly means removed ~~12-monthly anomaly of detrended SST~~ obtained from ERAi and CTRL. **a)** and **b)** EOF1 and EOF2 from ERAi SST detrended anomalies (1979-2015 period), respectively. **c)** and **d)** EOF1 and EOF2 from CTRL SST detrended anomalies (11-210 period), respectively. The number in parentheses for each panel gives the % of SST variance described by the EOF mode.

Figure 3: **a)** Monthly means of ATL3 SST (unit: °C) index from ERAi (blue) and CTRL (orange); **b)** Monthly standard deviations of ATL3 SST (unit: °C) from ERAi (blue) and CTRL (orange).

Figure 4: **a)** Quarterly SST time series (from ERAi) during the preceding (e.g. year -1) and simultaneous (e.g. year 0) ISM years, regressed against the ISMR index (e.g. JJAS ISM rainfall from GPCP). Unit for the SST regression coefficient is °C by mm/day. **b)** Same as **a)**, but for regression using quarterly rainfall and 850-hPa wind time series. Units for the rainfall and 850-hPa wind regression coefficients are mm/day by mm/day and m s^{-1} by mm/day, respectively. **c),** Same as **a)**, but for quarterly 200-hPa velocity potential time series. Unit for the 200-hPa velocity potential regression coefficient is 10^5 m^2 s^{-1} by mm/day. Regression coefficients reaching the 90% significance level according to a phase-scrambling bootstrap test (Ebisuzaki 1997) with 999 samples are contoured (SST or 200-hPa velocity potential) or shown (rainfall and 850-hPa wind). Quarterly time series refer to to the seasons February-May, June-September, October-January and so on.

Figure 5: **a)** Quarterly SST time series during year 0 regressed against the ISMR index (e.g. JJAS ISM rainfall) in CTRL. Unit for the SST regression coefficient is °C by mm/day. **b)** Same as **a)**, but for regression using quarterly rainfall and 850-hPa wind time series in CTRL. Units for the rainfall and 850-hPa wind regression coefficients are mm/day by mm/day and m s^{-1} by mm/day, respectively. **c),** Same as **a)**, but for quarterly 200-hPa velocity potential time

series in CTRL. Unit for the 200-hPa velocity potential regression coefficient is 10^5 m^2 s^{-1} by mm/day. Regression coefficients reaching the 90% significance level according to a phase-scrambling bootstrap test (Ebisuzaki 1997) are contoured (SST or 200-hPa velocity potential) or shown (rainfall and 850-hPa wind).

Figure 6: Empirical Orthogonal Function (EOF) 1st and 2nd modes for 12-monthly anomaly of detrended SST obtained from FTPC and FTPC-obs experiments. **a)** and **b)** EOF1 and EOF2 from FTPC SST detrended anomalies (11-110 period), respectively. **c)** and **d)** EOF1 and EOF2 from FTPC-obs SST detrended anomalies (11-50 period), respectively. The number in parentheses for each panel gives the % of SST variance described by the EOF mode.

Figure 7: **a)** Quarterly SST time series during year 0 regressed against the ISMR index (e.g. JJAS ISM rainfall) in FTPC-obs. Unit for the SST regression coefficient is °C by mm/day. **b)** Same as **a)**, but for quarterly 200-hPa velocity potential time series in FTPC-obs. Unit for the 200-hPa velocity potential regression coefficient is 10^5 m^2 s^{-1} by mm/day. Regression coefficients reaching the 90% significance level according to a phase-scrambling bootstrap test (Ebisuzaki 1997) are contoured.

Figure 8: Monthly standard deviations of Nino34 SST (unit:°C) from ERAi (blue), CTRL (orange), FTAC (green) and FTAC-obs (red).

Figure 9: **a)** Quarterly rainfall and 850-hPa wind time series during boreal winter and spring regressed against the Nino34 index during the following boreal winter (e.g. ONDJ Nino34 SST) in FTAC-obs. **b)** Same as **a)**, but in FTAC. **c)** Quarterly SST time series during boreal winter and spring regressed against the Nino34 index during the following boreal winter in FTAC-obs. **d)** Same as **c)**, but in FTAC. Unit for the SST regression coefficient is °C by °C. Units for the rainfall and 850-hPa wind regression coefficients are mm/day by °C and m s^{-1} by °C, respectively. Regression coefficients reaching the 90% significance level according to a phase-scrambling bootstrap test (Ebisuzaki 1997) are contoured (SST or 200-hPa velocity potential) or shown (rainfall and 850-hPa wind).

Figure 10: **a)** 850-hPa zonal wind boreal spring means differences (unit: m s^{-1}) between FTAC-obs and CTRL; **b)** 200-hPa zonal wind boreal spring means differences (unit: m s^{-1}) between FTAC-obs and CTRL; **c)** 850-hPa velocity potential boreal spring means differences (unit: 10^6 m^2 s^{-1}) between FTAC-obs and CTRL; **d)** 200-hPa velocity potential boreal spring means differences (unit: 10^6 m^2 s^{-1}) between FTAC-obs and CTRL; **e)** 850-hPa stream function boreal spring means differences (unit: 10^6 m^2 s^{-1}) between FTAC-obs and CTRL; **f)**

200-hPa stream function boreal spring means differences (unit: 10^6 m^2 s^{-1}) between FTAC-obs and CTRL.

Figure 11: **a)** Rainfall boreal spring standard deviation differences (unit: mm/day) between FTAC-obs and CTRL. **b)** Same as **a)**, but for FTAC and CTRL. **c)** 850-hPa zonal wind boreal spring standard deviation differences (unit: m s^{-1}) between FTAC-obs and CTRL. **d)** Same as **c)**, but for FTAC and CTRL.

Figure 12: **a)** Boreal spring SST time series regressed against the Nino34 index during the preceding boreal winter (e.g. ONDJ Nino34 SST) in FTAC-obs; **b)** Boreal summer SST time series regressed against the Nino34 index during the preceding boreal winter in FTAC-obs; **c)** Boreal winter SST time series regressed against the Nino34 index during the preceding boreal winter in FTAC-obs. Unit for the SST regression coefficient is °C by °C. Regression coefficients reaching the 90% significance level according to a phase-scrambling bootstrap test (Ebisuzaki 1997) are contoured.

Figure 13: **a)** Monthly means of ISMR (unit: mm/day) from GPCP (blue), CTRL (orange), FTAC (green) and FTAC-obs (red); **b)** Monthly standard deviations of ISMR (unit: mm/day) from GPCP (blue), CTRL (orange), FTAC (green) and FTAC-obs (red); **c)** Lead-lag correlations between ISMR and quarterly Nino3.4 SSTs starting from the beginning of the previous year (e.g. year - 1) to the end of the following year of the monsoon (e.g. year +1) in observations (blue), CTRL (orange), FTAC (green) and FTAC-obs (red). X-axis indicates the lag (in 4 months interval) for a 36 months period starting one year before the developing year of ISMR (e.g. year 0) and Y-axis is the amplitude of the correlation. Thus, the coefficients corresponding to -1, 0, +1 lags refer, respectively, to the correlations between ISMR in year 0 (e.g. JJAS ISM rainfall) and February-May, June-September and October-January Niño-3.4 SSTs, also during year 0, and so on. Circles indicate correlations that are above the 90% significance confidence level according to a phase-scrambling bootstrap test (Ebisuzaki 1997).

Figure 14: **a)** Boreal spring and summer 200-hPa velocity potential time series regressed against the preceding boreal winter Nino34 SST in ERAi. **b)** Same as **a)**, but for CTRL. **c)** Same as **a)**, but for FTAC-obs. Unit for the 200-hPa velocity potential regression coefficient is 10^5 m^2 s^{-1} by mm/day. Regression coefficients reaching the 90% significance level according to a phase-scrambling bootstrap test (Ebisuzaki 1997) are contoured.

Figure S1: **a)** SST seasonal standard deviations (unit: °C) computed from ERAi. **b)** SST seasonal standard deviation differences (unit: °C) computed between CTRL and ERAi.

Figure S2: **a)** Quarterly (residual) SST time series during the preceding (e.g. year -1) and simultaneous (e.g. year 0) ISM years regressed against the ISMR index (e.g. JJAS ISM rainfall) in ERAi and GPCP after the simultaneous linear effect of the Nino34 index has been removed from the SST time series by a linear regression method. Unit for the SST regression coefficient is °C by mm/day. **b)** Same as **a),** but for CTRL**.**

Figure S3: **a)** Quarterly SST time series during years 0 and +1 regressed against the Nino34 index during boreal winter (e.g. ONDJ Nino34 SST) in ERAi. **b)** Same as **a)**, but in CTRL. Unit for the SST regression coefficient is °C by °C. Regression coefficients reaching the 90% significance level according to a phase-scrambling bootstrap test (Ebisuzaki 1997) are contoured.

Figure S4: **a)** Quarterly rainfall and 850-hPa wind time series during years 0 and +1 regressed against the Nino34 index during boreal winter (e.g. ONDJ Nino34 SST) in GPCP and ERAi. **b)** Same as **a)**, but in CTRL. Units for the rainfall and 850-hPa wind regression coefficients are mm/day by °C and m s^{-1} by °C, respectively. Regression coefficients reaching the 90% significance level according to a phase-scrambling bootstrap test (Ebisuzaki 1997) are shown.

Figure S5: **a)** SST standard-deviation differences (unit: °C) between FTAC-obs and CTRL during boreal spring (e.g. FMAM); **b)** SST standard-deviation differences (unit: °C) between FTAC-obs and CTRL during boreal summer (e.g. JJAS); **c)** SST standard-deviation differences (unit: °C) between FTAC-obs and CTRL during boreal winter (e.g. ONDJ). **d)**, **e)** and **f)** Same as **a)**, **b)** and **c),** but for SST standard-deviation differences between FTAC-obs and FTAC.

Figure S6: **a)** SST seasonal mean climatological differences (unit: °C) between FTAC-obs and CTRL; **b)** Rainfall seasonal means differences (unit: mm/day) between FTAC-obs and CTRL; **c)** Z20 seasonal means differences (unit: m) between FTAC-obs and CTRL.

Figure S7: **a)** Correlation coefficients between the Nino34 index during boreal winter (e.g. ONDJ) and boreal summer (e.g. JJAS) rainfall during the following year in ERAi and GPCP. **b)** Same as **a)**, but in CTRL. **c)** Same as **a)**, but in FTAC-obs. Correlation coefficients above the 90% significance confidence level according to a phase-scrambling bootstrap test (Ebisuzaki 1997) are contoured.

Table captions

Table 1: Summary of the numerical experiments with their main characteristics, including length, nudging domain and SST climatology used for the nudging in the AO or PO decoupled experiments. The nudged experiments are the Forced Tropical Pacific Climatology (FTPC), the Forced Tropical Pacific observed Climatology (FTPC-obs), the Forced Tropical Atlantic Climatology (FTAC) and, finally, the Forced Tropical Atlantic observed Climatology (FTAC-obs) runs. See text for more details. For the FTPC and FTPC-obs experiments only ocean grid-points in the PO are included in the correction or smoothing areas and, similarly, for the FTAC and FTAC-obs experiments. The different correction domains are also displayed in Figure 1a. The observed daily SST climatology used in the FTPC-obs and FTAC-obs experiments is derived from the AVHRR only daily Optimum Interpolation SST version 2 (OISSTv2) dataset for the 1982-2010 period (Reynolds et al. 2007).